Astronomy Reports, Vol. 46, No. 6, 2002, pp. 435–442. Translated from Astronomicheskiĭ Zhurnal, Vol. 79, No. 6, 2002, pp. 483–491.

Color Variations in the Gravitational Lens Q2237+0305

V. N. Shalyapin

Institute of Radio Astronomy, National Academy of Sciences of Ukraine, ul. Krasnoznamennaya 4, Kharkov, 310002 Ukraine

Received June 10, 2001; in final form, November 23, 2001

Abstract—We show that the color index of a quasar image and the second time derivative of the intensity should be correlated if variations of the amplification coefficient for gravitational microlensing are smooth. We estimate an upper limit for the size of the emitting region of the quasar associated with the gravitational lens Q2237+0305 based on simultaneous observations made in 1997 by the OGLE group in the V band and at the Maĭdanak Observatory in the R band. © *2002 MAIK "Nauka/Interperiodica".*

1. INTRODUCTION

In the context of geometrical optics, the angle of gravitational deviation of light is essentially independent of the wavelength. Therefore, when a gravitational lens splits an image of a quasar, all components of the image are expected to have the same colors. However, two factors can give rise to differences in the colors of the images [1]. The first is related to the fact that the light from each image passes through different regions in the lensing galaxy, with different extinctions. The higher the extinction, the redder the image. The other possible factor is the finite size of the quasar. If the brightness distribution across the quasar image depends on the wavelength, and if the amplification coefficient of the gravitational lens varies appreciably across the source disk, regions with different colors are amplified differently, resulting in different colors for the different images. If the extinction in the lensing galaxy is variable (e.g. due to moving dust clouds) or the gravitational amplification varies with time (e.g. due to moving microlenses), the color of the images should be time-dependent.

Differences in the colors of images were detected in the very first observations of the quadruple lens Q2237+0305 [2]. When intensity variability was discovered [3], attempts were also made to detect color variations. Substantial variations of the intensities of images B and C were seen [4], but the colors of all the components remained constant. The expected color variations were calculated in [5], and the correlation between the intensity and color was studied. Observations with the Hubble Space Telescope [6] demonstrated that the colors observed in 1991 do not fit the same linear relation as those observed in 1988 [2]. Finally, using our observations obtained at the Maĭdanak Observatory in 1995 [7], we concluded that component B had become bluer than A, whereas in 1987 [2] it was redder. We were not able to choose between two possible origins for the color variations: extinction and microlensing. Our data were confirmed by observations with the Nordic Optical Telescope [8] carried out a month later. The relation $\Delta m(A-B) \sim \lambda^{-1}$ was found in the recent study of Nadeau *et al.* [9].

Color variations in Q2237+0305 can be seen more clearly if we collect data obtained in different filters by several observers at roughly the same time. Figures 1a–1d present the intensities of components B, C, and D relative to image A. Observations in September 1987 [2] indicate (Fig. 1a) that the difference in the intensities of the components decreases with increasing wavelength. This means that all the images are *redder* than A. The same was true in 1997 (Fig. 1b). However, the behavior of image B in the other two panels stands out. Figure 1c, taken from [9], presents the dependence of the relative intensity on the wavelength observed in the fall of 1991. The difference between the images increases with the wavelength; i.e., image B is *bluer* than A. Figure 1d, which corresponds to the second half of 1995, presents four different sets of observations, made by Westphal in July [10], Vakulik in September [7], Burud in October [8], and Blanton in November [11]. This figure displays the intensity and color variations as a function of time; however, image B always remains bluer.

Note that, in studies of the microlensing of quasars, the techniques used to analyze the chromaticity of the source are substantially different from those used in studies of microlensing of stars in the Galaxy and nearby galaxies. In the case of microlensing in our Galaxy, as a rule, the law for the variations in the amplification of a point source is considered to be known. It is comparatively easy to calculate the impact of a nonuniform brightness distribution across the stellar disk (limb darkening) at different

1063-7729/02/4606-0435$22.00

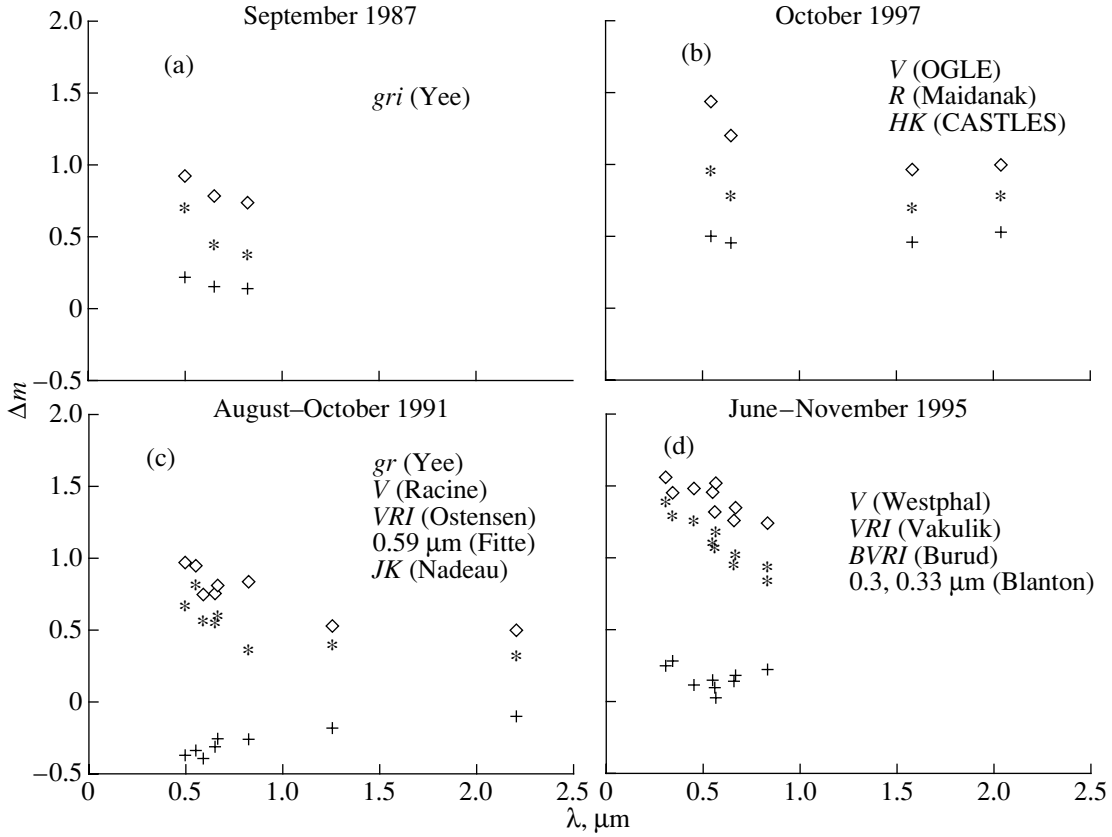

Fig. 1. Relative intensities of the components of Q2237+0305 at different times. The pluses, asterisks, and diamonds denote the differences $m_B - m_A$, $m_C - m_A$, and $m_D - m_A$, respectively.

wavelengths [12, 13], and such effects have already been observed for giants [14]. In addition, in microlensing within a galaxy, together with extinction and the finite source radii, several additional reasons for color variations can arise (see, for example, [15, 16]). In extragalactic microlensing, the distribution of the amplification coefficient remains unknown and other analysis techniques must be developed.

Here, we study certain regular behavior in color variations due to gravitational microlensing, which can be used to track their correlations with intensity variations and distinguish them from color variability due to time-variable extinction.

2. AMPLIFICATION OF AN EXTENDED SOURCE

Since the color of an image is determined by the difference of the amplifications for sources of different sizes, let us first consider the amplification of an extended source in a gravitational field.

The amplification of an extended source μ_{ext} can be represented as the product of the amplification of a point source $\mu(\mathbf{r})$ and the brightness distribution $I(\mathbf{r})$ integrated over the radiating area, normalized to the general unperturbed intensity (see, for example, [17]):

$$\mu_{ext} = \frac{\int\int I(\mathbf{r})\mu(\mathbf{r})d\mathbf{r}}{\int\int I(\mathbf{r})d\mathbf{r}}. \quad (1)$$

If the amplification coefficient does not vary dramatically over the surface of the source, it can be expanded in a series with the origin at the center of the radiating region:

$$\mu(\mathbf{r}) = \mu(0) + x\frac{\partial\mu}{\partial x} + y\frac{\partial\mu}{\partial y} + \frac{1}{2}\left(x^2\frac{\partial^2\mu}{\partial x^2} + 2xy\frac{\partial^2\mu}{\partial x\partial y} + y^2\frac{\partial^2\mu}{\partial y^2}\right). \quad (2)$$

Then, the intensity of the extended source can be represented by the series

$$\int\int I(\mathbf{r})\mu(\mathbf{r})d\mathbf{r} = \mu(0)\int\int I(\mathbf{r})d\mathbf{r} + \frac{\partial\mu}{\partial x}\int\int xI(\mathbf{r})d\mathbf{r} + \frac{\partial\mu}{\partial y}\int\int yI(\mathbf{r})d\mathbf{r} + \frac{1}{2}\left(\frac{\partial^2\mu}{\partial x^2}\int\int x^2I(\mathbf{r})d\mathbf{r} + 2\frac{\partial^2\mu}{\partial x\partial y}\right. \quad (3)$$

$$\times \int\int xyI(\mathbf{r})d\mathbf{r} + \frac{\partial^2\mu}{\partial y^2}\int\int y^2 I(\mathbf{r})d\mathbf{r}\Big),$$

whose first term corresponds to the amplification of the point source multiplied by the general unperturbed intensity, or the zero moment

$$M_0 = \int\int I(\mathbf{r})d\mathbf{r}. \quad (4)$$

The second and third terms are specified by the gradient of the amplification and the first moments of the intensity distribution

$$M_1 = \int\int xI(\mathbf{r})d\mathbf{r}, \qquad M_2 = \int\int yI(\mathbf{r})d\mathbf{r}, \quad (5)$$

and the subsequent terms are second derivatives of the field of the amplification coefficient multiplied by the second moments of the intensity distribution:

$$M_{11} = \int\int x^2 I(\mathbf{r})d\mathbf{r}, \quad M_{12} = \int\int xyI(\mathbf{r})d\mathbf{r}, \quad (6)$$
$$M_{22} = \int\int y^2 I(\mathbf{r})d\mathbf{r}.$$

2.1. Sources with Azimuthal Symmetry

If the source displays azimuthal symmetry $I(\mathbf{r}) = I(r)$, the first moments of the intensity distribution are zero:

$$M_1 = \int_0^{2\pi}\cos\varphi d\varphi\int_0^\infty I(r)r^2dr = 0, \quad (7)$$
$$M_2 = 0.$$

The second moments in x and y are equal to each other, and the mixed moment vanishes:

$$M_{11} = \int_0^{2\pi}\cos^2\varphi d\varphi\int_0^\infty I(r)r^3dr \quad (8)$$
$$= \pi\int_0^\infty I(r)r^3dr = M_{22}, \qquad M_{12} = 0.$$

Thus, the resulting amplification of an extended source can be written as the sum of the point source amplification μ_p and the Laplacian of the amplification field multiplied by some constant that depends on the specific form of the distribution:

$$\mu_\mathrm{ext} = \mu_\mathrm{p} + \frac{1}{4}\Delta\mu\frac{\int_0^\infty I(r)r^3dr}{\int_0^\infty I(r)rdr}. \quad (9)$$

Note that a similar formula was previously derived in [18]. We will present explicit formulas for two specific distributions.

2.1.1. A homogeneous disk. The constant intensity inside the radius R of the disk cancels out in (9), so that it can be chosen equal to an arbitrary constant value. For the sake of simplicity, we will take the intensity to be unity. Then, the total unperturbed intensity can be written

$$M_0 = 2\pi\int_0^\infty I(r)rdr = \pi R^2. \quad (10)$$

The second moments of the distribution are

$$M_{11} = M_{22} = \pi\int_0^\infty I(r)r^3dr = \pi\frac{R^4}{4}, \quad (11)$$

and the amplification coefficient is

$$\mu_\mathrm{ext} = \mu_\mathrm{p} + \Delta\mu\frac{R^2}{8}. \quad (12)$$

2.1.2. A Gaussian disk. A Gaussian distribution $I(r) = \exp(-r^2/R^2)$ also depends only on the radius R. Its total unperturbed intensity, second moments, and amplification coefficient are

$$M_0 = 2\pi\int_0^\infty I(r)rdr \quad (13)$$
$$= 2\pi\int_0^\infty e^{-r^2/R^2}rdr = \pi R^2,$$

$$M_{11} = M_{22} = \pi\int_0^\infty I(r)r^3dr = \pi\frac{R^4}{2}, \quad (14)$$

$$\mu_\mathrm{ext} = \mu_\mathrm{p} + \Delta\mu\frac{R^2}{4}. \quad (15)$$

Note that the amplifications for a homogeneous disk (12) and a Gaussian source (15) differ only in the factor in the denominator of the second term.

2.2. Sources with Elliptical Symmetry

If the source displays elliptical symmetry, $I(\mathbf{r}) = I(x/a, y/b)$ (for example, it is inclined to the line of sight at some angle i), formula (9) is slightly modified, but the dependence on the second derivatives remains. As an example, we present formulas for an elliptical Gaussian disk with unit intensity at the center:

$$I(x,y) = e^{-(x^2/a^2+y^2/b^2)}. \quad (16)$$

The moments of the distribution are

$$M_0 = \pi ab, \qquad M_1 = M_2 = 0, \quad (17)$$
$$M_{11} = \frac{\pi}{2}a^3b, \qquad M_{12} = 0, \qquad M_{22} = \frac{\pi}{2}ab^3,$$

while the amplification factor takes the form

$$\mu_\mathrm{ext} = \mu_\mathrm{p} + \frac{1}{4}\left(\frac{\partial^2\mu}{\partial x^2}a^2 + \frac{\partial^2\mu}{\partial y^2}b^2\right) \quad (18)$$
$$= \mu_\mathrm{p} + \frac{R^2}{4}\left(\frac{\partial^2\mu}{\partial x^2} + \cos^2 i\frac{\partial^2\mu}{\partial y^2}\right).$$

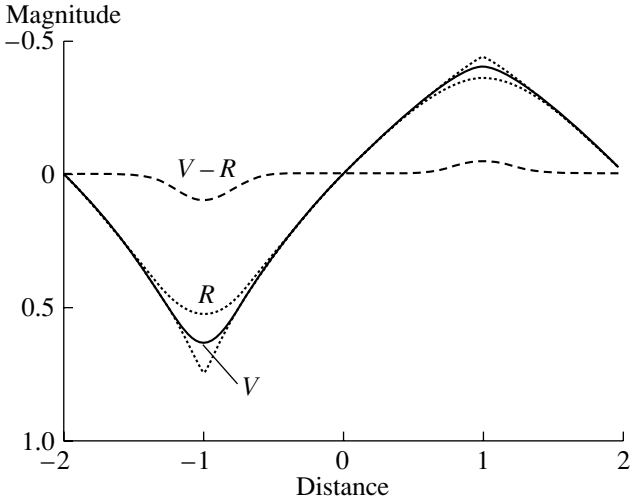

Fig. 2. Piecewise-linear model for the variability.

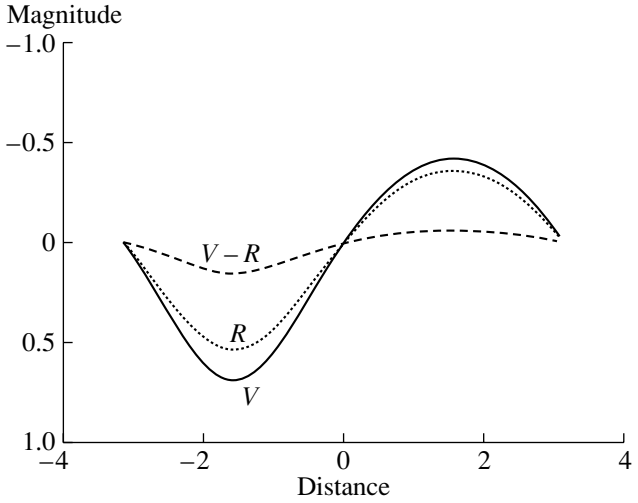

Fig. 3. Sinusoidal model for the variability.

3. RELATION BETWEEN INTENSITY AND COLOR INDEX

Formulas (9) and (18) express the amplification of an extended source in terms of its radius, the amplification at the center of the radiating region, and the second derivatives of the amplification field. If we assume that differences in the radiation of quasars at different wavelengths are due only to differences in the effective radii, we can relate color-index variations or differences in the amplifications of two sources with different sizes with the second derivatives of the amplification field in the framework of our approximation. The second partial derivative along the vector of motion of the source can be derived from the light curve. The transverse second derivative is unknown; however, its average over large time intervals should be zero. It follows that for symmetrical sources and smooth variations of the amplification coefficient, the color index and second derivative of the light curve should be correlated.

To better understand the implications of this conclusion, we will consider several model light curves.

3.1. A Piecewise-Linear Function

Let us suppose that the source moves in the amplification field in a zig-zag fashion along its overall line of motion. To simplify the analysis, we also assume that the amplification does not vary in the transverse direction. Then, within each of the linear sections, the second derivative of the amplification coefficient is zero and the color of the source remains constant. Only when the source overlaps with a turning point is the assumption that the variations of the amplification function are smooth violated, giving rise to small variations in the color. The larger the radius of the source, the greater the degree of overlap. Figure 2 presents numerical calculations for this type of variability with a Gaussian source in accordance with the general formula (1). The variability of the point source was specified in the form $\mu_{\rm p} = 1 + 0.5f(x)$, where the function $f(x)$ was chosen to be $\ldots, x+4, -x-2, x, -x+2, x-4, \ldots$ for the intervals $x = \ldots, [-5,-3], [-3,-1], [-1,1], [1,3], [3,5], \ldots$, respectively. The radii of the larger and smaller sources were 0.4 and 0.2.

3.2. A Sinusoidal Dependence

The second derivative of a sinusoid is proportional to the amplitude. Therefore, the intensity and color vary synchronously. Figure 3 presents numerical calculations for two Gaussian sources with radii of 1.0 and 0.5. The amplification field varies only along the direction of the source motion, in accordance with the formula $f(x) = 1 + 0.5\sin x$. In this case, an exact analytical formula for the amplification of an extended source can be derived.

Substituting the Gaussian distribution for a source with radius R and its center at the point x_0 in the general formula (1), we obtain

$$\mu_{\rm ext} = \frac{1}{\pi R^2}\int_{-\infty}^{+\infty} e^{-y^2/R^2}dy \qquad (19)$$
$$\times \int_{-\infty}^{+\infty} e^{-(x-x_0)^2/R^2}\sin x dx.$$

Integrating over y and introducing the normalized coordinates $\xi = x/R$ and $\xi_0 = x_0/R$ yields

$$\mu_{\rm ext} = \frac{1}{\sqrt{\pi}}\int_{-\infty}^{+\infty} e^{-(\xi-\xi_0)^2}\sin(R\xi)d\xi \qquad (20)$$

or, taking into account the fact that the Laplacian of the exponential function is odd,

$$\mu_{\rm ext} = 2e^{-\xi_0^2}\int_0^\infty e^{-\xi^2}\,{\rm sh}(2\xi_0\xi)\sin(R\xi)d\xi. \quad (21)$$

This last integral is tabulated (see, for example, [19, (4.133.1)]). Therefore, we finally obtain

$$\mu_{\rm ext} = e^{-R^2/4}\sin x_0. \quad (22)$$

Note that, with harmonic light-curve variations, it is very difficult to differentiate between variability due to microlensing and to variable extinction, since color variations due to absorption are also proportional to the intensity.

3.3. A Point Mass

Let us proceed to the more realistic situation of a point-mass gravitational lens. The amplification of a point source f over the entire plane is described by the relation

$$\mu_{\rm p} = \frac{r^2+2}{r\sqrt{r^2+4}}. \quad (23)$$

The Laplacian of this function can most conveniently be calculated in polar coordinates:

$$\Delta\mu = \frac{1}{r}\frac{\partial}{\partial r}\left(r\frac{\partial\mu}{\partial r}\right) \quad (24)$$
$$= -\frac{8}{r}\frac{\partial}{\partial r}\left(\frac{1}{r(r^2+4)^{3/2}}\right) = \frac{32(r^2+1)}{r^3(r^2+4)^{5/2}}.$$

The Laplacian turns out to be positive at any point of the plane. This means that a larger source undergoes higher amplification. Therefore, if the size of the radiating region of the quasar increases with the wavelength, the effect of a point-mass gravitational lens is to redden the image. This is illustrated by Fig. 4a, which shows the variations for Gaussian sources passing near a lens, with the impact parameter equal to one Einstein radius. The radius of the larger source is 0.5 of the Einstein radius, while that of the smaller source is 0.25 of the Einstein radius.

Only when the source disk substantially overlaps the point mass—i.e., at the point where there is a discontinuity in the derivatives, violating the conditions of applicability for the approximation used—does the amplification of the smaller source begin to exceed that of the larger source so that the source becomes bluer (Fig. 4b).

For a uniform disk, we can compare the approximate solution with the exact solution obtained in [20]. Substituting (24) into (12), we obtain an expansion for the amplification in a series in the source radius:

$$\mu_{\rm ext} = \frac{r^2+2}{r\sqrt{r^2+4}} + \frac{4(r^2+1)}{r^3(r^2+4)^{5/2}}R^2 + \dots. \quad (25)$$

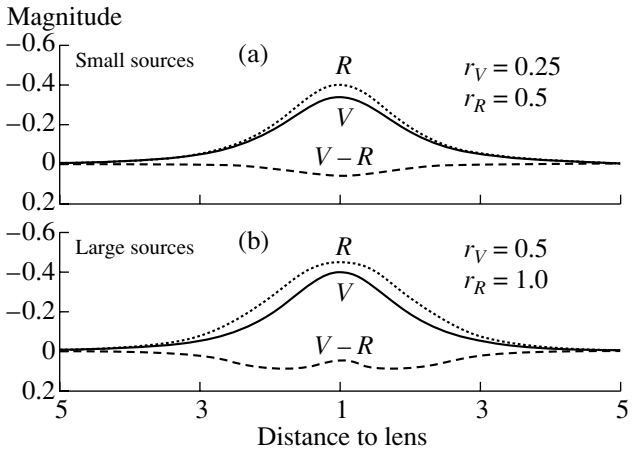

Fig. 4. Intensity and color variations produced by a point-like gravitational lens.

For comparison, we present the exact solution from [20]:

$$\mu_{\rm ext} = 1 + \frac{1}{\pi}\left[E\left(\frac{\pi}{2},k\right)\frac{r+R}{2R^2}\sqrt{4+(r-R)^2}\right. \quad (26)$$
$$- F\left(\frac{\pi}{2},k\right)\frac{r-R}{R^2}\frac{4+\frac{(r^2-R^2)}{2}}{\sqrt{4+(r-R)^2}}$$
$$\left. + \Pi\left(\frac{\pi}{2},n,k\right)\frac{2(r-R)^2}{R^2+(r+R)^2}\frac{1+R^2}{\sqrt{4+(r-R)^2}}\right],$$

where

$$n = \frac{4rR}{(r+R)^2}, \qquad k = \sqrt{\frac{4n}{4+(r-R)^2}}. \quad (27)$$

The expansion of the exact solution in a series in the disk radius coincides with our approximation.

3.4. A Rectilinear Caustic Fold

In the vicinity of a caustic, the basic assumption of the smoothness of the function becomes violated, and the approximation for the extended source is valid only when the source does not overlap with the caustic. However, the approximation used here remains valid within a restricted region.

Near a rectilinear caustic fold, the amplification coefficient for a point source depends only on its distance x to the caustic. This dependence has the very simple form

$$\mu_{\rm p} = 1/\sqrt{x}. \quad (28)$$

Differentiating (28) in x twice and substituting the result into (15) yields an approximate formula for the

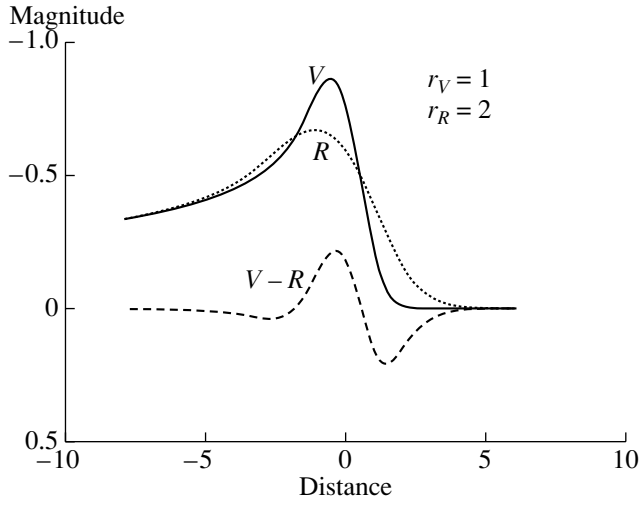

Fig. 5. Variations of the intensity and color in the vicinity of a rectilinear caustic fold.

amplification of a Gaussian source in the vicinity of the caustic:

$$\mu_{\text{ext}} = \frac{1}{\sqrt{x}} + \frac{3}{16}\frac{R^2}{x^{5/2}} + \dots . \qquad (29)$$

In the approximation (29), extended sources are amplified more strongly and the color becomes redder. This dependence of the amplification coefficient (28) makes it possible to take the initial integral (1) in the explicit form [21]

$$\mu_{\text{ext}} = 2^{-1/4}R^{-1/2}e^{-x^2/2R^2}D_{-1/2}\left(-2^{1/2}\frac{x}{R}\right). \quad (30)$$

Expansion of the function of the parabolic cylinder into a series in large values of the argument

$$D_{-1/2}(z) = e^{-z^2/4}z^{-1/2}\left(1 + \frac{3}{8z^2} + \dots\right) \qquad (31)$$

transforms (30) into (29).

We can see from Fig. 5 that the series expansion of the amplification coefficient is correct only when the source is a substantial distance from the caustic, $x < -3$.

4. ESTIMATION OF A QUASAR RADIUS FROM OBSERVATIONS

The technique developed here is based on the correlation between the color index and the second time derivative of the light curve. Therefore, it requires regular, long-term observations carried out in several filters. The only multiwavelength, long-term monitoring program of gravitational lenses carried out to date is the series of NOT observations of Q2237+0305 [22]. Unfortunately, the infrequency of simultaneous observations in the two filters used ($\sim$20 points for 4 years), their irregularity, and the photometric accuracy of the observations make it impossible to calculate the dynamics of variations of the second derivative.

It has become realistic to obtain regular observations of Q2237+0305 in the last few years with the monitoring program started by the OGLE group [23, 24]. However, these observations are carried out only in the V filter.

Simultaneously with the OGLE observations, we carried out independent observations of Q2237+0305 (primarily, in the R filter) at the Maĭdanak Observatory in the second half of 1997 [25]. A joint analysis of these two sets of observations provides the fundamental possibility of analyzing the color variations of the components.

During the second half of 1997, component A underwent the largest variations; therefore, we will restrict our consideration to its variability. Figure 6 presents the OGLE and Maĭdanak observations. Let us consider the evolution of the light curves during the time of the observations. Over about 200 days, the color of image A, $\Delta m(V-R)$, changed from zero at the beginning of the period to $\sim 0.1^m$ at the end; i.e., the image became redder. The second derivative estimated from the V data is clearly positive. Precisely such a dependence is expected from our theoretical approximation.

To obtain quantitative estimates, we will introduce a few simplifying assumptions. Let us suppose that the size of the quasar in V is substantially smaller than in R so that the V light curve can be considered a realization of amplification of a point source. We can then write one of the formulas for the amplification of an extended source, for example (15), for two times,

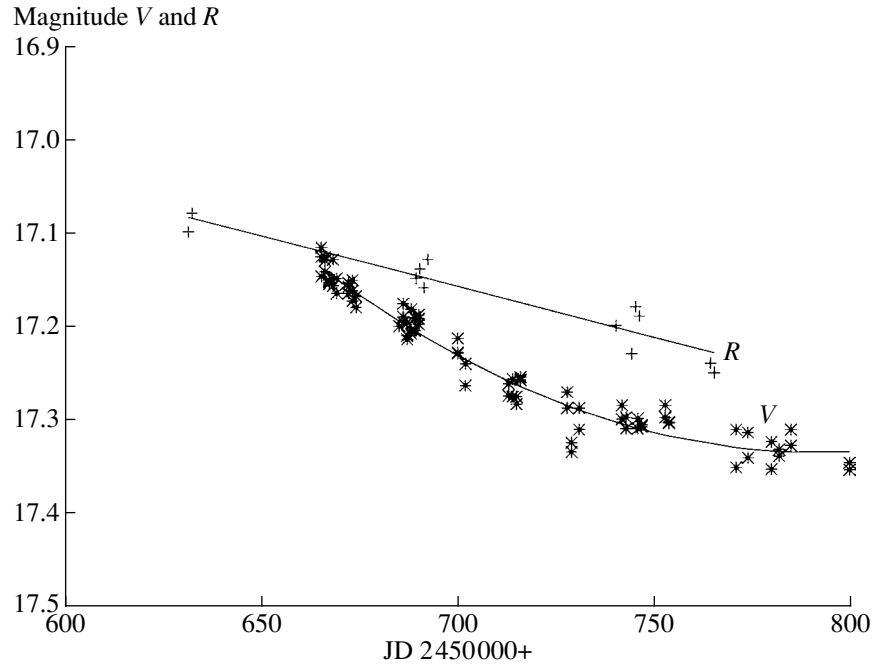

Fig. 6. Variability of the image of Q2237+0305A in the second half of 1997, based on OGLE V observations and Maĭdanak R observations.

for example, at the beginning and end of the observations:

$$\mu_{R1} = \mu_{V1} + \Delta\mu_{V1}\frac{R^2}{4}, \qquad (32)$$
$$\mu_{R2} = \mu_{V2} + \Delta\mu_{V2}\frac{R^2}{4}.$$

We now divide the second equation by the first, taking into account the fact that the relative variations of the amplification during the time of the observations are substantially smaller than unity:

$$\frac{\mu_{R2}}{\mu_{R1}} = \frac{\mu_{V2} + \Delta\mu_{V2}\frac{R^2}{4}}{\mu_{V1} + \Delta\mu_{V1}\frac{R^2}{4}} \qquad (33)$$
$$\approx \frac{\mu_{V2}}{\mu_{V1}}\left(1 + \left(\frac{\Delta\mu_{V2}}{\mu_{V2}} - \frac{\Delta\mu_{V1}}{\mu_{V1}}\right)\frac{R^2}{4}\right).$$

We will estimate the Laplacians from the second derivative along the direction of motion of the sources and assume that the second derivative was zero at the beginning of the observations. We can then estimate the radius of the quasar in the R filter based only on the observed values:

$$R \approx 2\left[\frac{\mu_{V2}}{\Delta\mu_{V2}}\left(\frac{\mu_{R2}}{\mu_{R1}} - \frac{\mu_{V2}}{\mu_{V1}}\right)\right]^{1/2}. \qquad (34)$$

The quantity in the inner parentheses can be estimated if we take into account the smallness of the variations of the amplification during the observation period:

$$\frac{\mu_{R2}}{\mu_{R1}} - \frac{\mu_{V2}}{\mu_{V1}} \approx (1 - dm_{R21}) \qquad (35)$$
$$- (1 - dm_{V21}) \sim 0.1^m.$$

The amplification for component A μ_{V1} derived from the models for this gravitational lens is about five, and the second derivative can be estimated from the difference of the slopes of the light curve at the end and beginning of the observations:

$$\Delta\mu_{V2} = \frac{\frac{d\mu_2}{dt} - \frac{d\mu_1}{dt}}{dt} \sim 10^{-4}\ \text{day}^{-2}. \qquad (36)$$

Substituting these values into (34), we obtain

$$R = 2\left[\frac{5}{10^{-4}\ \text{day}^{-2}} \times 0.1\right]^{1/2} \approx 140\ \text{day}. \qquad (37)$$

To make the translation from time measurements to linear units, we use the limit for the source velocity derived in [26]: $v \leq 500$ km/s. Then, 140 days corresponds to an upper limit for the radius of the quasar $R \leq 3 \times 10^{15}$ cm.

These calculations for the radius can be considered only very approximate order-of-magnitude estimates. Note, however, that this radius is in rather good agreement with other estimates for the source radius in this system calculated using completely different methods [27].

5. CONCLUSION

We have developed a method making it possible to relate color variations in images of gravitationally-lensed quasars and the second derivative of the light curve. Our approach is based on two main assumptions:

(1) the brightness distribution in the quasars is symmetrical;

(2) variations of the amplification coefficient are smooth on scales of the order of the source radius.

The assumed symmetry of the brightness distribution could be violated, for example, by rapid rotation of the accretion disk and the resulting Doppler shifts, which would lead to nonzero first moments of the brightness distribution in the source. In this situation, linear gradients in the expansion of the amplification field (2) must be taken into account. These linear gradients could be manifest observationally as a correlation between variations of the color index and the first derivative of the light curve, i.e., the rate of variations in the intensity.

The second condition is violated in the vicinity of caustics. In such regions, our approach is of limited value, and other methods must be used.

In conclusion, we stress that multiwavelength monitoring of gravitational lenses is highly desirable. If the above approximations are valid, more accurate determinations of the correlation between color-index variations and the second derivative of the light curve will enable estimation of the sizes of the lensed quasars at different wavelengths.

REFERENCES

1. R. Kayser, S. Refsdal, and R. Stabell, Astron. Astrophys. **166**, 36 (1986).
2. H. K. C. Yee, Astron. J. **95**, 1331 (1988).
3. M. J. Irwin, R. L. Webster, P. C. Hewett, *et al.*, Astron. J. **98**, 1989 (1989).
4. R. Racine, Astron. J. **102**, 454 (1991).
5. J. Wambsganss and B. Paczyński, Astron. J. **102**, 864 (1991).
6. H.-W. Rix, D. P. Schneider, and J. N. Bahcall, Astron. J. **104**, 959 (1992).
7. V. G. Vakulik, V. N. Dudinov, A. P. Zheleznyak, *et al.*, Astron. Nachr. **318**, 73 (1997).
8. I. Burud, R. Stabell, P. Magain, *et al.*, Astron. Astrophys. **339**, 701 (1998).
9. D. Nadeau, R. Racine, R. Doyon, and G. Arboit, Astrophys. J. **527**, 46 (1999).
10. C. S. Kochanek, E. E. Falco, C. D. Impey, *et al.*, Astrophys. J. **543**, 131 (2000).
11. M. Blanton, E. L. Turner, and J. Wambsganss, Mon. Not. R. Astron. Soc. **296**, 1223 (1998).
12. A. Gould, Astrophys. J. Lett. **421**, L71 (1994).
13. M. B. Bogdanov and A. M. Cherepashchuk, Pis'ma Astron. Zh. **21**, 570 (1995) [Astron. Lett. **21**, 505 (1995)].
14. M. D. Albrow, J. An, J.-P. Beaulieu, *et al.*, Astrophys. J. **549**, 759 (2001).
15. A. F. Zakharov, *Gravitational Lenses and Microlenses 328* [in Russian] (Yanus-K, Moscow, 1997).
16. A. F. Zakharov and M. V. Sazhin, Usp. Fiz. Nauk **168**, 1041 (1998) [Phys. Usp. **41**, 945 (1998)].
17. P. Schneider, J. Ehlers, and E. Falco, *Gravitational Lenses* (Springer-Verlag, Berlin, 1992).
18. A. Gould and J. Miralda-Escudé, Astrophys. J. Lett. **483**, L13 (1997).
19. I. S. Gradshteyn and I. M. Ryzhik, *Table of Integrals, Series, and Products 1108* (Nauka, Moscow, 1971; Academic, New York, 1980).
20. H. J. Witt and S. Mao, Astrophys. J. **430**, 505 (1994).
21. P. Schneider and A. Weiss, Astron. Astrophys. **171**, 49 (1987).
22. R. Østensen, S. Refsdal, R. Stabell, *et al.*, Astron. Astrophys. **309**, 59 (1996).
23. P. R. Woźniak, C. Alard, A. Udalski, *et al.*, Astrophys. J. **529**, 88 (2000).
24. P. R. Woźniak, A. Udalski, M. Szymański, *et al.*, Astrophys. J. Lett. **540**, L65 (2000).
25. P. V. Bliokh, V. N. Dudinov, V. G. Vakulik, *et al.*, Kinematika Fiz. Nebesnykh Tel **15**, 338 (1999).
26. J. S. B. Wyithe, R. L. Webster, and E. L. Turner, Mon. Not. R. Astron. Soc. **309**, 261 (1999).
27. V. N. Shalyapin, Pis'ma Astron. Zh. **27**, 180 (2001) [Astron. Lett. **27**, 150 (2001)].

Translated by K. Maslennikov

Astronomy Reports, Vol. 46, No. 6, 2002, pp. 443–450. Translated from Astronomicheskiĭ Zhurnal, Vol. 79, No. 6, 2002, pp. 492–500.

Equilibrium After Violent Relaxation in Numerical Dynamical Models of Open Clusters

V. M. Danilov

Astronomical Observatory, Ural State University, pr. Lenina 51, Yekaterinburg, 620083 Russia

Received June 1, 2001; in final form, November 23, 2001

Abstract—Models of open clusters in a state of equilibrium in the space of the three parameters of the stellar motion and simultaneously far from virial equilibrium are analyzed. A formula for the phase-space stellar number density in such cluster models is derived, as well as formulas for the integrated and differential energy distributions of the phase-space volume occupied by cluster stars per unit stellar mass. These three quantities are computed for several times exceeding the time for violent relaxation of the cluster model. The phase-space density function obtained is used to compute the distribution of the absolute values of stellar velocities for the cluster model considered. © *2002 MAIK "Nauka/Interperiodica"*.

1. INTRODUCTION

The dynamic evolution of open-cluster models that are not stationary in the field of regular forces [1] by the end of the first relaxation time τ_{vr} are characterized by an equilibrium distribution of stars in the space of the three parameters of the stellar motion: ε, l, and ε_ζ (the energy, angular momentum, and energy of the stellar motion perpendicular to the Galactic plane, with all three quantities measured per unit stellar mass). The open-cluster models of [1] (hereafter, Paper 1) do not attain virial equilibrium with increasing time t, and the virial coefficient continues to oscillate with almost constant amplitude and period at times $t > \tau_{vr}$. Although the open-cluster models of Paper 1 are quite far from virial equilibrium (and, consequently, from statistical and thermodynamical equilibrium [2]), the stellar distributions $f(\varepsilon, \varepsilon_\zeta, l)$, $\chi(\varepsilon)$, $\omega(\varepsilon_\zeta)$, and $\psi(l)$ in the parameters ε, ε_ζ, and l are maintained at $t > \tau_{vr}$ over time intervals Δt of the order of the period P_r of the oscillations of the regular field. The mean values $\langle\varepsilon\rangle$, $\langle\varepsilon_\zeta\rangle$, and $\langle l\rangle$ averaged over several stars and the dispersions σ_ε, $\sigma_{\varepsilon,\zeta}$, and σ_l of the deviations of ε, ε_ζ, and l from $\langle\varepsilon\rangle$, $\langle\varepsilon_\zeta\rangle$, and $\langle l\rangle$ in the intervals of ε, ε_ζ, and l corresponding to these stars are also conserved in these model. (This is true for stars with clustercentric distances $r < R_t^-$, where R_t^- is the tidal radius for stars with retrograde orbits in the cluster [1].) The dispersions σ_ε, $\sigma_{\varepsilon,\zeta}$, and σ_l can serve to characterize the intervals $\Delta\varepsilon$, $\Delta\varepsilon_\zeta$, and Δl used in Paper 1 when constructing the distributions $\chi(\varepsilon)$, $\omega(\varepsilon_\zeta)$, and $\psi(l)$. In Paper 1, we also estimated the local time for relaxation of the cluster models to phase-space equilibrium t_r. Such a relaxation transition in the open-cluster models of Paper 1 results in a core–halo structure and a sort of oscillatory process in which the distribution of stars in coordinate–velocity space and the regular-force potential of the cluster vary periodically (or almost periodically) with time. According to Paper 1, at $t > \tau_{vr}$, the number of stars $\Delta N(\varepsilon)$ in the interval $\Delta\varepsilon$ remains almost constant during time intervals P_r, because the distribution $\chi(\varepsilon)$ and the quantity σ_ε are preserved over time intervals $\Delta t = P_r$. We can write for small $\Delta\varepsilon$

$$dN = \chi(\varepsilon)d\varepsilon \simeq \text{const}. \qquad (1)$$

Let $\Gamma(\varepsilon)$ be the phase-space volume occupied by cluster stars with energies $\varepsilon' \le \varepsilon$, and $\gamma(\varepsilon)$ be the phase-space volume occupied by stars with energies $\varepsilon' \in [\varepsilon, \varepsilon + d\varepsilon]$, divided by the energy interval $d\varepsilon$:

$$\Gamma(\varepsilon) = \int_{-\infty}^{\varepsilon} \gamma(\varepsilon')d\varepsilon', \quad \gamma(\varepsilon) = \frac{d\Gamma(\varepsilon)}{d\varepsilon}. \qquad (2)$$

The functions $\Gamma(\varepsilon)$ and $\gamma(\varepsilon)$ are the integrated and differential distributions of the energy ε of the phase-space volume occupied by stars from the corresponding ε intervals (see above). We have $\gamma(\varepsilon) \neq 0$ for cluster stars with energies ε (for sufficiently large $\Delta\varepsilon$ intervals), implying that $\gamma(\varepsilon) > 0$ and $\frac{d\Gamma(\varepsilon)}{d\varepsilon} > 0$. In this case, $\Gamma(\varepsilon)$ is a monotonically increasing function of ε for all $\varepsilon \in [\varepsilon_1, \varepsilon_n]$, where $\varepsilon_1, \varepsilon_n$ are the minimum and maximum energy ε of the cluster stars, respectively.

In statistical physics, functions of the form (2) are commonly used to make the transition from a distribution of particle energies to the corresponding phase-space distribution for the same particles (see,

1063-7729/02/4606-0443$22.00

e.g., [3, p. 46]). Since $\chi(\varepsilon) \simeq$ const and $\sigma_\varepsilon \simeq$ const in time intervals P_r, (1) and (2) yield the formula

$$dN(\Gamma(\varepsilon)) = \frac{\chi(\varepsilon)}{\gamma(\varepsilon)} d\Gamma(\varepsilon) \simeq \text{const}, \quad (3)$$
$$\frac{d\Gamma(\varepsilon)}{\gamma(\varepsilon)} \simeq \text{const}.$$

It thus follows that, as a result of the relaxation transition, a balance of transitions between some of the phase-space cells is established in the cluster models of Paper 1 over a time τ_{vr}. In this case, the number of particles entering a phase-space cell occupied by particles with energy ε is approximately equal to the number of stars leaving this cell (since $dN(\Gamma(\varepsilon)) \simeq$ const). Let $d\Gamma(\varepsilon) = d^3r d^3v$, where d^3r and d^3v are volume elements in coordinate ($\mathbf{r}$) and velocity ($\mathbf{v}$) space, respectively (here and below, $\mathbf{r}$ and $\mathbf{v}$ denote the radius vector and velocity vector of a cluster star). According to the second of conditions (3), the oscillatory process that is established in the models of Paper 1 at $t > \tau_{vr}$ obeys the condition $d^3r \simeq \text{const} \times \gamma(\varepsilon)/d^3v$. In the cluster models considered here, we can assume that, to first approximation, the function $\gamma(\varepsilon)$ varies little over one oscillation period P_r of the regular field (see Fig. 2 below). Therefore, the oscillations in coordinate ($\mathbf{r}$) and velocity ($\mathbf{v}$) space are in antiphase, and their amplitude ratio depends on $\gamma(\varepsilon)$.

Our previous statistical description of open-cluster models in Paper 1 is not complete, because the numerical simulations described failed to yield an equilibrium phase-space density function corresponding to a state of equilibrium in the space of the coordinates ε, ε_ζ, and l attained in the model. According to the results of Paper 1, $\varepsilon = \varepsilon(\mathbf{r}, \mathbf{v})$. We now substitute $\varepsilon(\mathbf{r}, \mathbf{v})$ into the first relation of (3) to obtain the equilibrium phase-space density:

$$F_0(\mathbf{r}, \mathbf{v}) d^3r d^3v \quad (4)$$
$$= \frac{\chi(\varepsilon(\mathbf{r}, \mathbf{v}))}{\gamma(\varepsilon(\mathbf{r}, \mathbf{v}))} d\Gamma(\varepsilon(\mathbf{r}, \mathbf{v})) \simeq \text{const}.$$

To analyze the specifics of the oscillatory process that develops in the open-cluster models of Paper 1 and derive the equilibrium phase-space density $F_0(\mathbf{r}, \mathbf{v})$, we must find the differential distribution $\gamma(\varepsilon)$ of the phase-space volume in ε.

According to (4), a system with such a phase-space density goes through an entire series of recurrent states in the course of its evolution, which is typical of autowave processes [4]. In reality, the periodically recurring states (with period P_r) in the cluster models of Paper 1 vary slightly over time intervals exceeding P_r, since these models slowly evolve when averaged over the period P_r (e.g., due to dissipation of stars and energy from the cluster). The process established during a time τ_{vr} in the models of Paper 1 must be close to an autowave process. According to Vasil'ev *et al.* [4], the development of an autowave process is a characteristic feature of self-organizing systems that are far from thermodynamical equilibrium. In the models of Paper 1, the cluster stars occupy the entire volume below the cluster's tidal surface, which is determined by the gravitational field of the Galaxy. Therefore, the cluster-averaged mass density in these models (and in open clusters) is close to $\rho = 3M/(4\pi(R_t^-)^3)$, where M is the cluster mass. The Jeans wavelength λ_J of a uniform gravitating stellar system with density ρ and an rms velocity for the peculiar stellar motions of $\langle v \rangle$ is $\lambda_J \simeq 4R_t^-$ if ρ and $\langle v \rangle$ are derived from the data of Paper 1. Here, $\lambda_J = \langle v \rangle \sqrt{\pi/(G\rho)}$ (see, e.g., formula (15.42) in [5, p. 125]), and G is the gravitational constant. The wavelength λ_J is of the order of the cluster size (diameter) $L \simeq 2R_t^-$. According to Weinberg [6], in this situation, small random density fluctuations can easily trigger the stochastic excitation of large-scale oscillations in the system. Weinberg [6] found that these large-scale density fluctuations produce accelerations that are independent of the mass of the star, as is the case with violent relaxation [7] and the cluster models of Paper 1 with the phase-space density (4). One of the most remarkable features of open-clusters models with the phase-space density (4) is the synchronization of density oscillations on various scales developing within them.

In view of possible astrophysical applications, it is of interest to analyze the specific nature of the oscillation process that develops in the cluster models of Paper 1 and to determine their equilibrium phase-space density. Integrating this phase-space density over velocity space $\mathbf{v}$ will enable us to determine the distribution of stars in the coordinate space $\mathbf{r}$. Theoretically, a comparison of this distribution with those observed in real open clusters can be used to derive the parameters of the equilibrium distribution $f(\varepsilon, \varepsilon_\zeta, l)$ for the cluster stars (see (5) in Paper 1). Using these parameters and integrating $F_0(\mathbf{r}, \mathbf{v})$ over the spatial coordinates $\mathbf{r}$, we can derive the distribution of stellar velocities in an observed cluster. The results of this analysis may have other applications, depending on the accuracy of the parameters of the distribution $f(\varepsilon, \varepsilon_\zeta, l)$.

The aim of the current work is to determine the functions $\gamma(\varepsilon)$ and $F_0(\mathbf{r}, \mathbf{v})$ for the open-cluster models of Paper 1.

2. PRINCIPAL FORMULAS AND EQUATIONS

To compute the functions $\gamma(\varepsilon)$ and $F_0(\mathbf{r}, \mathbf{v})$, we used the results of our earlier numerical integration

of 500 equal-mass stars moving in the combined field of the cluster and the Galaxy (see Paper 1; in that paper, we analyzed models for a cluster moving in the Galactic plane in a circular orbit with Galactocentric radius $R_0 = 8200$ pc).

It is more convenient to compute the function $\gamma(\varepsilon)$ by performing all necessary phase-space integrations in the spherical coordinate system (r, θ, φ) (in coordinate space $\mathbf{r}$), taking into account the dependence of ε on the absolute value of the star's velocity v (in velocity space $\mathbf{v}$; see Paper 1):

$$\varepsilon = \frac{v^2}{2} - U(\mathbf{r}) + \frac{r^2}{2}(\alpha_1 \sin^2\theta\cos^2\varphi + \alpha_3\cos^2\theta) = H(\mathbf{r},\mathbf{v}). \quad (5)$$

Here, the coordinates (r, θ, φ) are related to the Cartesian coordinates (ξ, η, ζ) used in Paper 1 in the usual way, r is the distance from the cluster center of mass (the absolute value of the vector $\mathbf{r}$), φ the angle in the (ξ, η) plane between the positive ξ axis and the projection of the radius vector $\mathbf{r}$ onto the (ξ, η) plane, θ the angle between the positive ζ axis and the radius vector $\mathbf{r}$ ($\theta \in [0, \pi]$ and $\varphi \in [-\pi, +\pi]$), $U(\mathbf{r})$ the gravitational potential of the cluster, and $\alpha_1 = \text{const}$ and $\alpha_3 = \text{const}$, as defined in Paper 1 for the model of the potential of the regular forces of the Galaxy [8] ($\alpha_1 < 0$ and $\alpha_3 > 0$).

The phase-space volume $\Gamma(\varepsilon)$ occupied by cluster stars with energies $\varepsilon' \le \varepsilon$ can be determined as follows:

$$\Gamma(\varepsilon) = \int d\varphi \int r^2 dr \times \int\limits_{\varepsilon_1 \le H(\mathbf{r},\,\mathbf{v}) \le \varepsilon} \sin\theta d\theta \int 4\pi v^2 dv, \quad (6)$$

where ε_1 is defined in the explanation of (2) and the integration in (6) is to be performed over the phase-space domain satisfying the constraints on the function $H(\mathbf{r}, \mathbf{v})$ indicated in (6). Anselm [3, p. 47] uses the same method to compute the phase-space volume $\Gamma(\varepsilon)$. The quantity $\Delta\Gamma(\varepsilon)$ can be determined either as $\Delta\Gamma(\varepsilon) = \Gamma(\varepsilon + \Delta\varepsilon) - \Gamma(\varepsilon)$ or as the integral (6) with the integration domain satisfying the conditions $\varepsilon \le H(\mathbf{r}, \mathbf{v}) \le \varepsilon + \Delta\varepsilon$. Due to the incompleteness of the phase-space mixing that occurs by time t, the cluster stars will not yet occupy all phase-space domains satisfying the conditions $\varepsilon \le H(\mathbf{r},\, \mathbf{v}) \le \varepsilon + \Delta\varepsilon$. Therefore, the integration in (6) should be performed over the phase-space domain bounded by a surface constructed using the phase-space coordinates of stars satisfying the above conditions on the function $H(\mathbf{r}, \mathbf{v})$. Following (6), we write

$$\Gamma(\varepsilon) = \int\limits_{\varphi_1(\varepsilon)}^{\varphi_2(\varepsilon)} d\varphi \int\limits_{r_1(\varepsilon,\varphi)}^{r_2(\varepsilon,\varphi)} r^2 dr \times \int\limits_{\theta_1(\varepsilon,\varphi,r)}^{\theta_2(\varepsilon,\varphi,r)} \sin\theta \frac{4\pi}{3}(v^3 - {v_1}^3) d\theta, \quad (7)$$

where v is determined from (5) [(7) is written with the integration over v in (6) already performed]; $\varphi_{1,2}(\varepsilon)$, $r_{1,2}(\varepsilon, \varphi)$, and $\theta_{1,2}(\varepsilon, \varphi, r)$ are the minimum and maximum values of φ, r, and θ, respectively, for stars with energies $\varepsilon' \le \varepsilon$ and the specified values of the quantities in parentheses for $r_{1,2}, \theta_{1,2}$; and $v_1 = v_1(\varepsilon, \varphi, r, \theta)$ is the minimum value of v for stars with energies $\varepsilon' \le \varepsilon$ and the specified φ, r, θ.

The parameter $\Delta\varepsilon$ in (6) is small compared to $\varepsilon_n - \varepsilon_1$. In this case, we have, in accordance with (2), $\Delta\Gamma(\varepsilon) \simeq \gamma(\varepsilon)\Delta\varepsilon$. This relation and (7) enable us to approximately determine the function $\gamma(\varepsilon)$.

The distribution of stars $g(v)$ in the absolute value of the velocity v for the open-cluster models of Paper 1 can be written

$$g(v)dv = 4\pi v^2 I(v) dv, \quad (8)$$

$$I(v) = \int\limits_{\phi_1(v)}^{\phi_2(v)} d\varphi \int\limits_{\lambda_1(v,\varphi)}^{\lambda_2(v,\varphi)} r^2 dr \times \int\limits_{\vartheta_1(v,\varphi,r)}^{\vartheta_2(v,\varphi,r)} \frac{\sin\theta\chi(\varepsilon(r,\varphi,\theta,v))d\theta}{\gamma(\varepsilon(r,\varphi,\theta,v))},$$

where $\phi_{1,2}(v)$, $\lambda_{1,2}(v, \varphi)$, and $\vartheta_{1,2}(v, \varphi, r)$ are the minimum and maximum values of φ, r, and θ, respectively, for stars with the specified values of the quantities in parentheses at $\phi_{1,2}$, $\lambda_{1,2}$, and $\vartheta_{1,2}$.

The integration in (8) is performed for stars with the specified v and energies $\varepsilon \in [\varepsilon_1, \varepsilon_n]$, where ε_1 and ε_n are defined in the explanation of formulas (2). The order of integration in (7) and (8) is determined by the shape of the domain in (r, φ) space occupied by the stars of the cluster model by the time t (Fig. 1). On the (r, φ) plane in Fig. 1, the stars concentrated near $\varphi \simeq -0.7$ rad and $\varphi \simeq 2.5$ rad have large r values and escape from the cluster, producing two spiral-like arms in the Galactic plane located along the stellar orbits shown, e.g., in Fig. 1 of [9].

The radial distributions of the number of stars $N(r)$ and stellar density $n(r)$ in the open cluster models of Paper 1 can be written

$$N(r)dr = 4\pi r^2 n(r) dr, \quad (9)$$

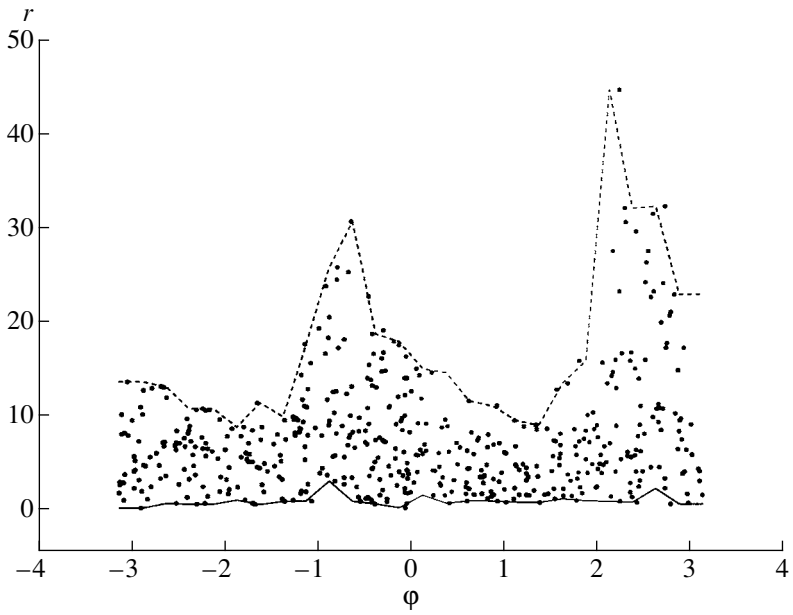

Fig. 1. Positions of stars in cluster model 2 of Paper 1 shown in the (φ, r) plane at time $t = 1.4\tau_{vr}$. φ and r are in radians and parsecs, respectively.

$$n(r) = \int\limits_{\nu_1(r)}^{\nu_2(r)} v^2 dv \int\limits_{\overline{\phi}_1(r,v)}^{\overline{\phi}_2(r,v)} d\varphi \times \int\limits_{\overline{\vartheta}_1(r,v,\varphi)}^{\overline{\vartheta}_2(r,v,\varphi)} \frac{\sin\theta \chi(\varepsilon(r,\varphi,\theta,v))d\theta}{\gamma(\varepsilon(r,\varphi,\theta,v))},$$

where $\nu_{1,2}(r)$, $\overline{\phi}_{1,2}(r,v)$, and $\overline{\vartheta}_{1,2}(r,v,\varphi)$ are the minimum and maximum values of v, φ, and θ, respectively, for stars with the specified values of the quantities in parentheses at $\nu_{1,2}$, $\overline{\phi}_{1,2}$, $\overline{\vartheta}_{1,2}$, and $\vartheta_i(v,\varphi,r) = \overline{\vartheta}_i(r,v,\varphi)$, $i = 1, 2$.

The integration over φ and θ in (9) takes into account deviations from spherical symmetry in the stellar density distribution $n(\mathbf{r})$ (in $\mathbf{r}$ space), which increase with r at the periphery of the cluster [because the phase-space density distribution $\chi(\varepsilon)/\gamma(\varepsilon)$ in the open-cluster model considered depends on ε and the dependence of ε on the spatial coordinates has the form (5)].

3. DETERMINATION OF THE INTEGRATION-DOMAIN BOUNDARIES

We determined the boundaries of the (φ, r, θ) domain occupied by stars with energies $\varepsilon' \le \varepsilon$ by the time t separately for each ε from the given series ε_i specified on the interval $[\varepsilon_1, \varepsilon_n]$. After finding $\varphi_{1,2}(\varepsilon_i)$ for stars with energies $\varepsilon' \le \varepsilon_i$, we define a grid of φ_j in the interval $[\varphi_1(\varepsilon_i),\ \varphi_2(\varepsilon_i)]$. The quantities $r_{1,2}(\varepsilon_i, \varphi_j)$ are determined from the n_s stars nearest to the given grid point φ_j in the parameter space φ ($n_s \ge 2$). We assumed that the dependences $r_{1,2} = r_{1,2}(\varepsilon_i, \varphi)$ are linear within the intervals between two neighboring grid points φ. The dashed and solid curves in Fig. 1 show the upper and lower boundaries of the domain of integration over r in (7) for $\varepsilon' \le (39\varepsilon_2 + \varepsilon_1)/40$ derived using the above technique. As the interval $\Delta\varphi$ narrows (and the number of grid points in φ increases), the number of stars outside this integration domain in the (φ, r) plane decreases. Unfortunately, increasing the number of grid points in φ, r, and θ drastically increases the computer speed and disk space required for the computation. We therefore did not use very small intervals between adjacent points of the grids considered [we used grids with 26 equidistant points in each coordinate axis—φ, r, and θ—covering the domain accessible for stars satisfying the conditions in (7) and (8)]. Further increasing the number of grid points was difficult for technical reasons. Note that $\Gamma(\varepsilon)$ depends strongly on the accuracy of the upper boundary of the integration domain in r at the largest r (Fig. 1), since, according to (7), $\Gamma(\varepsilon) \sim (r_2^3 - r_1^3)$. The error introduced in $\Gamma(\varepsilon)$ due to the use of finite intervals $\Delta\varphi$ can be reduced by excluding the stars with the largest r.

We determined the boundaries of the integration domain in (7) and (8) at the points of the φ, r, and θ grids considered using the phase-space coordinates

of the cluster stars at time t, which we adopted from Paper 1.

We determined the boundaries for the integration over r in (1) for each $\varphi \in [\varphi_1(\varepsilon_i), \varphi_2(\varepsilon_i)]$ by linearly interpolating the tabulated relations $r_{1,2} = r_{1,2}(\varepsilon_i, \varphi)$ in φ. The boundaries for integration over θ in (7) for a point in (φ, r) space are determined using the formula for a two-dimensional linear interpolation obtained by applying a one-dimensional linear interpolation twice (i.e., by substituting the formula for the linear interpolation in φ into the interpolation formula in r). We derived the interpolation polynomial using the technique described by Korn and Korn [10, p. 596]. If one argument of the interpolated function of two variables is equal to its grid-point value, the resulting formula for the two-dimensional interpolation reduces to the usual formula for a linear one-dimensional interpolation in the other argument. In (7), $v_1(\varepsilon_i, \varphi, r, \theta)$ for a point in (φ, r, θ) space is determined using the three-dimensional interpolation formula obtained by applying the formula for a linear one-dimensional interpolation three times, in accordance with the technique described by Korn and Korn [10, p. 596]. If we have $v_1(\varepsilon, \varphi, r, \theta) > v$ during the computations, where v is determined using (5), we set $v_1(\varepsilon, \varphi, r, \theta)$ equal to precisely this v value in order to take into account the condition $v_1(\varepsilon, \varphi, r, \theta) \le v$ when using (7).

We computed values of $F(\varepsilon) = \chi(\varepsilon)/\gamma(\varepsilon)$ by linearly interpolating tabulated values of $F(\varepsilon)$ obtained for a number of ε. According to (4), $F(\varepsilon(\mathbf{r}, \mathbf{v})) = F_0(\mathbf{r}, \mathbf{v})$.

We used the ratio $\frac{n(\varepsilon)}{\Delta\varepsilon}$ as the function $\chi(\varepsilon)$, where $n(\varepsilon)$ is the number of stars in the interval $\varepsilon \in [\varepsilon, \varepsilon + \Delta\varepsilon]$. We obtained the stellar distribution $n(\varepsilon)$ in Paper 1 using the ε interval $\Delta\varepsilon$.

To compute the function $g(v)$ from (8), we used the same technique to determine the integration domain as for (7) (substituting the condition $\varepsilon' \le \varepsilon_i$ with the condition $v' \in [v_i, v_i + \Delta v]$). In this case, the construction of surfaces bounding the integration domain in (8) ends with finding $\vartheta_{1,2}(v, \varphi, r)$. These computations involve one- and two-dimensional interpolations exclusively, since, in constrast to the case of the integral (7), the integrand in (8) is determined beforehand and computed via a linear one-dimensional interpolation.

The errors introduced in the computed functions $\Gamma(\varepsilon)$ and $g(v)$ due to the inaccurate specification of the integration-domain boundaries in (7) and (8) should not be too large if the grid cells used in (φ, r, θ) space are not too small, since the stellar distribution $g(v)$ obtained using the $F(\varepsilon)$ function derived in the current paper is in approximate agreement with the stellar velocity distribution obtained directly from the stellar velocities in the cluster model considered.

4. COMPUTATION RESULTS AND DISCUSSION

We used (5)–(7) to compute the functions $\gamma(\varepsilon)$, $\Gamma(\varepsilon)$, and $F(\varepsilon)$ for several times $t/\tau_{vr} = 1.2$, 1.4, and 1.6 in the open-cluster models of Paper 1 (as in that paper, we have adopted $\tau_{vr} = 2.6\overline{t}_{cr}$, where $\overline{t}_{cr}$ is the mean crossing time for the cluster). Figures 2 and 3 show the results of our computations for cluster model 2 in Paper 1 (plots of $\gamma(\varepsilon), F(\varepsilon)$ for cluster model 1 in Paper 1 are similar to those shown, and we do not present them here).

According to Paper 1, the estimated times t_r for the relaxation of cluster models 1 and 2 to an equilibrium state with the phase-space density (4) are $t_r \simeq 0.5\tau_{vr}$ at the cluster center and $t_r \simeq 1.1\tau_{vr}$ and $t_r \simeq 1.5\tau_{vr}$ at the cluster periphery for models 1 and 2, respectively. By the time the models reach equilibrium in ε, ε_ζ, l space, $\gamma(\varepsilon)$ acquires the form of a mainly increasing function of ε. Since $\gamma(\varepsilon) > 0$ (Fig. 2), the phase-space volumes $\Gamma(\varepsilon)$ occupied by stars with energies $\varepsilon' \le \varepsilon$ increase monotonically with ε, and the phase-space volumes $\Delta\Gamma(\varepsilon)$ occupied by stars with energies $\varepsilon' \in [\varepsilon, \varepsilon + \Delta\varepsilon]$ mainly increase with ε. Thus, we have obtained a fully expected result. Stars with large energies ε can attain large clustercentric distances r and, according to our computations, can have high mean velocities $\overline{v}$ and large dispersions for the deviations of v from $\overline{v}$. Therefore, these stars mainly occupy large phase-space volumes $\Delta\Gamma(\varepsilon)$ in the open-cluster models. In the course of cluster evolution, some fraction of the stars with the highest energies escape from the cluster, increasing the corresponding phase-space volumes.

The function $F(\varepsilon)$ characterizing the equilibrium phase-space density of cluster stars within the interval $\Delta\Gamma(\varepsilon)$ mostly decreases with increasing ε (Fig. 3). The presence of isolated ε intervals in Fig. 3, where the monotonically decreasing behavior of $F(\varepsilon)$ is disrupted, is due to two factors. The first is specific features of the distribution of stellar energies $\chi(\varepsilon)$ (see the jumplike variations of the function $n(\varepsilon)$ as ε increases at some times t in Fig. 4a of Paper 1). The second factor is the disruption of the monotonic growth of $\gamma(\varepsilon)$ in some ε intervals due to the strong irregularity (stochastic shape, the presence of peaks, etc.) of the integration domains in (7). The integration-domain boundary's shape is due, among other things, to the fact that individual stars located far from the bulk of the cluster stars in (r, φ, θ) space are included in the integration [the shape of integration-domain boundaries in (7) is made

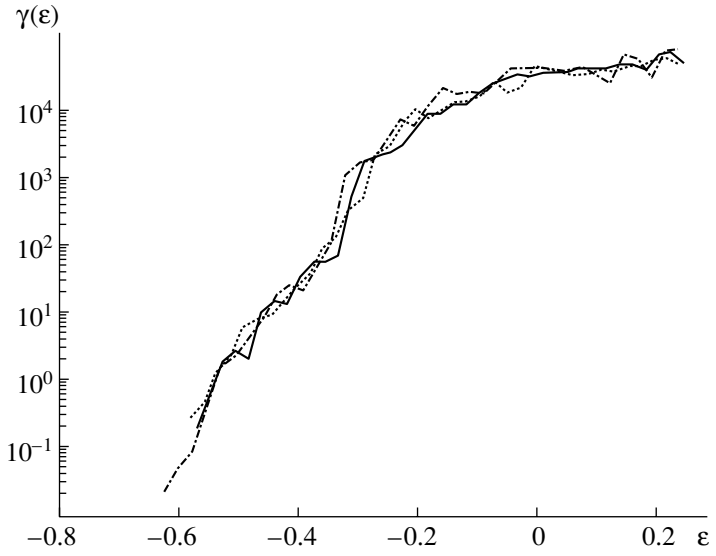

Fig. 2. Relations $\gamma = \gamma(\varepsilon)$ for times $t/\tau_{vr} = 1.2$ (solid curve); $t/\tau_{vr} = 1.4$ (dotted curve), and $t/\tau_{vr} = 1.6$ (dot–dashed curve). γ and ε are in $\mathrm{pc}^4/\mathrm{Myr}$ and $(\mathrm{pc}/\mathrm{Myr})^2$, respectively.

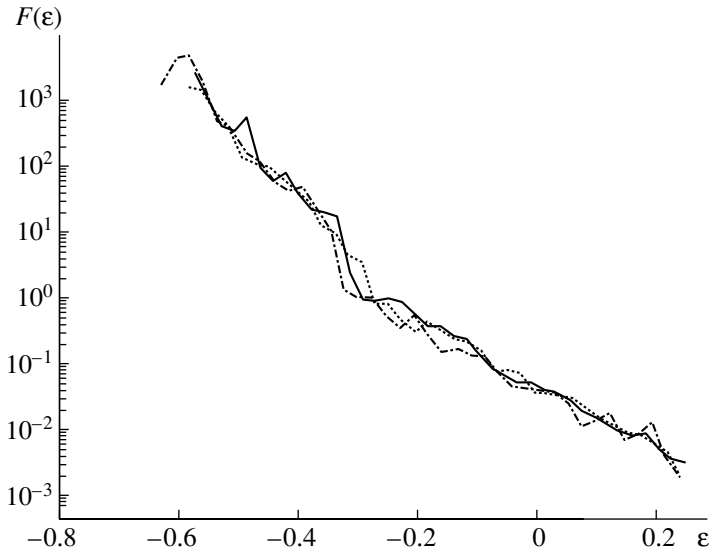

Fig. 3. Relations $F = F(\varepsilon)$ for times $t/\tau_{vr} = 1.2$ (solid curve); $t/\tau_{vr} = 1.4$ (dotted curve), and $t/\tau_{vr} = 1.6$ (dot–dashed curve). F and ε are in $\mathrm{Myr}^3/\mathrm{pc}^6$ and $(\mathrm{pc}/\mathrm{Myr})^2$, respectively.

especially complicated and distorted by individual stars that have traveled far from the cluster in r, e.g., as a result of an individual close stellar encounter or due to initial conditions favoring the dissipation of certain stars from the cluster]. The shapes of the integration-domain boundaries in (8) and (9) behave in a similar way. The small number of stars satisfying the boundary conditions in (φ, r, θ) and (v, φ, θ) space and the random nature of the arrangement of stars in the domains considered also contribute to the strong irregularity of the integration-domain boundaries in (7)–(9).

To a first approximation, the logarithm of $F(\varepsilon)$ at the cluster core (at $\varepsilon < -0.3$) and in the halo can be fitted by two linear relations $\ln F(\varepsilon) \simeq a_i + b_i\varepsilon$ $(i = 1, 2)$, derived by obtaining a least-squares fit to the data from the three curves shown in Fig. 3. The coefficients of the above relations for $\ln F(\varepsilon)$ for the time period from $1.2\tau_{vr}$ to $1.6\tau_{vr}$ are $a_1 = -6.37 \pm 0.32$, $b_1 = -24.02 \pm 0.72$ and $a_2 = -3.23 \pm 0.03$, $b_2 = -10.98 \pm 0.23$ in the core $(i = 1)$ and halo, respectively. The straight lines corresponding to these coefficients intersect at the point $\varepsilon^* = -0.24$, which

characterizes the position of the core–halo boundary in ε space. The ratio of the slopes of these linear relations is $b_1/b_2 \simeq 2.19$, implying that, during the time from $1.2\tau_{vr}$ to $1.6\tau_{vr}$, the rate of decrease of $\ln F(\varepsilon)$ with increasing ε is a factor of 2.19 higher in the cluster core than in the halo. The formation of such an $F(\varepsilon)$ phase-space density distribution is the result of violent relaxation in our cluster model.

The average deviations of $\ln F(\varepsilon)$ from the above linear relations correspond to fractional variations of $\frac{|\Delta F(\varepsilon)|}{F(\varepsilon)} \simeq 0.48$ and $\frac{|\Delta F(\varepsilon)|}{F(\varepsilon)} \simeq 0.85$ in the halo and core, respectively, which exceed the fractional errors for computing $F(\varepsilon)$ by factors of 8 and 14 in the halo and core, respectively (the fractional errors for computing the integrals (7) and (8) do not exceed 0.03). Figure 3 indicates that $\ln F(\varepsilon)$ deviates most from the linear relations in the core of the cluster model. Near the values $\varepsilon \simeq -0.32$ and -0.33, these deviations correspond to $\frac{|\Delta F(\varepsilon)|}{F(\varepsilon)} \sim 1$. A third linear relation $\ln F(\varepsilon) = a_3 + b_3\varepsilon$, where $b_3/b_1 \simeq 1.25$–1.30, is probably required to describe $\ln F(\varepsilon)$ in the interval $\varepsilon \in [-0.36, -0.28]$. The deviations of $\ln F(\varepsilon)$ from the linear relations $\ln F(\varepsilon) = a_{1,2} + b_{1,2}\varepsilon$ may well be the result of violent relaxation in the cluster model.

The strong irregularity of the shapes of the integration domains in (7) and (8) complicates the computation of $g(v)$ using (8). Applying the technique used to construct the integration domains for (7) and (8) twice enables us to reconstruct the form of $g(v)$ using the data on $F(\varepsilon)$ only approximately (Fig. 4). The dotted curve in Fig. 4 shows the function $g(v)$ derived from the stellar velocities for cluster model 2. The solid curve shows the distribution $g_1(v)$ of the absolute values v of the stellar velocities in this cluster model constructed by applying (8) to the data for $F(\varepsilon)$ using the above technique to construct the boundaries of the integration domain. The irregular shape of the integration-domain boundaries in (7) and (8) leads to the irregular shape of the $g_1(v)$ distribution and the presence of several peaks in this distribution. The smaller number of stars with absolute velocities v exceeding their mean value $\langle v \rangle$ in the $g_1(v)$ distribution compared to $g(v)$ is due mostly to two factors. The first is our neglect of stars with clustercentric distances $r > \overline{r}(\varepsilon) + (2.0$–$2.5)\sigma_{\overline{r}(\varepsilon)}$ when constructing the integration-domain boundaries in (7) and (8), and the second is the finite cell sizes used to determine the surfaces bounding the integration domains (here, $\overline{r}(\varepsilon)$ and $\sigma^2_{\overline{r}(\varepsilon)}$ are the mean clustercentric distance and dispersion of the deviations of r from $\overline{r}(\varepsilon)$ for stars with energies $\varepsilon' \in [\varepsilon, \varepsilon + \Delta\varepsilon]$, respectively).

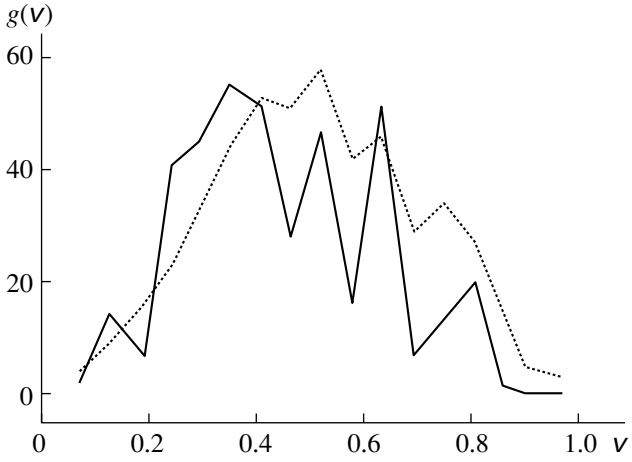

Fig. 4. Relations $g = g(v)$ and $g_1 = g_1(v)$ for time $t = 1.4\tau_{vr}$ in cluster model 2 of Paper 1. g and v are in numbers of stars (within the corresponding Δv intervals) and pc/Myr, respectively.

5. CONCLUSIONS

(1) As a result of the relaxation transition toward the equilibrium state considered in the current paper, the cluster models of Paper 1 establish a balance of transitions of stars between phase-space domains occupied by stars with energies ε from various intervals $[\varepsilon, \varepsilon + \Delta\varepsilon]$ on the ε axis over a time t_r. The number of stars entering the phase-space domain occupied by stars with energies close to ε is approximately equal to the number of stars leaving this domain.

(2) We have derived formulas for the differential ($\gamma(\varepsilon)$) and integrated ($\Gamma(\varepsilon)$) distributions of the energy ε of the phase-space volume occupied in the cluster by stars with energies $\varepsilon' \in [\varepsilon, \varepsilon + \Delta\varepsilon]$ and $\varepsilon' \leq \varepsilon$, respectively. The $\Gamma(\varepsilon)$ distribution in the cluster models of Paper 1 over a time t_r is a monotonically increasing function of ε. The quantity $\gamma(\varepsilon)$, which corresponds to the distribution $\Gamma(\varepsilon)$, mainly increases with ε.

(3) We have derived a formula for the phase-space stellar number density in open-cluster models that have attained the equilibrium state considered here. We have constructed the corresponding phase-space density distribution $F(\varepsilon)$ in phase-space volume intervals $\Delta\Gamma(\varepsilon)$, which is primarily a monotonically decreasing function of ε and can be fitted by a function of the form

$$F(\varepsilon) = \begin{cases} \exp(a_1 + b_1\varepsilon) & \text{at} \quad \varepsilon \leq \varepsilon^* \\ \exp(a_2 + b_2\varepsilon) & \text{at} \quad \varepsilon > \varepsilon^*, \end{cases}$$

where $a_i = \text{const}$, $b_i = \text{const}$ $(i = 1, 2)$, and ε^* determines the position of the core–halo boundary in ε space. Theoretically, the distribution $F(\varepsilon)$ combined

with (5) provides a full statistical description of a model cluster that has attained the equilibrium state in $(\varepsilon, \varepsilon_\zeta, l)$ space but is far from virial equilibrium and a steady state in the regular field.

(4) We have developed a technique for constructing the boundaries of the integration domains in (7) and (8) using the phase-space coordinates of stars in numerical models of open stellar clusters.

(5) The equilibrium phase-space density distribution $F(\varepsilon)$ obtained using the technique for construction of the integration-domain boundaries makes it possible to derive the distribution $g(v)$ of the stellar velocities v, which is in approximate agreement with the $g(v)$ distribution obtained from the stellar velocities for the model cluster.

ACKNOWLEDGMENTS

This work was supported by the Russian Foundation for Basic Research (project no. 00-02-16217) and the Ministry of Industry and Science of the Russian Federation (State Science and Technology Program Research and development in priority fields of science and technology, program "Astronomy").

REFERENCES

1. V. M. Danilov, Astron. Zh. **77**, 345 (2000) [Astron. Rep. **44**, 298 (2000)].
2. L. D. Landau and E. M. Lifshitz, *Course of Theoretical Physics,* Vol. 5: *Statistical Physics* (Nauka, Moscow, 1964; Pergamon, Oxford, 1980).
3. A. I. Ansel'm, *Foundations of Statistical Physics and Thermodynamics* (Nauka, Moscow, 1973).
4. V. A. Vasil'ev, Yu. M. Romanovskiĭ, and V. G. Yakhno, *Autowave Processes* [in Russian] (Nauka, Moscow, 1987).
5. W. C. Saslaw, *Gravitational Physics of Stellar and Galactic Systems* (Cambridge Univ. Press, Cambridge, 1985; Mir, Moscow, 1989).
6. M. D. Weinberg, Astrophys. J. **410**, 543 (1993).
7. D. Lynden-Bell, Mon. Not. R. Astron. Soc. **136**, 101 (1967).
8. S. A. Kutuzov and L. P. Osipkov, Astron. Zh. **57**, 28 (1980) [Sov. Astron. **24**, 17 (1980)].
9. V. M. Danilov, Astron. Zh. **59**, 490 (1982) [Sov. Astron. **26**, 297 (1982)].
10. G. A. Korn and T. M. Korn, *Mathematical Handbook for Scientists and Engineers* (McGraw-Hill, New York, 1961; Nauka, Moscow, 1968).

Translated by A. Dambis

Astronomy Reports, Vol. 46, No. 6, 2002, pp. 451–459. Translated from Astronomicheskiĭ Zhurnal, Vol. 79, No. 6, 2002, pp. 501–509.

A Comparative Analysis of the Integrated Radio Luminosities of Normal and Millisecond Pulsars

A. D. Kuz'min

Pushchino Radio Astronomy Observatory, Astro Space Center of the Lebedev Physical Institute, Pushchino, Russia

Received August 8, 2001; in final form, December 27, 2001

Abstract—We present the results of a comparative statistical analysis of the integrated radio luminosities of millisecond and normal pulsars and their dependences on other parameters of the pulsars. The analysis is based on our own measurements of the flux densities, spectra, and integrated radio luminosities of the millisecond pulsars, as well as data from the literature used to determine the integrated radio luminosities for 545 pulsars, 50 of them millisecond pulsars. Despite large differences in their periods P, period derivatives $\dot{P}$, magnetic fields B, and ages τ, the integrated radio luminosities of the millisecond and normal pulsars and their dependences on other parameters are approximately the same. The integrated radio luminosity depends on the parameter B/P^2, which is proportional to the potential difference in the polar-cap gap; this may indicate that the radio energy of pulsars is determined by the energy of primary particles accelerated in the polar-cap gap. Secular decreases in the radio luminosities of both normal and millisecond pulsars were also detected. © *2002 MAIK "Nauka/Interperiodica"*.

1. INTRODUCTION

The aim of the present study is to establish the parameters of pulsars determining the energetics of their radio emission. To this end, we have undertaken a comparative analysis of the integrated radio luminosities of millisecond and normal pulsars[1].

The total radio energy of pulsars is determined by the integrated radio luminosity over the entire frequency range considered and the solid angle for the pulsar radio beam

$$L_{\rm int} = \Omega d^2 \int_{\nu_1}^{\nu_2} S(\nu) d\nu,$$

where Ω is the solid angle of the beam, d the distance to the pulsar, (ν_1, ν_2) the frequency range under consideration, and $S(\nu)$ the flux density of the radio emission.

Millisecond and normal pulsars differ strongly in most parameters (their periods, period derivatives, magnetic fields, ages, and evolutionary histories). A comparative analysis of the integrated luminosities of millisecond and normal pulsars can be used to study dependences of the integrated luminosities over a broad range of variations of these parameters and to better distinguish the main factors determining the radio luminosity.

Most studies of pulsars and pulsar catalogs use monochromatic radio luminosities

$$Ł_\nu = S_\nu \times d^2,$$

where S_ν is the radio flux density at frequency ν (in mJy) and d is the distance to the pulsar (in kpc). The quantity L_ν characterizes the radio flux density at frequency ν reduced to the standard distance of $d = 1$ kpc.

The most complete data on the monochromatic radio luminosities of pulsars are those of Taylor *et al.* [1], who present data for 640 pulsars at 400 MHz. In their comparison of the monochromatic radio luminosities of millisecond and normal pulsars at 1.4 GHz, Kramer *et al.* [2] noted that the monochromatic luminosities of the millisecond pulsars were approximately an order of magnitude lower than those of the normal pulsars. Kuzmin and Losovskiĭ [3] found a somewhat smaller difference (about half an order of magnitude) for the monochromatic luminosities at the low frequencies of 102 and 111 MHz. Earlier [4], these same authors discovered a dependence of the monochromatic luminosities of millisecond pulsars on their rate of rotational energy loss $\dot{E}$. In his analysis of the monochromatic radio luminosities of 150 pulsars from the first catalog of Manchester and Taylor [6], Stollman [5] found a dependence of the luminosity on the parameter B/P^2,

[1] We consider millisecond pulsars to be those with short periods $P < 100$ ms and small period derivatives $\dot{P} < 10^{-17}$ s/s, which corresponds to the region in the $P - \dot{P}$ diagram with weak magnetic fields $B < 10^{10}$ G.

1063-7729/02/4606-0451$22.00

where B is the magnetic-field strength and P is the pulsar period.

However, all these analyses were carried out for monochromatic radio luminosities, which do not determine the radio energy of the pulsars. The monochromatic luminosity is convenient for rough comparisons of the radio intensities of pulsars, but does not characterize their total radio energy. There have been very few determinations and analyses of integrated radio luminosities of pulsars. Malov *et al.* [7] computed the radio luminosities of 232 pulsars. Based on analyses of dependences on other parameters, they reported that there was no luminosity decrease with age on time scales up to several million years, and that the integrated radio luminosity grows with the rate of rotational energy loss as $L \propto \dot{E}^{0.35}$ and decreases with increasing period as $\log L = 28.2(\pm 0.1) - 0.94(\pm 0.16) \log P$. If the period is indeed a determining factor, the radio luminosities of millisecond pulsars should be much higher (by approximately two orders of magnitude) than those of normal pulsars.

In the present study, we have determined the integrated radio luminosities for 545 pulsars, including 50 millisecond pulsars, performed a comparative analysis, and identified the main parameter determining the integrated radio luminosities of pulsars.

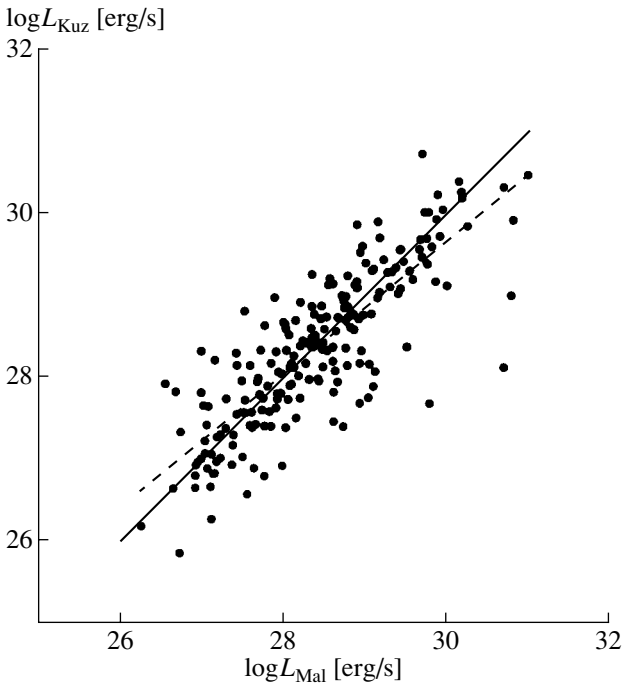

Fig. 1. Comparison of our integrated radio luminosities $L_{\rm Kuz}$ with the $L_{\rm Mal}$ computed values of Malov *et al.* [7] for 202 normal pulsars. The solid line corresponds to the relation $L_{\rm Kuz} = L_{\rm Mal}$, and the dashed line, to the correlation relation $L_{\rm Kuz} \propto (L_{\rm Mal})^{0.84}$.

2. DETERMINATION OF THE INTEGRATED RADIO LUMINOSITY

The integrated radio luminosity can be written

$$L_{\rm int} - \Omega d^2 \int_{\nu_1}^{\nu_2} S_{\rm m}(\nu) d\nu,$$

where, as before, Ω is the solid angle for the pulsar's radio beam, d the distance to the pulsar, and (ν_1, ν_2) the frequency range considered; $S_{\rm m} = SP/W$ is the flux density at the pulse maximum, P the pulsar's period, S the flux density averaged over the pulsar period, and W the mean profile width.

For millisecond pulsars, the effective widths of the mean pulse profile are approximately the same over the entire observed radio frequency range [8], and their radio spectra are power-law, without any low-frequency turnovers or high-frequency breaks [4, 9]. We adopted analogous simplifications, assuming constant widths for the mean profile and power-law spectra without low-frequency turnovers or high-frequency breaks, $S(\nu) = S_0(\nu/\nu_0)^{\alpha}$, to compute the luminosities of all pulsars, taking the width W to be equal to W_{50} at 400 MHz. In this case,

$$L_{\rm int} = \Omega d^2 S_{\rm m}(\nu_2^{\alpha+1} - \nu_1^{\alpha+1})/\nu_0^{\alpha}(\alpha+1).$$

We specified the lower frequency to be the well-studied frequency $\nu_1 = 100$ MHz. To simplify the calculations and increase the number of pulsars that could be used, we adopted the mean spectral index $\alpha = -1.7$ for all the normal pulsars. In this case, $\alpha + 1 < 0$ and $\nu_2^{\alpha+1} \ll \nu_1^{\alpha+1}$. The flux density S_0 was determined using the data of the catalog of Taylor *et al.* [1] recalculated to the reference frequency $\nu_0 = \nu_1 = 100$ MHz. The mean profile widths W_{50} and distances to the pulsars d were also taken from [1]. For an axially symmetrical beam,

$$\Omega = 2\pi(1 - \cos\varrho),$$

where ϱ is the cone opening angle of the pulsar emission. We took the ϱ values for 120 pulsars from [10]. For the remaining pulsars, we determined ϱ using the theoretical–empirical dependence for the opening angle on the period, $\varrho \approx 5^0 \times P^{-0.4}$, obtained from [10–13]. Then,

$$L_{\rm int} - 2\pi(1 - \cos\varrho) d^2 S_{\rm m} \nu_0 / |(\alpha+1)|.$$

Table 1 presents the resulting calculated values of $L_{\rm int}$ for the normal pulsars.

To verify the acceptability of the adopted simplifying assumptions and the trustworthiness of the resulting data, we compared our calculated integrated radio luminosities $L_{\rm Kuz}$ for 202 normal pulsars of the 495 we studied with the corresponding computed

values of Malov *et al.* [7], $L_{\rm Mal}$, which were obtained without these assumptions. The results of this comparison, shown in Fig. 1, shows that the two sets of values are in good agreement. The mean values $\log L_{\rm Kuz} = 28.5$ and $\log_{\rm Mal} = 28.4$ are virtually identical. The dependence $L_{\rm Kuz} \propto (L_{\rm Mal})^{0.84}$ shows a strong correlation between the two values. This confirms the admissibility of our adopted simplifications and the trustworthiness of our calculation results.

The basis for Table 2, which contains our integrated radio luminosities for the millisecond pulsars, was the flux-density and spectral-index measurements for 30 pulsars of Kuz'min and Losovskiĭ [3]. The radiation-cone opening angles ϱ for 15 pulsars were taken from [2]. We adopted $\varrho \approx 3.5^0 \times P^{-0.3}$ for the remaining millisecond pulsars, based on the approximate dependence of the opening angle on the pulsar period for the data of [2] and the lower boundary for $W_{50}(P)$. For the remaining millisecond pulsars, we calculated $L_{\rm int}$ using the method described above for the normal pulsars. The parameters for pulsars PSR J0030+0451, J0621+1002, J1744−1134, J1911−1114, J2051−0827, and J2129−5721, which are not included in the catalog of Taylor *et al.* [1], were taken from [3, 14–20]. The distance to J1744−1134, $d = 0.36$ kpc, was taken from the measurements of its parallax [21].

3. ANALYSIS AND DISCUSSION

Our comparison of the integrated radio luminosities of the millisecond and normal pulsars (Fig. 2) shows that, in spite of the large differences in their periods, period derivatives, surface magnetic fields, and ages, the integrated radio luminosities of the two groups of pulsars are approximately the same. The two mean values are 28.0 and 28.4, respectively. This indicates that the parameters listed above are not the most important in determining the radio energy of pulsars. We must search for another parameter whose value is, on average, roughly the same for normal and millisecond pulsars, and whose variations are correlated with variations in the luminosity. One such parameter is the quantity B/P^2, where $B = 3.2 \times 10^{19}(P\dot{P})^{1/2}$ is the magnetic field at the surface of the neutron star. The mean values of this parameter, like the radio luminosities, are approximately the same for normal and millisecond pulsars.

The dependence $L_{\rm int}(B/P^2)$ is shown in Fig. 3. To better represent the character of this dependence, we have grouped the integrated radio luminosities and averaged them in equal intervals of $\log B/P^2$. The circles (for normal pulsars) and triangles (for millisecond pulsars) show the averaged integrated radio luminosities $\langle \log L_{\rm int} \rangle$ and the rms errors for these mean values. The solid and dashed lines show linear-regression approximations to these relations.

The $L_{\rm int}(B/P^2)$ dependence is different for small and large values of B/P^2 and can be described with the piecewise power-law function

$$L_{\rm int} \propto \begin{cases} (B/P^2)^{0.8\pm0.1} & \text{for} \quad \log(B/P^2) \le 13 \\ (B/P^2)^{0.1\pm0.1} & \text{for} \quad \log(B/P^2) \ge 13 \end{cases}$$

for the normal pulsars. For the millisecond pulsars, the dependence

$$L_{\rm int} \propto (B/P^2)^{1.2\pm0.3}$$

in the interval $11 < \log B/P^2 < 14$ is similar to the relation presented above for the normal pulsars in this interval.

Our relations for the dependence of the integrated radio luminosity $L_{\rm int}$ on B/P^2 formally coincide with the analogous dependence for the monochromatic radio luminosity obtained by Stollman [5], $L_{400}(B/P^2)$. However, qualitatively, analyzing the integrated radio luminosities enables us to take a further step in understanding the physical processes associated with the pulsar radio emission.

The integrated radio luminosity $L_{\rm int}$ represents the radio energy of the pulsar, while the parameter B/P^2 is proportional to the potential difference in the polar-cap gap, ($\Phi_{\rm max} \propto B/P^2$) [22]. The relationship we have identified between the integrated radio luminosity and B/P^2 can be understood in a physical model in which the pulsar's radio energy is determined by the accelerating potential in the polar-cap gap. This may indicate that the radio energy of pulsars $E_{\rm radio}$ is determined by the energy of primary particles $E_{\rm part}$ accelerated in the polar-cap gap: $E_{\rm radio} \propto E_{\rm part}^{0.8}$.

We have also found a secular decrease in the integrated radio luminosity with increasing pulsar age $\tau = P/2\dot{P}$ for both the millisecond and normal pulsars. The $L_{\rm int}(\tau)$ dependence is shown in Fig. 4. The circles (for normal pulsars) and triangles (for millisecond pulsars) show the luminosities $\langle \log L_{\rm int} \rangle$ averaged over equal intervals of τ and the corresponding rms errors. The solid and dashed lines show linear-regression approximations to these relations. However, the millisecond and normal pulsars do not form a single age sequence, displaying instead two separate branches, in each of which the radio luminosity decreases with increasing pulsar age.

For the normal pulsars, the character of the $L_{\rm int}(\tau)$ dependence is also different for small and large values of τ, and can be represented by the piecewise power-law function

$$L_{\rm int} \propto \begin{cases} \tau^{-0.1\pm0.1} & \text{for} \quad \tau \le 10^6 \quad \text{yr} \\ \tau^{-0.5\pm0.1} & \text{for} \quad \tau \ge 10^6 \quad \text{yr.} \end{cases}$$

Table 1. Integrated radio luminosities of the normal pulsars

PSR	$\log L$ [erg/s]	PSR	$\log L$ [erg/s]	PSR	$\log L$ [erg/s]	PSR	$\log L$ [erg/s]
J0006+1834	25.7	B0540+23	29.2	B0909−71	28.4	J1123−6256	29.4
B0011+47	27.3	B0559−57	27.0	B0917+63	26.5	J1124−6652	28.5
B0031−07	27.3	B0609+37	28.3	B0922−52	28.9	B1124−60	29.3
B0037+56	28.6	B0611+22	29.4	B0923−58	27.8	J1130−6815	28.8
J0045−7319	29.1	B0621−04	28.0	B0932−52	28.3	B1133+16	27.4
B0052+51	27.0	B0626+24	29.4	J0941−5248	28.7	B1133−55	28.5
B0053+47	26.9	B0628−28	28.7	B0940−55	29.6	J1140−3107	28.0
B0059+65	27.3	B0643+80	28.2	B0941−56	29.2	B1143−60	28.4
B0105+65	27.6	B0656+14	26.8	B0940+16	27.0	J1156−5909	29.3
B0114+58	28.3	B0655+64	26.7	B0942−13	27.8	B1154−62	30.3
J0132−7010	27.8	J0725−1637	28.4	B0943+10	26.6	B1159−58	29.1
B0136+57	29.2	B0727−18	28.3	B0950+08	27.2	J1209−5556	30.1
B0138+59	28.4	B0740−28	29.6	B0953−52	29.3	B1221−63	29.1
B0144+59	27.9	J0749−4247	27.7	B0957−47	27.7	J1225−5600	28.3
B0149−16	27.2	B0756−15	28.7	B0959−54	29.4	B1222−63	30.1
B0154+61	27.3	B0809+74	26.9	B1001−47	28.3	B1232−55	27.7
B0203−40	27.5	B0818−13	29.1	J1007−6316	28.7	B1237+25	27.5
B0226+70	27.1	B0818−41	27.9	B1010−23	27.1	B1236−68	28.0
B0254−53	27.9	B0820+02	27.9	B1011−58	29.4	B1237−41	28.1
B0301+19	27.0	B0823+26	28.0	B1014−53	27.7	B1240−64	30.7
B0320+39	27.9	B0826−34	25.4	B1015−56	29.5	J1253−5819	28.8
B0329+54	30.3	B0833−45	30.2	B1030−58	28.6	B1256−67	27.9
B0331+45	28.1	B0834+06	27.7	J1036−4926	29.1	B1259−63	28.4
B0339+53	27.3	B0835−41	30.1	B1036−58	27.8	B1309−55	29.0
B0353+52	28.7	B0839−53	29.2	B1039−55	28.9	B1316−60	29.7
B0355+54	29.1	B0840−48	29.0	B1044−57	28.8	B1317−53	29.0
B0403−76	27.9	B0844−35	27.6	J1047−6711	28.6	B1322+83	27.0
B0402+61	28.5	B0853−33	27.3	B1046−58	28.8	J1321−3509	27.1
B0410+69	28.0	B0855−61	28.9	B1054−62	30.2	B1323−58	30.6
J0448−2757	27.2	J0858−4419	29.0	B1055−52	28.8	B1323−63	29.9
B0450+55	28.1	B0901−63	28.2	B1056−78	28.1	B1322−66	29.0
J0459−0210	27.0	B0903−42	28.3	B1056−57	28.5	B1323−62	30.2
B0458+46	27.8	J0904−4546	28.6	B1105−59	27.9	B1323−627	29.4
B0525+21	27.9	B0904−74	28.5	B1107−56	29.3	B1325−43	28.4
B0529−66	30.3	J0905−5127	29.4	B1112+50	26.7	J1332−3033	26.8
B0531+21	30.2	B0905−51	28.6	B1114−41	28.7	J1334−5839	29.0
B0538−75	27.6	B0906−17	27.3	B1118−79	27.2	B1334−61	28.3
B0540−69	29.3	B0906−49	29.8	B1119−54	30.1	B1336−64	27.9

Table 1. (Contd.)

PSR	$\log L$ [erg/s]	PSR	$\log L$ [erg/s]	PSR	$\log L$ [erg/s]	PSR	$\log L$ [erg/s]
B1338−62	29.5	B1557−50	30.5	B1657−13	28.7	B1736−31	28.0
B1352−51	29.1	B1556−57	29.0	J1700−3310	28.7	B1737+13	28.9
J1356−5521	29.2	B1558−50	29.5	B1657−45	29.5	B1737−30	28.3
B1353−62	29.5	J1603−2531	29.0	B1700−18	28.1	B1738−08	28.3
B1356−60	30.2	B1600−27	28.3	B1700−32	28.5	B1737−39	29.3
B1358−63	28.8	B1600−49	29.5	J1703−4900	28.8	B1740−03	27.7
B1359−51	27.8	B1601−52	27.4	B1659−60	27.4	B1740−13	28.4
B1409−62	28.5	B1604−00	27.6	B1702−19	28.2	B1740−31	27.9
B1417−54	28.5	B1607−52	28.5	J1705−3422	28.7	J1744−2334	28.1
B1424−55	28.6	B1609−47	28.7	B1703−40	28.0	B1742−30	29.0
B1426−66	28.9	B1612+07	28.0	B1701−75	27.2	B1745−12	28.8
B1436−63	28.9	B1610−50	29.3	B1706−16	28.3	B1746−30	28.7
B1449−64	29.7	B1612−29	27.2	J1709−3421	28.7	B1745−56	27.6
B1451−68	28.4	J1615−3936	29.2	B1706−44	28.2	B1747−31	28.7
B1454−51	27.3	B1611−55	28.6	B1709−15	28.1	J1750−3506	28.5
B1503−51	27.5	J1622−4334	28.9	B1707−53	28.6	B1747−46	28.1
B1504−43	28.2	J1625−4050	28.9	B1714−34	29.6	B1749−28	29.9
B1503−66	29.0	B1626−47	28.9	B1713−40	28.8	B1750−24	28.9
B1508+55	29.0	B1630−44	29.3	B1715−40	28.8	B1754−24	28.3
B1507−44	28.2	B1629−50	29.9	B1718−02	28.5	B1756−22	29.1
B1508−57	29.9	B1633+24	28.0	B1717−16	27.9	J1759−2922	28.2
B1509−58	27.7	B1630−59	28.9	B1717−29	27.8	B1758−03	29.4
B1510−48	27.7	B1634−45	28.0	B1718−19	28.1	B1758−23	29.6
B1518−58	28.8	B1635−45	28.6	B1718−35	29.6	B1758−29	28.3
B1524−39	27.6	B1636−47	28.9	B1718−32	29.0	B1800−21	28.6
B1523−55	29.1	B1641−45	30.6	B1718−36	28.2	B1800−27	27.8
B1530+27	27.3	B1642−03	30.4	B1719−37	29.0	B1804−08	29.8
B1530−53	28.2	B1643−43	29.0	B1726−00	28.0	B1804−27	29.8
B1530−539	28.7	B1641−68	27.5	B1727−33	29.0	J1808−0813	28.9
B1535−56	28.5	J1648−3256	28.8	B1727−47	29.8	B1805−20	29.0
J1542−5034	28.9	J1650−1654	28.0	B1729−41	28.7	B1806−53	28.3
B1540−06	28.3	B1648−17	27.4	B1730−22	28.2	B1810+02	28.5
B1541−52	28.1	B1648−42	29.2	B1730−37	27.4	B1813−17	28.6
J1549−4848	28.2	B1647−52	29.3	B1732−02	28.7	B1813−26	28.1
B1550−54	28.2	B1647−528	28.7	B1732−07	29.1	B1813−36	29.0
J1556−4258	29.9	B1649−23	28.0	B1734−35	28.0	B1815−14	28.2
B1556−44	29.1	B1650−38	28.7	B1735−32	27.0	B1818−04	29.2
B1555−55	28.9	J1654−2707	28.2	B1736−29	29.0	B1817−13	27.8

Table 1. (Contd.)

PSR	$\log L$ [erg/s]	PSR	$\log L$ [erg/s]	PSR	$\log L$ [erg/s]	PSR	$\log L$ [erg/s]
B1817−18	28.8	B1844−04	28.9	B1907+00	28.8	B1924+16	29.0
B1820−14	28.6	J1848+0826	27.7	B1907+02	28.9	B1924+19	29.0
B1819−22	28.2	B1845−01	29.1	B1907+10	29.6	B1925+18	28.4
J1822−4210	28.1	J1848−1414	28.7	J1909+1450	27.4	B1925+1882	27.7
B1821+05	28.9	B1845−19	27.0	J1909+1859	28.2	B1925+22	28.7
J1823−0154	28.8	B1846−06	28.8	B1907+03	28.2	B1926+18	28.1
B1820−11	28.6	B1848+13	28.3	J1910+0714	27.8	B1927+13	28.8
B1820−30B	28.8	B1848+04	27.9	B1907+12	28.4	B1929+15	27.9
B1820−31	28.6	B1848+12	28.6	B1907−03	29.8	B1929+10	27.8
B1821−11	29.3	B1849+00	28.8	J1911+1758	27.6	B1929+20	29.5
B1821−19	29.3	J1852−2610	28.3	B1910+10	27.6	B1930+22	29.5
B1822+00	28.1	B1851−14	28.6	B1910+20	28.8	B1930+13	28.0
B1822−09	28.7	B1853+01	27.8	J1912+2525	27.4	B1931+24	28.3
B1822−14	28.0	B1855+02	29.5	B1911+09	27.6	B1933+16	30.9
B1823−11	27.7	J1859+1526	28.0	B1911+13	28.8	B1933+17	28.4
B1823−13	27.8	B1857−26	28.7	B1911−04	29.6	B1933+15	28.4
B1824−10	27.9	B1859+01	28.7	B1911+11	27.7	B1935+25	27.9
B1826−17	29.1	B1859+03	29.6	J1915+0738	27.4	J1941+1026	28.6
B1829−08	28.4	B1859+07	28.4	B1913+10	28.7	B1939+17	29.1
B1831−03	29.4	J1901+1306	26.9	B1913+16	28.6	B1940−12	28.0
B1830−08	29.0	J1901−0907	28.2	B1913+167	27.6	B1943+18	28.7
B1828−60	27.1	B1900+05	28.3	B1914+09	29.0	B1942−00	27.6
B1831−00	27.6	B1900+06	29.0	B1914+13	28.6	B1944+17	28.0
B1831−04	29.0	J1902+0723	26.8	B1915+13	29.6	B1944+22	28.4
B1832−06	28.1	B1900+01	29.0	B1916+14	29.6	B1946+35	30.4
J1835−1106	29.0	J1903+2225	28.2	J1918+1541	26.2	B1946−25	27.5
B1834−04	28.8	B1900−06	29.5	B1917+00	28.9	J1951+1123	27.0
B1834−10	28.7	J1904+0004	29.5	B1918+26	27.5	B1951+32	28.2
J1837−0048	28.1	B1901+10	27.4	B1919+14	28.0	B1952+29	27.0
B1834−06	28.1	J1904−1224	28.7	B1918+19	29.4	B1953+50	28.6
B1839+56	27.9	B1903+07	28.4	B1919+20	27.1	J2002+1637	27.7
B1839+09	28.6	B1902−01	29.0	B1919+21	27.5	B2000+32	28.7
B1839−04	27.7	J1906+1854	28.5	B1920+20	28.4	B2000+40	29.7
B1842+14	28.4	B1904+12	28.1	B1920+21	30.2	B2002+31	29.4
B1842−02	28.1	B1905+39	27.7	B1921+17	28.0	J2005−0016	27.6
B1841−04	27.8	J1908+0500	28.6	B1922+20	28.9	B2003−08	28.4
B1841−05	28.5	J1908+0734	26.8	B1923+04	29.0	J2008+2513	27.9
B1842−04	27.8	B1906+09	28.0	B1924+14	29.2	B2011+38	29.7

Table 1. (Contd.)

PSR	$\log L$ [erg/s]	PSR	$\log L$ [erg/s]	PSR	$\log L$ [erg/s]	PSR	$\log L$ [erg/s]
J2015+2524	25.2	B2045+56	29.4	B2152−31	27.3	B2306+55	28.1
B2016+28	29.1	B2045−16	27.5	B2151−56	26.1	B2310+42	28.6
B2020+28	28.4	B2048−72	27.5	B2154+40	29.6	B2315+21	27.8
B2021+51	28.6	B2053+21	27.9	J2215+1538	28.1	B2323+63	28.2
B2022+50	28.1	B2053+36	29.5	B2217+47	29.4	B2324+60	28.8
B2025+21	28.91	B2106+44	28.9	B2224+65	28.4	B2327−20	27.4
B2027+37	29.1	B2110+27	28.1	B2227+61	28.8	B2334+61	28.1
B2028+22	28.4	B2111+46	30.0	B2241+69	27.3	B2351+61	28.8
B2035+36	28.6	J2144−3939	25.9	B2255+58	29.4		
B2044+15	28.4	B2148+52	29.1	J2307+2225	25.9		

Table 2. Integrated radio luminosities of the millisecond pulsars

PSR	$\log L$ [erg/s]	PSR	$\log L$ [erg/s]	PSR	$\log L$ [erg/s]	PSR	$\log L$ [erg/s]
B0021−72C	27.9	J1045−4509	28.6	B1821−24	30.1	B2127+11A	28.7
B0021−72D	27.8	B1257+12	27.4	B1855+09	28.1	B2127+11B	28.2
J0030+0451	26.5	B1310+18	29.0	J1911−1114	28.2	B2127+11E	27.7
J0034−0534	27.3	J1518+4904	26.9	B1913+16	28.3	B2127+11F	27.4
J0218+4232	28.9	B1534+12	27.4	B1937+21	30.6	B2127+11C	29.3
J0437−4715	27.4	B1620−26	28.5	B1953+29	29.1	J2129−572	27.9
J0613−0200	28.3	B1639+36A	28.6	B1957+20	29.2	J2145−0750	27.6
J0621+1002	27.4	J1640+2224	28.9	J2019+2425	27.9	J2229+2643	27.0
J0711−6830	26.5	J1713+0747	29.1	J2033+1736	26.5	J2235+1506	27.2
J0751+1807	27.5	J1730−2304	27.4	J2051−0827	28.5	J2317+1439	28.7
J1012+5307	27.5	J1744−1134	26.9	B2127+11D	28.7	J2322+2057	27.4
J1022+10	27.6	J1804−2718	27.7	B2127+11G	26.8		
J1025−0709	26.3	J1820−30A	30.2	B2127+11H	27.8		

For the millisecond pulsars,

$$L_{\rm int} \propto \tau^{-0.5\pm0.1}.$$

The secular decrease in the integrated radio luminosity is a consequence of the $L_{\rm int}(B/P^2)$ dependence. During a secular increase in the period and decay of the magnetic field, the accelerating potential in the polar-cap gap decreases, ($\Phi_{\rm max} \propto B/P^2$) so that, due to the $L_{\rm int}(B/P^2)$ dependence, the integrated radio luminosity $L_{\rm int}$ also decreases. This relationship is supported by the fact that the $L_{\rm int}(\tau)$ dependence also has a break, with the break point $\tau \approx 10^6$ yr agreeing with the break point $\log B/P^2 \approx 13$ for the $L_{\rm int}(B/P^2)$ dependence, in accordance with the empirical relation $\log(B/P^2) \approx 16.7 - 0.63 \log \tau$.

The dependence of the integrated radio luminosity on the period [7] in the presence of nearly equal integrated radio luminosities for millisecond and normal

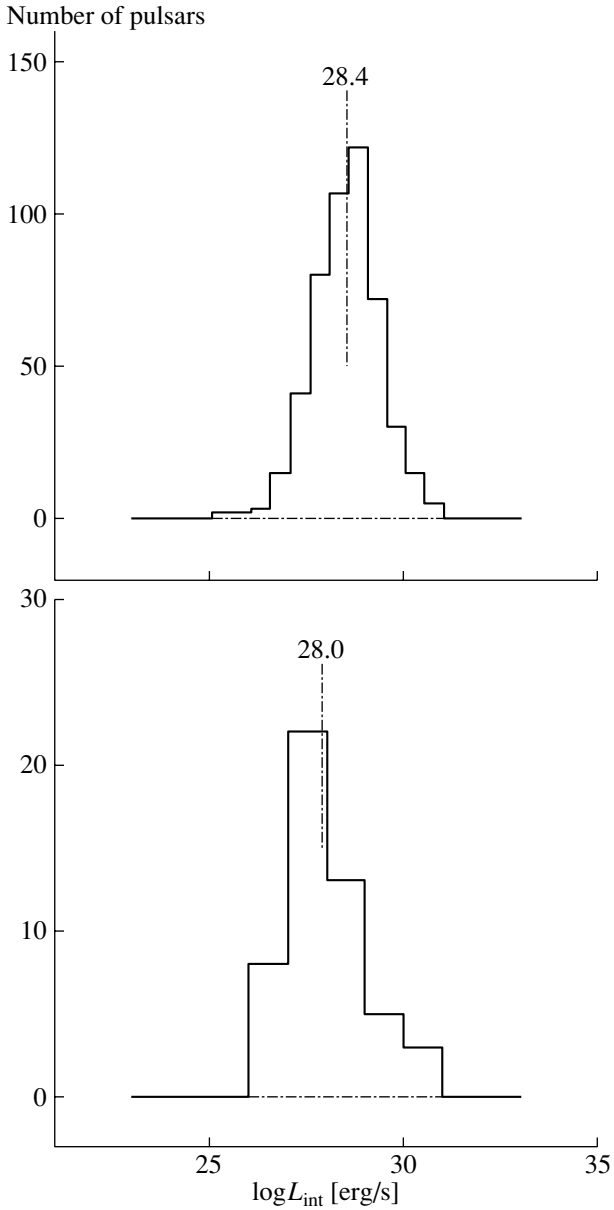

Fig. 2. Distributions of integrated radio luminosities for normal and millisecond pulsars.

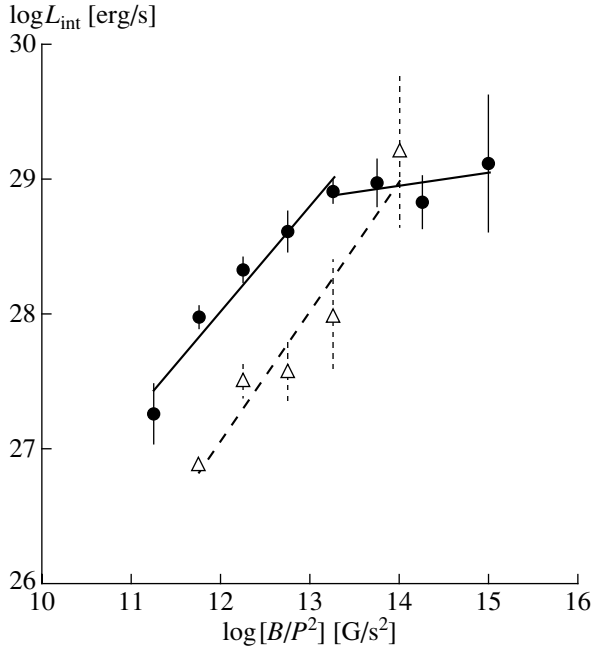

Fig. 3. $\log L_{\rm int} - (\log B/P^2)$ dependence. The circles (normal pulsars) and triangles (millisecond pulsars) show the integrated radio luminosities $\langle \log L \rangle$ averaged in equal intervals of $\log B/P^2$ and the corresponding rms errors. The solid and dashed lines show linear-regression approximations to these dependences.

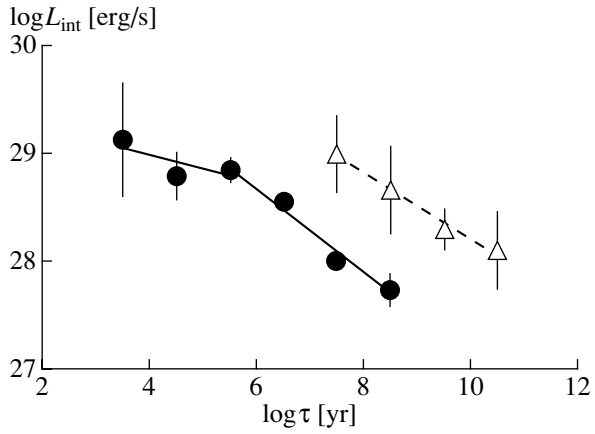

Fig. 4. Dependences of the integrated radio luminosities of normal and millisecond pulsars on their characteristic ages $\tau = P/2\dot{P}$. The circles (normal pulsars) and triangles (millisecond pulsars) show the luminosities $\langle \log L \rangle$ averaged over equal intervals of τ and the corresponding rms errors. The solid and dashed lines show linear-regression approximations to these dependences.

pulsars but large differences in their periods indicates that this is not the main parameter determining the radio energies of the pulsars.

The radio-luminosity variations are also correlated with the rate of loss of kinetic rotational energy:

$$Ł_{\rm int} \propto \dot{E}^{0.5}.$$

We did not detect any significant dependence of the integrated radio luminosity on the period derivative or magnetic field strength.

4. CONCLUSION

We have determined the integrated radio luminosities of 545 pulsars, 50 of them millisecond pulsars.

In spite of the large differences in their periods P, period derivatives $\dot{P}$, magnetic-field strengths B,

and ages τ, the integrated radio luminosities of the millisecond and normal pulsars were approximately the same.

The integrated radio luminosity depends on the parameter B/P^2, which is proportional to the potential difference in the polar-cap gap. The character of this dependence is different for small and large values of B/P^2 and can be represented by the piecewise power-law function

$$L_{\rm int} \propto \begin{cases} (B/P^2)^{0.8\pm0.1} \text{ for} \log(B/P^2) \le 13 \\ (B/P^2)^{0.1\pm0.1} \text{ for} \log(B/P^2) \ge 13. \end{cases}$$

The radio energy of pulsars $E_{\rm radio}$ is determined by the energy of primary particles being accelerated in the polar-cap gap, $E_{\rm part}$: $E_{\rm radio} \propto E_{\rm part}^{0.8}$.

We also detected a secular decrease in the integrated radio luminosities of the pulsars.

ACKNOWLEDGMENTS

The author would like to thank the referee for useful comments. This work was supported by the Russian Foundation for Basic Research project no. 01-02-16326.

REFERENCES

1. J. H. Taylor, R. N. Manchester, A. G. Lyne, *et al.*, Catalog of 706 pulsars, 1995 (unpublished work).
2. M. Kramer, K. M. Xilourism, D. R. Lorimer, *et al.*, Astrophys. J. **501**, 270 (1998).
3. A. D. Kuzmin and B. Ya. Losovsky, Astron. Astrophys. **368**, 230 (2001).
4. A. D. Kuz'min and B. Ya. Losovskiĭ, Pis'ma Astron. Zh. **26**, 581 (2000) [Astron. Lett. **26**, 500 (2000)].
5. G. M. Stollman, Astron. Astrophys. **171**, 152 (1987).
6. R. N. Manchester and J. H. Taylor, Astron. J. **86**, 1953 (1981).
7. I. F. Malov, V. M. Malofeev, and D. S. Sen'e, Astron. Zh. **71**, 762 (1994) [Astron. Rep. **38**, 677 (1994)].
8. A. D. Kuz'min and B. Ya. Losovskiĭ, Pis'ma Astron. Zh. **25**, 441 (1999) [Astron. Lett. **25**, 375 (1999)].
9. M. Kramer, Ch. Lange, D. Lorimer, *et al.*, Astrophys. J. **526**, 957 (1999).
10. J. M. Rankin, Astrophys. J., Suppl. Ser. **85**, 145 (1993).
11. A. D. Kuz'min and I. M. Dagkesamanskaya, Pis'ma Astron. Zh. **9**, 149 (1983) [Sov. Astron. Lett. **9**, 80 (1983)].
12. A. D. Kuz'min, I. M. Dagkesamanskaya, and V. D. Pugachev, Pis'ma Astron. Zh. **10**, 854 (1984) [Sov. Astron. Lett. **10**, 357 (1984)].
13. A. G. Lyne and R. N. Manchester, Mon. Not. R. Astron. Soc. **234**, 477 (1988).
14. A. Somer, Astron. Soc. Pac. Conf. Ser. **202**, 17 (2000).
15. F. Camilo, D. Nice, and J. H. Taylor, Astrophys. J. **461**, 812 (1996).
16. I. H. Stairs, S. E. Thorsett, and F. Camilo, Astrophys. J., Supp. Ser. **123**, 627 (1999).
17. D. R. Lorimer, A. G. Lyne, M. Bailes, *et al.*, Mon. Not. R. Astron. Soc. **23**, 1383 (1997).
18. R. S. Foster, B. J. Cadwell, A. Wolszczan, and S. B. Anderson, Astrophys. J. **454**, 826 (1995).
19. M. Bails, S. Johnston, J. F. Bell, *et al.*, Astrophys. J. **481**, 386 (1997).
20. I. Stappers, M. Bailes, A. G. Lyne, *et al.*, Astrophys. J. Lett. **465**, L119 (1996).
21. M. Toscano, M. S. Britton, R. N. Manchester, *et al.*, Astrophys. J. **523**, L171 (1999).
22. B. Zhang, A. K. Harding, and A. G. Muslimov, Astrophys. J. **531**, L135 (2000).

Translated by D. Gabuzda

Astronomy Reports, Vol. 46, No. 6, 2002, pp. 460–473. Translated from Astronomicheskiĭ Zhurnal, Vol. 79, No. 6, 2002, pp. 510–525.

Subsystems of RR Lyrae Variable Stars in Our Galaxy

T. V. Borkova and V. A. Marsakov

Rostov State University, Rostov-on-Don, 344104 Russia

Received March 1, 2001; in final form, November 23, 2001

Abstract—We have used published, high-accuracy, ground-based and satellite proper-motion measurements, a compilation of radial velocities, and photometric distances to compute the spatial velocities and Galactic orbital elements for 174 RR Lyrae (ab) variable stars in the solar neighborhood. The computed orbital elements and published heavy-element abundances are used to study relationships between the chemical, spatial, and kinematic characteristics of nearby RR Lyrae variables. We observe abrupt changes of the spatial and kinematic characteristics at the metallicity $[\mathrm{Fe/H}] \approx -0.95$ and also when the residual spatial velocities relative to the LSR cross the critical value $V_{\mathrm{res}} \approx 290$ km/s. This provides evidence that the general population of RR Lyrae stars is not uniform and includes at least three subsystems occupying different volumes in the Galaxy. Based on the agreement between typical parameters for corresponding subsystems of RR Lyrae stars and globular clusters, we conclude that metal-rich stars and globular clusters belong to a rapidly rotating and fairly flat, thick-disk subsystem with a large negative vertical metallicity gradient. Objects with larger metal deficiencies can, in turn, be subdivided into two populations, but using different criteria for stars and clusters. We suggest that field stars with velocities below the critical value and clusters with extremely blue horizontal branches form a spherical, slowly rotating subsystem of the protodisk halo, which has a common origin with the thick disk; this subsystem has small but nonzero radial and vertical metallicity gradients. The dimensions of this subsystem, estimated from the apogalactic radii of orbits of field stars, are approximately the same. Field stars displaying more rapid motion and clusters with redder horizontal branches constitute the spheroidal subsystem of the accreted outer halo, which is approximately a factor of three larger in size than the first two subsystems. It has no metallicity gradients; most of its stars have eccentric orbits, many display retrograde motion in the Galaxy, and their ages are comparatively low, supporting the hypothesis that the objects in this subsystem had an extragalactic origin.

1. INTRODUCTION

The complex, multicomponent structure of the Galactic halo is being confirmed by more and more studies. In particular, the halo contains the thick disk subsystem, with a relatively high abundance of heavy elements, and two low-metallicity components: the protodisk halo subsystem, which shares a common origin with the disk, and a subsystem that presumably was formed from extragalactic fragments captured by the Galaxy. The presence of two populations with different histories in the low-metallicity halo was suggested in [1], where it was shown that two components were needed to model the dynamics of RR Lyrae variables with metallicities $[\mathrm{Fe/H}] < -1.0$: a spherical and a somewhat flattened component, with the latter dominating at Galactocentric distances less than the radius of the solar circle. The idea that there are two populations in the metal-poor halo was primarily developed during studies of globular clusters. This is the only Galactic population that is observable without considerable selection effects as far away as the Galactic center, and even beyond it, making it possible to establish the spatial distributions of objects in the proposed subsystems with reasonable reliability. In addition, globular clusters possess a feature (the structure of their horizontal branches) that can be used to distinguish between metal-poor clusters of different subsystems. Halo clusters with redder horizontal branches for a given metallicity (i.e., with horizontal branches showing a considerable number of stars on the low-temperature side of the Schwarzschild gap) are predominantly outside the solar circle. In addition, they exhibit a larger velocity dispersion and a slower orbital motion (a significant number having retrograde orbits) and are, on average, younger than clusters with very blue horizontal branches, which are concentrated within the solar circle. The explanation suggested for these differences was that the subsystem of older clusters formed together with the Galaxy as a whole, whereas the clusters of the young halo subsystem formed from fragments captured by the Galaxy from intergalactic space at later stages of its evolution [2].

Metal-poor field stars show a similar multicomponent structure. In particular, a study of a large

1063-7729/02/4606-0460$22.00

sample of stars in a deep survey in the direction of the North Galactic Pole demonstrated that stars further than 5 kpc from the plane of the disk tend to have retrograde orbits [3]. (The retrograde orbits clearly testify that the objects' origin was independent of that of the Galaxy, which exhibits prograde rotation.) Further evidence for the presence of objects with an extragalactic origin among field stars is the identification of objects with relatively young ages and low abundances of heavy elements (so that they should have been older, according to abundance age indicators). The subsystem of accreted globular clusters was named the "young halo" for precisely this reason. On average, high-velocity field subdwarfs with highly eccentric orbits ($e > 0.85$) are younger than subdwarfs with similar metallicities but less eccentric orbits [4]. The isochrone ages of subdwarfs were derived in [4] based on Strömgren photometry. Hanson *et al.* [5], who also used abundances of α elements as age indicators, likewise concluded that metal-poor red giants in retrograde orbits were relatively young. ([α/Fe] is known to be low for young objects formed from matter already enriched in the ejecta of type Ia supernovae, whereas the higher relative abundances of α elements in older stars are due to type II supernovae.) Unfortunately, no age indicators for individual RR Lyrae stars are available. However, observations of field RR Lyrae stars and blue horizontal-branch stars were used in [6] to estimate the number ratios of these objects in different directions from the Sun. Blue horizontal-branch giants dominate among stars close to the Galactic center and Galactic plane, whereas the numbers of variable stars and giants were approximately the same at greater distances. These stars have similar metallicities, suggesting that the inner, bluer population of the Galaxy is older than the outer population.

The recent papers [7, 8] present detailed studies of the kinematics of RR Lyrae stars in the solar neighborhood. The stars were assumed to form only two subsystems: a thick disk and a halo. In the current study, we attempt to identify accreted halo stars among these RR Lyrae variables. We use the spatial velocities and computed elements of Galactic orbits as our main criteria for distinguishing the subsystems (taking into account the nearby location of the studied variables). We wish to investigate relationships between the physical, chemical, spatial, and kinematic characteristics of RR Lyrae variables in each of the subsystems, determine the characteristic parameters of the subsystems, and compare them with the parameters of similar subsystems of globular clusters.

2. SOURCE DATA

The input catalog for our study was [9], which presents metallicities for 302 RR Lyrae (ab) variables known up until 1985 and brighter than apparent magnitude 13.5. In [9], the abundances of heavy elements were derived from the ratio of the intensities of the Ca II K line and H_δ and H_β Balmer lines (an analog of the ΔS index of Preston) and reduced to the [Fe/H] scale of [10]. The typical uncertainty of an individual [Fe/H] value is 0.15–0.20 dex. We added several bright stars that are missing from [9], for which metallicities were computed in [11] from published ΔS values. Checks presented in [12] show that the metallicities of [9] are in very good agreement with [Fe/H] values derived from Fe II lines using high-resolution spectra with high signal-to-noise ratios. Having in mind the large relative errors of the trigonometric parallaxes for distant objects, we chose to use the photometric distance scale of [9] (assuming $M_V(\mathrm{RR}) = 0.15[\mathrm{Fe/H}] + 1.01$). The radial velocities were also taken from [9]. Our final list contains 317 stars.

We created another sample for an analysis of the three-dimensional motion of these stars as a function of metallicity, containing 124 stars in the solar neighborhood brighter than 12.5^m from [7], with proper motions taken from the Hipparcos catalog. This sample includes virtually all bright RR Lyrae variables known prior to 1976 (such data were included in the satellite's input catalog). We supplemented our list with stars from [8], which presents data for all nearby RR Lyrae stars of the northern sky brighter than 11^m known in 1997 (a total of 130). The proper motions in [8] are averages from seven sources with high-accuracy ground-based observations, as well as from the Hipparcos catalog. Fifty stars from [8] entered our sample.

For each star, we computed the spatial velocity components in cylindrical coordinates and orbital elements using the Galactic model of [13], which includes a spherical bulge, disk, and extended massive halo. The model assumes the Galactocentric distance of the Sun to be $R_\odot = 8.5$ kpc and the Galactic rotation rate at the solar distance to be $V_{\mathrm{rot}} = 220$ km/s. Table 1 presents the metallicities, Galactic azimuthal velocity components, full residual velocities relative to the local solar centroid [with $(U_\odot, V_\odot, W_\odot) = (-10, 10, 6)$ km/s], and Galactic orbital elements for 174 RR Lyrae variables in our final sample. The orbital elements were computed by modeling five complete orbits around the Galactic center for each star. The most informative quantities are $Z_{\max}$, the maximum distance of the orbit from the Galactic center (the orbital apogalactic radius), and the eccentricity, $e = (R_a - R_{\min})/(R_a + R_{\min})$, where $R_{\min}$ is the minimum distance of the orbit from the Galactic center. To adequately estimate the characteristic parameters of the proposed RR Lyrae subsystems, the sample must be representative of the objects in these

Table 1. Orbital elements for nearby RR Lyrae variables

Name	[Fe/H]	Θ, km/s	V_{res}, km/s	R_a, kpc	Z_{max}, kpc	e	Name	[Fe/H]	Θ, km/s	V_{res}, km/s	R_a, kpc	Z_{max}, kpc	e
SW And	−0.38	200	40	9.0	0.4	0.01	S Com	−2.00	63	185	9.7	4.1	0.62
XX And	−2.01	18	325	19.3	11.3	0.91	RY Com	−1.65	65	163	8.8	3.8	0.67
AT And	−0.97	10	292	12.5	7.6	0.91	ST Com	−1.26	−34	264	9.1	4.4	0.79
CI And	−0.83	276	113	21.5	2.6	0.38	V413 CrA	−1.21	86	191	8.6	3.8	0.62
DR And	−1.48	−94	357	16.0	6.6	0.83	TV CrB	−2.33	137	154	9.3	4.0	0.29
WY Ant	−1.66	−46	351	17.5	14.0	0.97	W Crt	−0.50	127	151	9.9	1.2	0.54
TY Aps	−1.21	8	247	7.7	7.0	0.80	X Crt	−1.75	−39	298	10.7	8.7	0.82
XZ Aps	−1.57	−17	243	8.1	5.7	0.94	UY Cyg	−1.03	214	45	9.1	0.3	0.00
SW Aqr	−1.24	3	369	18.2	9.5	0.94	XZ Cyg	−1.52	237	237	25.3	15.2	0.50
SX Aqr	−1.83	−67	482	34.9	16.9	0.88	DM Cyg	−0.14	272	96	15.5	2.2	0.30
TZ Aqr	−1.24	162	65	8.2	1.1	0.14	DX Del	−0.56	204	73	10.1	0.2	0.23
BO Aqr	−1.80	163	111	9.4	1.9	0.37	RW Dra	−1.40	97	123	8.5	1.0	0.35
BR Aqr	−0.84	180	62	8.5	1.7	0.01	SU Dra	−1.74	−104	325	9.3	0.5	0.00
BT Aqr	−0.29	144	75	7.5	0.9	0.30	SW Dra	−1.24	129	118	9.8	0.7	0.38
CP Aqr	−0.90	167	123	9.5	0.8	0.42	XZ Dra	−0.87	166	80	8.8	1.0	0.23
DN Aqr	−1.63	−3	383	25.9	13.0	0.95	AE Dra	−1.54	−150	426	14.3	00.6	0.31
AA Aql	−0.58	152	86	7.9	0.8	0.13	BC Dra	−2.00	−193	535	52.5	45.1	0.71
V341 Aql	−1.37	103	201	9.7	5.2	0.41	BK Dra	−2.12	104	227	13.6	7.6	0.52
S Ara	−1.43	96	193	10.1	0.9	0.66	BT Dra	−1.55	62	306	17.0	9.6	0.94
MS Ara	−1.48	21	220	7.4	4.8	0.92	RX Eri	−1.30	208	79	9.5	1.8	0.07
X Ari	−2.40	−44	264	9.0	0.5	0.83	SV Eri	−2.04	79	164	9.8	0.6	0.68
TZ Aur	−0.80	204	122	14.2	2.6	0.33	BB Eri	−1.51	−13	317	14.6	8.0	0.94
RS Boo	−0.32	243	31	10.6	1.0	0.09	SS For	−1.35	−13	295	10.6	10.3	0.72
ST Boo	−0.86	141	112	8.3	2.2	0.14	SX For	−1.62	−41	305	11.1	5.5	0.81
SW Boo	−1.12	−142	524	68.3	55.1	0.90	RR Gem	−0.35	231	57	12.3	0.6	0.18
SZ Boo	−1.68	101	119	8.1	2.0	0.33	SZ Gem	−1.81	−32	376	21.9	10.1	0.92
TW Boo	−1.41	−1	327	14.7	9.5	0.94	TW Her	−0.67	246	31	10.5	0.6	0.12
UU Boo	−1.92	5	372	19.9	11.2	0.96	VX Her	−1.52	−56	453	39.4	19.4	0.98
UY Boo	−2.49	27	284	13.1	8.0	0.93	VZ Her	−1.03	49	178	8.2	1.2	0.80
RW Cnc	−1.52	6	241	11.2	7.4	0.97	AR Her	−1.40	−224	510	33.6	3.1	0.80
SS Cnc	−0.07	130	135	10.0	3.9	0.32	DL Her	−1.32	239	112	11.7	3.1	0.25
TT Cnc	−1.58	95	290	17.5	14.9	0.48	GY Her	−1.92	170	205	17.8	5.6	0.57
AQ Cnc	−1.53	−146	486	33.4	5.1	0.79	SV Hya	−1.70	114	187	10.0	3.8	0.46
AS Cnc	−1.89	40	417	51.3	42.8	0.67	SZ Hya	−1.75	−145	406	16.6	5.2	0.68
W CVn	−1.21	132	106	8.5	1.7	0.36	UU Hya	−1.65	−24	343	15.9	6.9	0.89
Z CVn	−1.98	−6	245	9.9	6.6	0.98	WZ Hya	−1.30	−47	305	9.3	5.8	0.62
RU CVn	−1.37	60	273	15.0	7.4	0.80	XX Hya	−1.33	46	241	13.9	0.9	0.81
RZ CVn	−1.92	−21	384	24.6	15.0	0.96	DD Hya	−1.00	98	163	10.9	1.4	0.63
SS CVn	−1.52	12	354	20.1	19.0	0.99	DG Hya	−1.42	46	244	11.9	6.4	0.80
SV CVn	−2.20	10	279	13.5	8.7	0.99	DH Hya	−1.55	−24	393	22.1	1.7	0.90
SW CVn	−1.53	−37	259	9.4	4.9	0.81	ET Hya	−1.69	−104	375	10.1	7.9	0.14
UZ CVn	−2.34	−158	394	9.9	0.9	0.24	GO Hya	−0.83	186	60	9.7	1.4	0.01
AL CMi	−0.85	202	105	12.1	2.2	0.25	V Ind	−1.50	−62	397	19.2	8.3	0.88

Table 1. (Contd.)

Name	[Fe/H]	Θ, km/s	V_{res}, km/s	R_a, kpc	Z_{max}, kpc	e	Name	[Fe/H]	Θ, km/s	V_{res}, km/s	R_a, kpc	Z_{max}, kpc	e
RV Cap	−1.72	−316	567	31.6	12.4	0.61	CQ Lac	−2.04	231	46	11.1	0.7	0.09
V499 Cen	−1.56	−19	322	14.2	7.4	0.99	RR Leo	−1.57	154	130	11.1	1.2	0.44
RR Cet	−1.52	85	152	9.2	0.8	0.65	RX Leo	−1.38	75	231	11.9	7.8	0.58
RU Cet	−1.6	13	253	9.1	7.7	0.84	SS Leo	−1.83	−14	252	9.2	5.5	0.93
RV Cet	−1.32	61	189	9.1	4.9	0.63	ST Leo	−1.29	−77	307	9.2	3.8	0.64
RX Cet	−1.46	−43	417	27.8	3.2	0.94	SZ Leo	−1.86	−90	326	9.8	1.8	0.58
RZ Cet	−1.50	108	180	12.0	3.8	0.52	TV Leo	−1.97	339	132	30.8	5.9	0.56
UU Cet	−1.32	56	310	20.6	3.0	0.87	WW Leo	−1.48	45	244	12.3	9.7	0.60
XZ Cet	−2.27	152	190	12.4	6.1	0.41	AA Leo	−1.47	−39	277	10.7	6.2	0.91
RW Col	−1.03	271	302	47.4	5.4	0.82	AE Leo	−1.71	207	273	38.8	6.7	0.78
RX Col	−1.70	−18	384	19.9	2.5	0.87	AN Leo	−1.14	42	259	12.1	10.3	0.59
RY Col	−1.11	−169	525	43.4	16.4	0.82	AX Leo	−2.28	−161	420	13.8	3.3	0.47
V LMi	−1.15	82	278	20.3	2.5	0.81	RY Psc	−1.39	10	346	21.5	13.3	0.95
X LMi	−1.68	78	285	20.7	2.6	0.85	XX Pup	−1.50	−50	397	20.4	0.9	0.87
U Lep	−1.93	−145	371	10.6	0.7	0.45	HH Pup	−0.69	204	20	8.8	0.3	0.00
TV Lib	−0.27	288	107	16.4	1.6	0.41	V440 Sgr	−1.47	43	181	7.9	1.5	0.83
VY Lib	−1.32	−13	320	12.3	10.9	0.9	V675 Sgr	−2.01	214	188	14.9	5.0	0.45
TT Lyn	−1.76	104	309	23.0	18.5	0.66	V494 Sco	−1.01	203	33	7.9	0.3	0.01
TW Lyn	−1.23	249	62	14.2	2.1	0.18	RU Scl	−1.25	83	217	11.4	4.5	0.68
RR Lyr	−1.37	140	249	17.5	0.3	0.61	VX Scl	−2.25	−156	432	16.3	7.5	0.54
RZ Lyr	−2.13	67	266	15.1	2.3	0.78	VY Ser	−1.82	−72	418	21.8	10.6	0.85
CN Lyr	−0.26	274	77	13.7	0.4	0.20	AN Ser	−0.04	183	70	8.5	1.1	0.19
EZ Lyr	−1.52	179	116	11.0	0.9	0.33	AR Ser	−1.78	100	372	31.2	19.0	0.64
IO Lyr	−1.52	87	312	34.3	9.8	0.78	AT Ser	−2.05	172	81	8.0	1.5	0.19
Z Mic	−1.28	166	131	10.0	1.7	0.39	AV Ser	−1.20	232	52	9.8	0.9	0.15
RV Oct	−1.34	24	206	8.3	5.0	0.93	CS Ser	−1.57	195	284	25.0	16	0.64
RY Oct	−1.83	72	175	7.9	3.7	0.66	RV Sex	−1.10	153	143	10.3	3.1	0.40
SS Oct	−1.60	−158	379	8.3	1.1	0.16	RW TrA	−0.07	205	64	8.7	0.5	0.12
UV Oct	−1.61	−30	355	15.4	8.0	0.82	W Tuc	−1.64	94	140	8.4	1.9	0.54
ST Oph	−1.30	235	28	8.6	0.5	0.00	RV UMa	−1.19	−71	303	9.1	1.6	0.67
V413 Oph	−1.00	114	111	7.6	0.6	0.29	TU UMa	−1.44	−16	586	11.4	6.4	0.96
V445 Oph	−0.23	214	68	9.5	0.7	0.17	AB UMa	−0.72	113	118	9.1	1.2	0.49
V455 Oph	−1.42	−10	307	9.3	6.9	0.88	AF Vel	−1.64	29	308	17.6	8.2	0.89
WY Pav	−0.98	−3	320	11.6	6.6	0.90	ST Vir	0.88	121	117	7.9	1.8	0.42
BN Pav	−1.32	154	105	8.0	1.4	0.14	UU Vir	−0.82	141	192	12.8	1.4	0.61
BP Pav	−1.48	−266	478	18.5	2.7	0.63	UV Vir	−1.19	−1	245	9.5	6.5	0.91
VV Peg	−1.88	201	72	9.2	1.4	0.03	AF Vir	−1.46	−39	415	24.8	19.7	0.92
AV Peg	−0.14	164	69	8.7	0.5	0.16	AM Vir	−1.45	3	289	10.7	10.1	0.82
BH Peg	−1.38	−68	358	12.9	1.4	0.70	AS Vir	−1.49	39	266	12.2	8.1	0.77
CG Peg	−0.48	279	69	8.6	0.4	0.00	AT Vir	−1.91	−255	531	32.7	20.2	0.65
DZ Peg	−1.52	−142	362	8.7	1.3	0.35	AV Vir	−1.32	3	322	16.2	9.3	0.97
AR Per	−0.43	229	28	10.0	0.3	0.01	BB Vir	−1.61	43	296	14.6	8.1	0.91
RV Phe	−1.60	16	422	36.2	29.0	0.99	BQ Vir	−1.32	60	172	9.4	3.9	0.67
U Pic	−0.73	204	47	9.1	1.2	0.01	BN Vul	−1.52	−86	310	8.2	0.9	0.61

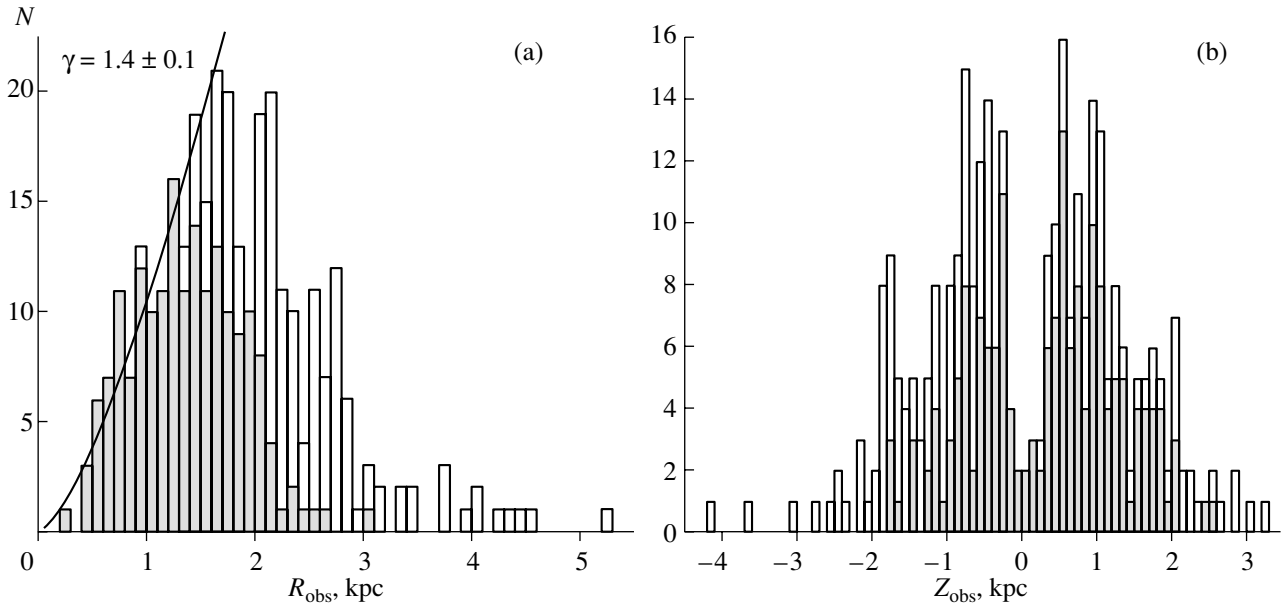

Fig. 1. Distributions of RR Lyrae stars in distance (a) from the Sun and (b) from the Galactic plane. The shaded part of the histogram corresponds to stars with known proper motions. The curve in the left histogram is a power-law approximation for the growth of the number of stars with distance in the initial sample for $R < 1.75$ kpc. γ is the power-law exponent. The dip in the right distribution near $Z \approx \pm 250$ pc is due to selection effects.

subsystems. Our choice of stars based solely on their type of variability ensures an absence of kinematic selection effects. However, since light curves can be obtained only for the relatively bright variables, our initial sample already has insufficient sampling depth to estimate the sizes of the oldest subsystems. Figure 1a presents the distributions of distance from the Sun for the stars in the initial sample. The solid line approximates the histogram with a function of the form $n = \alpha R_{\rm obs}^{\gamma}$ up to the class interval with the highest number (i.e., for $R_{\rm obs} < 1.75$ kpc). The power-law index was found to be $\gamma = 1.4 \pm 0.1$. The shaded areas in the histogram show the distributions for stars in our final sample with known spatial velocities. These are brighter and, naturally, on average closer to the Sun. Here, the number of stars grows with distance from the Sun in accordance with the same law as for the initial sample, but this is valid within a smaller radius. Even allowing for the uncertainties, the resulting relation clearly differs from the quadratic law that is expected if the observed volume is uniformly populated. In other words, the sample is not complete. This is due to the observational selection criteria used in [9], which included only stars more than 10° from the Galactic plane in order to reduce the final uncertainty in [Fe/H] due to interstellar reddening. This is apparent in Fig. 1b, where we find virtually no stars near $Z_{\rm obs} \approx \pm 250$ pc. It also appears that proper motions have been measured for a larger percentage of stars in the northern hemisphere ($Z > 0$). Note that the subsystems of the Galactic halo we are studying are large and that the selection effects primarily affect subsystems of the younger thin disk, so our samples should be sufficiently representative with respect to the halo subsystems.

3. CRITERIA FOR DISTINGUISHING THE SUBSYSTEMS

Objects belonging to the thick disk subsystem can be reliably distinguished based on their metallicity. In particular, the metallicity distribution of the globular clusters demonstrates an obvious depression near [Fe/H] ≈ -1.0, as well as abrupt changes in the velocity dispersions and distances from the Galactic center (cf., for instance, [14]). Figure 2a shows the metallicity function for the RR Lyrae stars in our initial sample. It can also be described by two normal curves at a high confidence level. A maximum-likelihood test shows that the probability that rejection of the best-fit single-Gaussian curve in favor of a two-Gaussian fit would be erroneous is $\ll 1\%$. The mean values and dispersions of the metallicities in the groups coincide with the corresponding parameters for globular clusters within the errors [14]. Like the globular clusters, the RR Lyrae stars in Fig. 2b demonstrate an abrupt change of the radial-velocity dispersions when the metallicity crosses a boundary value, equal in this case to $[{\rm Fe/H}]_{\rm bd} = -0.95$. Abrupt changes in the dispersion and maximum distance of

the stars from the Galactic plane are seen at the same metallicity in Fig. 2c.

Globular clusters also show an abrupt change of the dispersion of another intrinsic parameter near [Fe/H] ≈ -1.0, the morphological structure of the horizontal branch, which is closely related to the mean period of the RR Lyrae variables in the cluster. In addition, a similarity between the period distributions for field and globular-cluster RR Lyrae variables has been noted in several studies. For example, Carney [15] presents corresponding histograms (his Figs. 1.25 and 1.26) and discusses their bimodality and the similar positions of the two peaks. Figure 2d displays a metallicity–period diagram for the stars in our initial sample. However, the diagram shows no structural details apart from the well-known trend. Thus, we conclude that the variability periods of field RR Lyrae stars cannot be used as an additional criterion to identify objects belonging to the thick-disk subsystem.

Since this metallicity criterion for selecting thick-disk objects is clearly oversimplified, several criteria have been proposed to add metal-poorer stars to the subsystem. All use restrictions on the orbital velocity and are thus suitable only for stars with known proper motions. For example, Hanson *et al.* [5] proposed assigning all stars with velocities relative to the local centroid of the Sun below 125 km/s to the old disk, based purely on the fact that most metal-rich stars meet this criterion. We have plotted the corresponding vertical dashed line for the RR Lyrae stars in our final sample. The filled circles represent stars with [Fe/H] > -0.95. Virtually all lie to the left of the dashed line. The same area is also occupied by a fair number of metal-poorer stars, which form the low-metallicity tail of the thick disk. Note, however, that several metal-rich stars are found to the right of the line. If we increase the threshold velocity for the criterion to include these, the subsystem will include many stars located much higher above the Galactic plane than any of the metal-rich stars, increasing the characteristic size of the thick disk. To avoid this, a criterion also taking into account the star's location was suggested in [8] (see the slanting dashed line in Fig. 3a). In this case, the subsystem's characteristic size is obviously preserved, but the $|Z|_{\rm obs}$ distributions of stars with different metallicities remain different; the diagram shows that the highest density of metal-rich stars is reached at $Z_{\rm obs} < 0.5$ kpc (see also Fig. 4a below), and the highest density of stars in the low-metallicity tail occurs around $|Z|_{\rm obs} \approx 0.8$ kpc. Moreover, the number of RR Lyrae stars in the low-metallicity tail of the thick disk is as high as the total number of metal-rich stars. This contradicts the results obtained for nearby field stars, for which thick-disk stars were distinguished from the younger thin disk population. In particular, the recent detailed study [16] indicates that the low-metallicity tail of the thick disk essentially disappears near [Fe/H] ≈ -1.5. Apparently, if there is a low-metallicity tail of RR Lyrae stars, it must be identified using more complex criteria. The large uncertainties in the tangential velocities of distant stars, such as RR Lyrae variables, make it impossible to do this adequately. For this reason, we decided not to artificially assign any metal-poor stars to the thick-disk subsystem and we use only the primary criterion [Fe/H] > -0.95 when estimating the characteristic parameters of this subsystem. In our view, the fact that the ages of metal-rich globular clusters of the thick disk are considerably lower and essentially do not overlap the ages of protodisk halo clusters [14] is another argument against the existence of a low-metallicity tail, since this indicates that the time intervals for their formation were different.

It is much more difficult to identify objects that have an extragalactic origin; i.e., those belonging to the accreted halo. According to the hypothesis that the protogalaxy collapsed monotonically from the halo to the disk [17], stars genetically related to the Galaxy cannot have retrograde orbits. (Only the oldest halo stars may be exceptions, since they could have retrograde orbits due to the natural initial velocity dispersion of the protostellar clouds.) On the other hand, some stars formed from extragalactic fragments captured by the Galaxy should have prograde orbits. In any case, such stars should have fairly large residual spatial velocities relative to the local velocity centroid. Figure 3b displays the relation between this velocity and the azimuthal velocity component, Θ, for the RR Lyrae stars in our sample. We can see that there is a transition from prograde to retrograde orbits about the Galactic center near $V_{\rm res} \approx 290$ km/s. We also observe an abrupt increase in the dispersion of the azimuthal velocity component at the same place (see the error bars in the diagram). Figure 3c displays a significant increase in the scatter of the stars in $Z_{\max}$ when crossing the same threshold residual spatial velocity. The abrupt change in the apogalactic radii of the stellar orbits is even more evident (Fig. 3d). Both the orbital eccentricities and their dispersion abruptly increase when crossing the same point (Fig. 3e) and they also demonstrate different relations. First, the orbital eccentricities increase almost linearly with the residual velocities, reaching a maximum near the threshold velocity level. With further increase in $V_{\rm res}$, the mean and scatter of the eccentricities do not change within the errors. It is interesting that the metal abundances also demonstrate different behavior in different areas of Fig. 3f. First, we observe a clear metallicity decrease with increasing velocity, after which the metal abundance

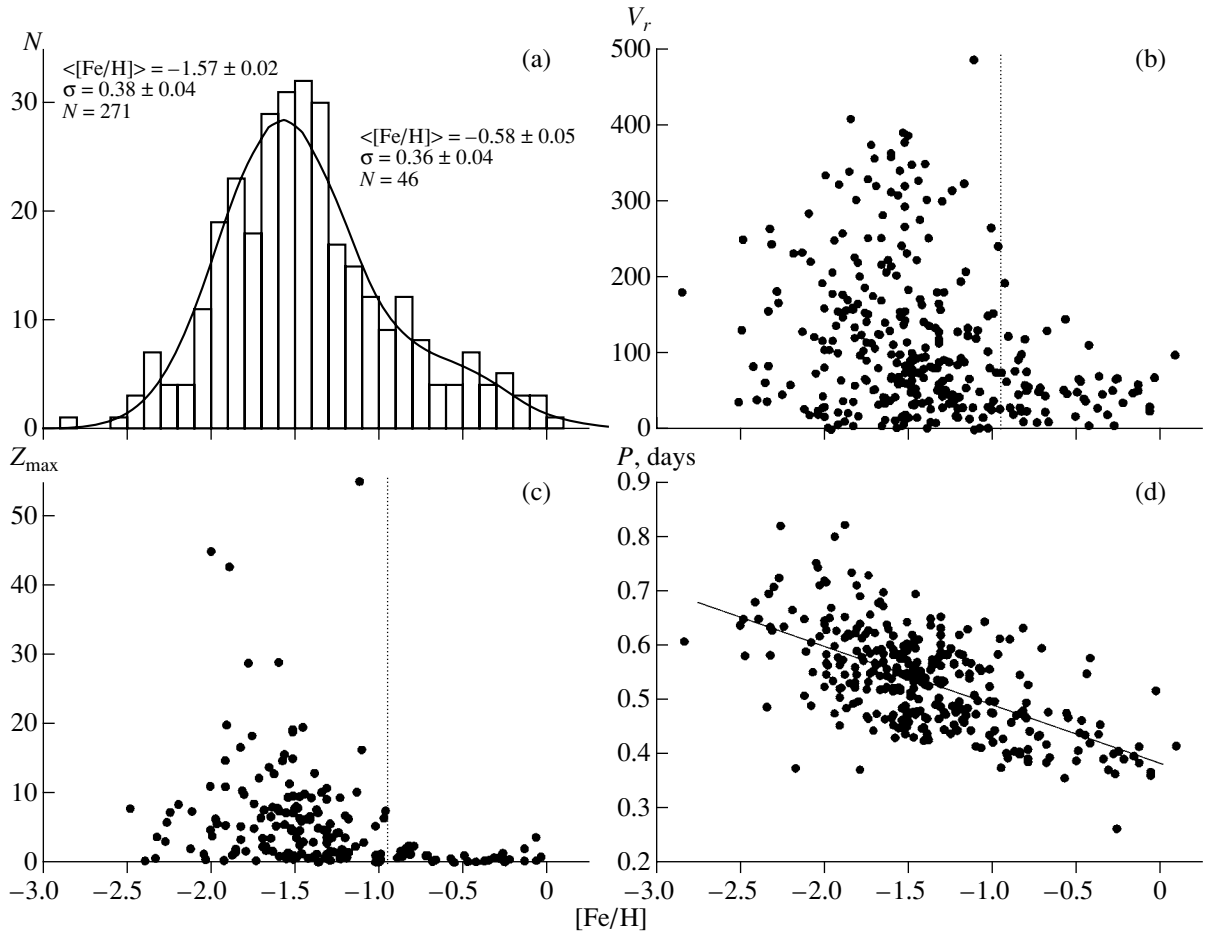

Fig. 2. (a) Metallicity function and relations between (b) metallicity and radial velocity, (c) metallicity and maximum distance from the Galactic plane, and (d) metallicity and variability period for RR Lyrae variables in the initial sample. The curve in the first graph is the maximum-likelihood approximation of the distribution using a sum of two normal curves with the indicated means, dispersions, and total numbers. The dashed vertical lines in the second and the third panels are visual estimates of the location of the abrupt increase in the scatter of V_r and $Z_{\max}$ at [Fe/H] $= -0.95$.

remains virtually unchanged and there is an appreciable decrease in its scatter. For this reason, we adopt $V_{cr} \approx 290$ km/s as the critical value for distinguishing stars of the outer halo ($V_{res} > V_{cr}$). We suggest that stars with lower residual velocities have a Galactic origin and belong to the thick-disk and protodisk halo subsystems. Apparently, this kinematic criterion is not entirely unambiguous: some stars of the protodisk halo may have larger residual spatial velocities. Evidence for this is provided, in particular, by the increase in the stellar density immediately to the right of V_{cr} in our diagrams. However, we decided (as for the thick disk) to retain a simple criterion in order not to artificially confuse the situation.

Note again that the principal criteria distinguishing globular clusters of the young halo are their redder horizontal branches and, simultaneously, the lower mean periods of their RR Lyrae stars compared to clusters of the protodisk halo. To test this circumstance for field stars, we computed the mean periods of stars in a narrow metallicity range ($-1.7 <$ [Fe/H] < -1.2) for both halo subsystems. Each sample contained about forty stars. Their mean periods were the same. Thus, the variability periods of field RR Lyrae stars cannot serve as an additional criterion to divide them into the subsystems of the metal-poor halo, similar to the case of the thick disk.

Let us now compare the properties of the resulting subsystems.

4. PROPERTIES OF STARS IN THE SUBSYSTEMS

Since the membership of stars in the thick disk is determined by their metallicity, we are able to first consider a number of properties of this subsystem using the initial sample of RR Lyrae stars then compare these properties to the results obtained for the smaller

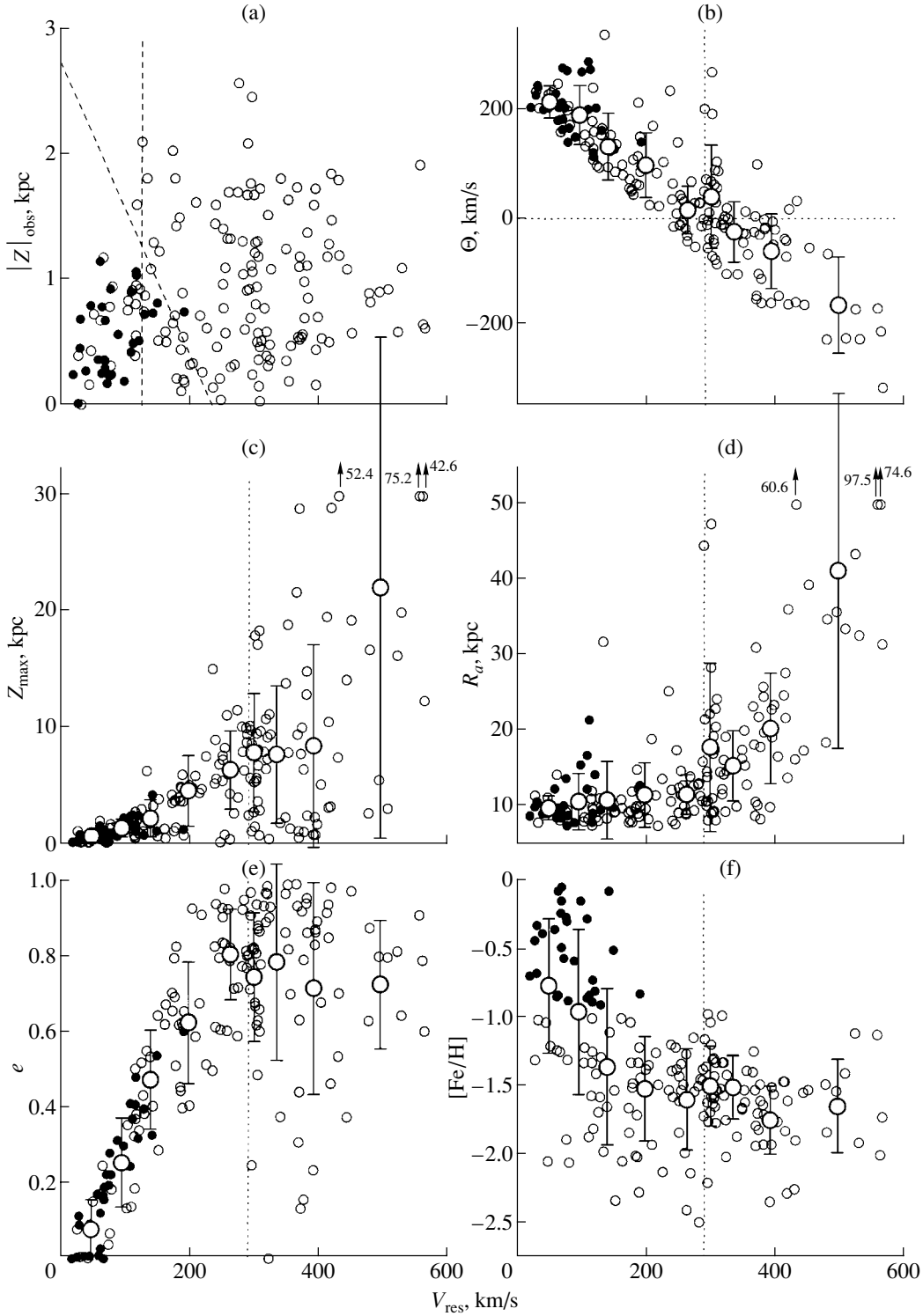

Fig. 3. Relations between the residual spatial velocity and other characteristics of the RR Lyrae stars. The filled circles represent stars with [Fe/H] > −0.95; the large open circles with error bars are mean values and dispersions of the corresponding parameters in narrow intervals of V_{res}. The vertical and slanted dashed lines in the first panel mark the separation distinguishing areas occupied by thick-disk objects according to [5] and [8], respectively. An abrupt change in the dispersion near $V_{res} \approx 290$ km/s (the vertical dashed lines) is apparent in all panels except the first.

number of stars that have known spatial velocities and orbital elements. The characteristic feature of the thick disk is its rapid rotation, which results in considerable flattening toward the Galactic plane.

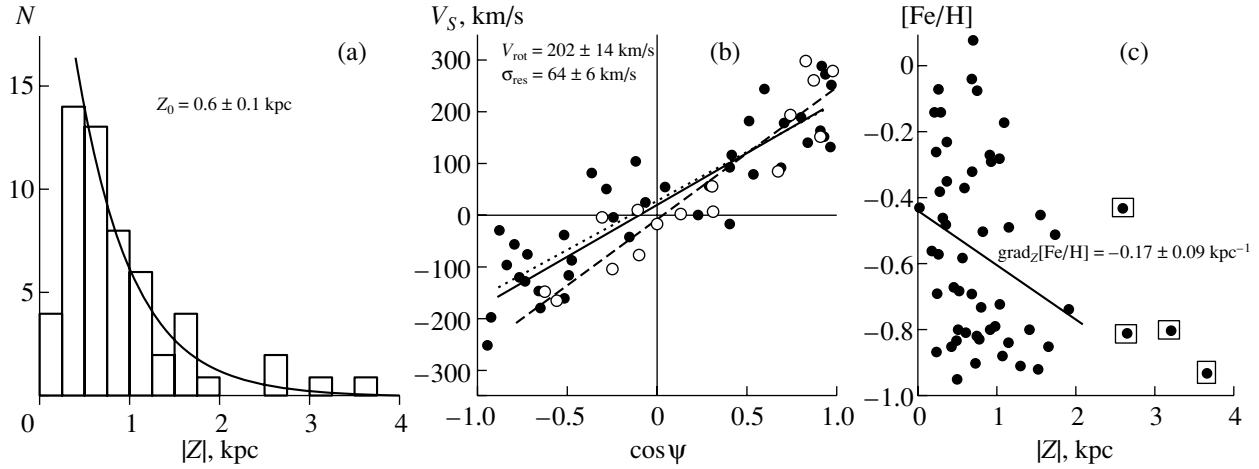

Fig. 4. (a) Distribution of distance from the Galactic plane, (b) kinematic diagram, and (c) relation between metallicity and distance from the Galactic plane for RR Lyrae stars with [Fe/H] > -0.95. The curve in the left panel approximates the distribution with an exponential law with scale height Z_0. The solid line in the middle panel is a regression line, whose slope is determined by the subsystem's rotation rate; the open circles and dashed line correspond to stars with [Fe/H] > -0.4, and the filled circles and dashed line, to stars with $-0.95 <$ [Fe/H] < -0.4. The line in the right panel is a least-squares regression line for $|Z| < 2$ kpc, whose slope is determined by the metallicity gradient; the squares show distant stars excluded from our computations.

In particular, the natural logarithmic scale height of the density of globular clusters in the thick disk is ≈ 1.0 kpc. As shown above, the sampling depth of our initial sample is considerably larger, so we can derive the scale height (Z_0) of the subsystem of metal-rich RR Lyrae stars from their observed positions.

Figure 4a shows that the scale height of the thick disk at the solar distance from the Galactic center is even somewhat lower than for globular clusters that are close to the center. Assuming nonrigid rotation of the subsystem with a constant linear velocity, we can obtain a least-squares fit to this velocity based solely on the radial velocities and observed positions of the studied stars (see [18] for details of the method). Figure 4b presents the corresponding $\cos\psi - V_S$ kinematic diagram, where ψ is the angle between the line of sight and the vector for rotation about the Z axis and V_S is the star's radial velocity reduced to an observer at rest at the position of the Sun. The slope of the least-squares regression line determines the rotational velocity of the subsystem of metal-rich stars, $V_{\rm rot} = 220 \pm 14$ km/s, whereas the scatter around it determines the dispersion of the residual velocities, $\sigma_{\rm res} = 64 \pm 6$ km/s; the correlation coefficient is quite high, $r = 0.9 \pm 0.1$. Using the apparent positions of the stars, we can also follow variations of the metallicity with distance from the Galactic plane (Fig. 4c). The regression line derived for the majority of the stars (i.e., those closer than 2 kpc) indicates a considerable negative vertical metallicity gradient, $\mathrm{grad}_Z[\mathrm{Fe/H}] = -0.17 \pm 0.09$ kpc^{-1}, with $r = 0.3 \pm 0.1$. This result is stable: when distant stars are included, the absolute value of the gradient decreases but remains outside the errors. However, stars with $Z_{\rm obs}$ that are that high above the plane (beyond 3σ) do not necessarily belong to the disk subsystem.

Note that the resulting high rate of rotation of the subsystem of metal-rich RR Lyrae stars, which coincides with the Galactic rotational velocity at the distance of the Sun within the errors, probably testifies to the presence of thin-disk stars. If we divide the sample into two groups, for example, at [Fe/H] $= -0.4$, the more metal-rich group will demonstrate a much higher rotational velocity in the kinematic diagram (Fig. 4b). Due to the spatial observational selection criteria used, our initial sample lacks stars closer to the Galactic plane than $Z_{\rm obs} = \pm 250$ pc; since the scale height for the subsystem of old thin-disk stars is in this range [19], we cannot address this problem in more detail in the present study.

The spatial velocities of the stars can be used to verify the above results for the metal-rich stars, and also to obtain estimates for a number of characteristics for both halo subsystems, if we can first reconstruct the stars' Galactic orbits. Figure 5 shows the distributions of the stars in our three subsystems in the elements of their Galactic orbits. The top row presents histograms of the rotational velocities for stars of the thick disk, protodisk halo, and outer accreted halo. All three distributions can be quite satisfactorily represented with normal laws (the curves in the histograms), whose maxima are separated nearly by the corresponding dispersion (Table 2). The good agreement between the mean rotational velocities and

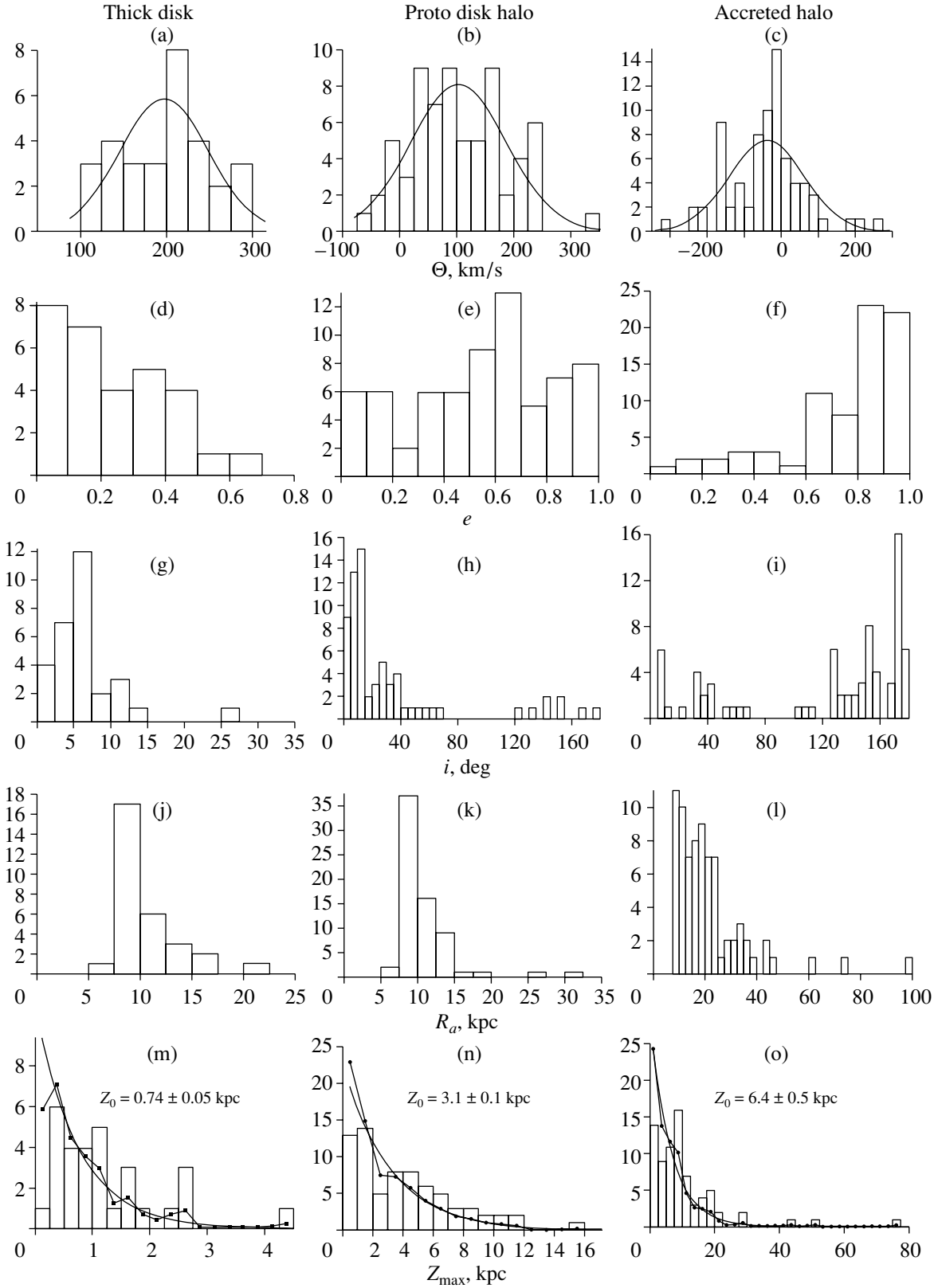

Fig. 5. Distribution of orbital elements for the RR Lyrae stars. Results for stars with [Fe/H] > -0.95 (left column), [Fe/H] < -0.95 and $V_{res} < 290$ km/s (middle column), and [Fe/H] < -0.95 and $V_{res} > 290$ km/s (right column) are shown separately. In the top row, we have plotted normal curves fitting the distributions. In the bottom row, the segmented lines are the reconstructed distributions of RR Lyrae stars in Z (see text for details), and the curves approximate the distributions with exponential laws (the corresponding scale heights are indicated).

Table 2. Characteristics of the subsystems of RR Lyrae (ab) variables

Parameters of RR Lyrae stars	Thick disk	Protodisk halo	Accreted halo
Number of stars	30	68	76
$\langle$[Fe/H]$\rangle$	-0.57 ± 0.05	-1.54 ± 0.04	-1.59 ± 0.04
$\sigma_{\rm [Fe/H]}$	0.28 ± 0.03	0.36 ± 0.03	0.29 ± 0.03
$\langle\Theta\rangle$, km/s	198 ± 9	104 ± 10	-40 ± 12
σ_Θ, km/s	51 ± 7	84 ± 7	101 ± 8
$\langle e\rangle$	0.23 ± 0.03	0.54 ± 0.03	0.75 ± 0.03
$\lim r_{\rm max}$, kpc	13	15	40
$\lim z_{\rm max}$, kpc	2	10	22
Z_0, kpc	0.74 ± 0.05	3.1 ± 0.1	6.4 ± 0.5
grad_R[Fe/H], kpc^{-1}	-0.03 ± 0.04	-0.03 ± 0.02	-0.00 ± 0.01
grad_Z[Fe/H], kpc^{-1}	-0.23 ± 0.10	-0.03 ± 0.02	-0.00 ± 0.01

their dispersions for the metal-rich stars derived from radial velocities (Fig. 4b) and spatial velocities (Table 2) testifies to the good accuracy of the proper motions and the photometric distance scale used. The second row of histograms in Fig. 5 shows the corresponding distributions in orbital eccentricity. The characters of these histograms are obviously very different. The disk has virtually no stars with $e \geq 0.5$, all eccentricities are present in approximately equal numbers in the protodisk halo, and stars with very eccentric orbits dominate in the outer halo (where almost two thirds of all stars have $e > 0.8$). The next row (Figs. 5g–5i) presents the distributions in orbital inclination. As expected, the orbital inclinations of the disk stars are very low, not exceeding 15°. The stars of the two spherical subsystems can have any orbital inclination. In both cases, the number of stars strongly increases with decreasing inclination; however, this is true for stars with prograde orbits in the protodisk halo and for those with retrograde orbits in the outer halo. We must bear in mind that the deficit of stars with large orbital inclinations is largely due to the kinematic selection effect imposed on the sample. The vertical components of the spatial velocities of such stars in the solar neighborhood should be comparable to the Galactic rotational velocity at this distance. Thus, the probability of their presence here is very low.

The fourth row of histograms (Figs. 5j–5l) can be used to estimate the radial sizes of the subsystem, and the fifth row (Figs. 5m–5o), their vertical sizes at the solar Galactocentric distance. Let us attempt to make a quantitative estimate of the outer sizes of the subsystems based on these distributions, using the standard rules of thumb for the behavior of an upper envelope, often applied in observational astronomy. For example, when selecting members of an open cluster, it is usual to reject the five brightest stars as possible field stars. Proceeding in this fashion, we simultaneously eliminate the largest uncertainties in the orbital elements and avoid possible errors in assigning some stars in our sample to a particular subsystem. Such estimates indicate that the outer sizes of the genetically related subsystems are comparable, whereas the outer halo is approximately a factor of three larger (Table 2). The sizes of the subsystems perpendicular to the Galactic plane differ more dramatically: the half-thickness of the thick disk is smallest, that of the protodisk halo is several times larger, and that of the outer halo is nearly an order of magnitude larger (Table 2).

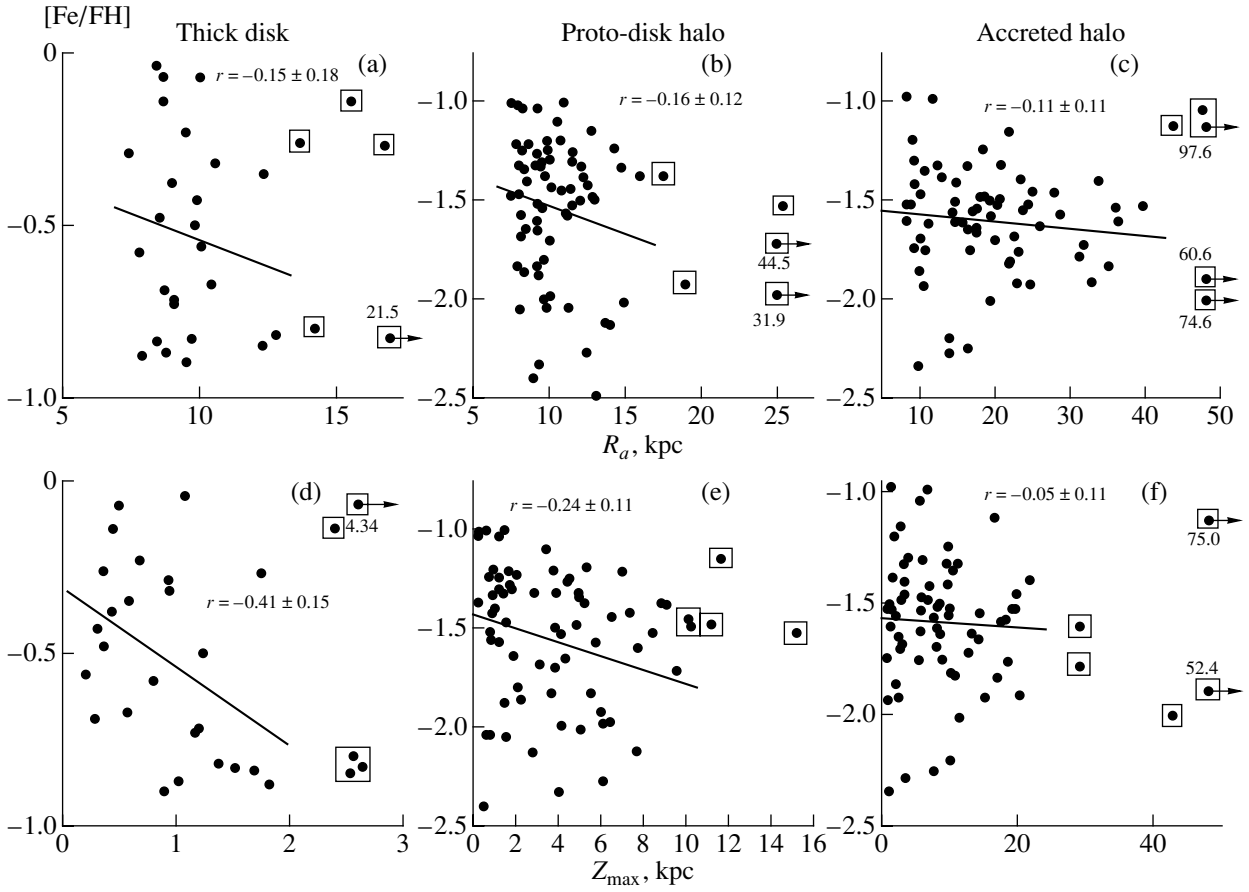

Fig. 6. Metallicities of the RR Lyrae stars as a function of apogalactic distance (a, b, c) and maximum distance from the Galactic plane (d, e, f). The straight lines are least-squares fits. The five most distant stars in each panel (in boxes) were excluded from our calculations. The correlation coefficients and their uncertainties are indicated.

It is obviously not correct to compute the scale height using Z_{max}, since all stars in a subsystem cannot simultaneously be located at the highest points of their orbits. To reconstruct the "real," instantaneous distributions of each subsystem from the Z values, we must spread each star over its orbit in proportion to the probability density of the star being located at each point of the orbit. This probability density can easily be found from the computed orbit of the star; the details of the procedure can be found in [19]. The segmented lines in the bottom row of histograms (Figs. 5m–5o) show the Z distributions for each subsystem reconstructed in this manner. In other words, this is how the stars will be distributed in height after some time if they are distributed randomly in their orbits. The solid curves in Figs. 5m–5o are least-squares approximations to the reconstructed distributions using an exponential law, $n = \alpha \times e^{-Z/Z_0}$, where Z_0 is the scale height (the corresponding Z_0 values are indicated in Figs. 5m–5o and Table 2). In this procedure, we did not take into account the first interval of Z_{max} for the segmented line corresponding to the thick disk, since the number of objects in this interval is far too low due to the observational selection criteria. (In all cases, we excluded the five most distant stars when evaluating the scale height.) Note the good agreement of the scale heights for the thick disk estimated from the observed positions and from the reconstructed distribution in $|Z|_{obs}$ (Fig. 4a).

Let us now consider the metallicity gradients in the subsystems. Figure 6 displays R_a – [Fe/H] and Z_{max} – [Fe/H] diagrams for each of the subsystems. The straight lines are least-squares fits. Assuming that the stars are born near the apogalactic radii of their orbits, the slopes of these lines reflect the initial radial and vertical metallicity gradients for the subsystems. To increase the trustworthiness of the gradient estimates, we rejected the five most distant data points in each case. The resulting gradients are presented in Table 2, and the correlation coefficients, in the corresponding diagrams. Only the vertical gradient in the thick disk appreciably exceeds the errors and has a high correlation coefficient. This gradient coincides within the errors with the value derived above (Fig. 4c) from the observed positions of the

stars, testifying to the reliability of the result. The radial metallicity gradient in the disk is zero within the errors. In the protodisk halo, small gradients with similar magnitudes, only slightly exceeding their uncertainties, are found. The correlation coefficients given in Figs. 6b and 6e will become smaller if we add the five excluded distant stars but will remain nonzero. Thus, the existence of gradients in the protodisk halo is still an open question. In contrast, the complete absence of both gradients for the RR Lyrae stars of the accreted halo is beyond doubt.

5. DISCUSSION

The thick-disk objects can be reliably distinguished from halo objects due to the abrupt change of their spatial distribution and their velocity dispersion when crossing the threshold value [Fe/H] ≈ -1.0. Thick-disk globular clusters selected using the same criterion have $Z_0 = 1.0 \pm 0.2$ kpc, $\langle[\mathrm{Fe/H}]\rangle = -0.56 \pm 0.05$, $\sigma_{[\mathrm{Fe/H}]} = 0.28 \pm 0.03$, $V_{\mathrm{rot}} = 165 \pm 38$ km/s, $\sigma_{\mathrm{res}} = 88 \pm 15$ km/s, $\mathrm{grad}_R[\mathrm{Fe/H}] = -0.01 \pm 0.02$ kpc^{-1}, and $\mathrm{grad}_Z[\mathrm{Fe/H}] = -0.16 \pm 0.06$ kpc^{-1}. Comparing these to the parameters of the subsystems of RR Lyrae stars from Table 2, we find that the mean metallicities for the clusters and for our field stars nearly coincide. However, the metallicity function of the thick-disk globular clusters has a well-defined depression in the number of clusters near the threshold metallicity, while the corresponding distribution for the field RR Lyrae stars does not show such a dip. (There is even a local rise near [Fe/H] ≈ -0.85.) Though the rotational velocities of the subsystems are the same within the errors, the velocity for the RR Lyrae stars was $\sim$35 km/s higher due to the contribution of thin-disk stars to the sample. The appreciable velocity dispersion of the disk globular clusters is probably the result of the large uncertainty in the computed $\cos\psi$ values for clusters near the Galactic center. The corresponding gradients are essentially the same for the subsystems, whereas the scale height for the clusters is higher by approximately one-third. A natural explanation is that some of the metal-rich clusters near the Galactic center probably belong to the bulge. The difference in the limiting radial sizes of the subsystems is more difficult to explain: this size is $\sim$13 kpc for the field RR Lyrae stars, whereas almost no metal-rich globular clusters are observed beyond $\sim$7 kpc (this may simply be due to the statistically small sample of globular clusters in the thick disk). Based on the coincidence of all but the last characteristic of the metal-rich subsystems of these different objects, we suggest that both the globular clusters and the field RR Lyrae stars with [Fe/H] ≥ -1.0 belong to the same subsystem of the Galaxy—the thick disk.

Let us now turn to the thick disk's low-metallicity tail. Of course, the abrupt end of the metallicity distribution at [Fe/H] $= -1.0$ seems artificial. The maximum-likelihood method also requires a much higher metallicity dispersion, as can be seen in a comparison of the data in Fig. 2 and Table 2. Therefore, it is natural to wish to smooth the metallicity function by including in the subsystem metal-poorer stars that do not reach large distances from the Galactic plane and have large orbital velocities. This does not cause significant changes in any of the characteristic spatial or kinematic parameters of the subsystem. However, adding metal-poor, low-Z stars to the sample completely removes the vertical metallicity gradient in the disk. This is the reason for the contradictory results concerning this gradient obtained in different studies and for disagreements about models for the formation and evolution of this subsystem. The presence of a vertical gradient would provide evidence for a slow, dissipative collapse as the mechanism for the formation of the thick disk, whereas the absence of a vertical gradient would rule out this process. We are inclined to believe that the stars in the low-metallicity tail of the disk (if there are any) probably formed from low-metallicity gas and dust fragments weakly interacting with the bulk of the parent protodisk cloud, where star formation (and hence enrichment in heavy elements) was suppressed for a long time. In this case, low-metallicity disk stars can be located in a thin layer of the Galaxy, considerably reducing the observed vertical metallicity gradient among genetically related stars of the subsystem.

Let us now consider the halo stars. As earlier, we will compare the characteristics of the metal-poor RR Lyrae stars derived in this study to the parameters of corresponding subsystems of globular clusters from [14], since only these objects were distinguished based on an intrinsic, physical parameter rather than interrelated spatial and kinematic criteria. The metallicity distributions of corresponding halo subsystems differ somewhat. In particular, the mean metallicity of the protodisk halo derived from globular clusters is lower than that of the outer halo. The metallicity dispersion is also lower. The field stars show the opposite pattern (Table 2). In all cases, however, the differences are comparable to the formally computed uncertainties, indicating that any conclusions about differences between these parameters have low statistical significance. The gradients in the protodisk halo are completely consistent. In the accreted halo, both gradients are absent for the field RR Lyrae stars but nonzero for the clusters. However, both gradients for the globular clusters are due exclusively to metal-richer objects close to the Galactic center ($R \lesssim 7$ kpc), and objects that far from the Sun do not enter our sample of field RR Lyrae stars. We have identified

the halo subsystems based on spatial velocity, and differences between the protodisk halo and accreted halo in any kinematic parameter should be more prominent. Indeed, while the orbital velocities for the globular clusters of the protodisk halo and the accreted halo are 77 ± 33 km/s and -23 ± 54 km/s, so the difference between them is ~ 100 km/s, this difference is approximately 40% higher for the RR Lyrae stars (Table 2). The velocity-dispersion estimates for the subsystems of globular clusters (129 ± 19 km/s and 140 ± 18 km/s) are obviously overestimated due to the large distance uncertainties, and, as a result, they are much higher than the values for the field RR Lyrae stars. The mean eccentricities in the protodisk halo subsystems are the same, whereas, in the outer halo, the eccentricities are, on average, higher for the field stars, as expected (note that orbital eccentricities are known only for a small number of clusters, and with large uncertainties). The radial size of the protodisk halo was approximately a factor of 1.5 larger for the field stars than for the clusters, whereas the two scale heights were the same within the errors. Recall that we can estimate the radial sizes of RR Lyrae subsystems only from their maximum distances from the Galactic center, which leads to appreciable overestimation of these sizes. The radial and vertical sizes of the outer accreted halo subsystem of field stars are naturally the largest and are in reasonable agreement with the corresponding sizes for the subsystem of globular clusters. Note that, in order to obtain correct estimates of sizes of Galactic subsystems based on data for nearby stars, it is necessary to take into account the kinematic selection effects, which lead to a deficiency of stars with large R_a and Z_{max} in the solar neighborhood.

Thus, the generally good agreement between the characteristics of corresponding subsystems of field RR Lyrae stars and globular clusters distinguished using different criteria shows that both populations are not uniform. Both the clusters and field stars belong to at least three Galactic subsystems: the thick disk, the genetically related inner protodisk halo, and the outer accreted halo. The collected results indicate that this subsystem is characterized by large size, an absence of appreciable metallicity gradients, predominantly large orbital eccentricities, a large number of objects in retrograde orbits, and younger ages for its objects, supporting the hypothesis that this subsystem had an extragalactic origin.

ACKNOWLEDGMENTS

The authors are grateful to the anonymous referee, who found several inconsistencies in the manuscript. This study was supported by the Russian Foundation for Basic Research, project nos. 00-02-17689 and 01-02-06449.

REFERENCES

1. F. D. A. Hartwick, in *The Galaxy,* Ed. by G. Gilmore and B. Carwell (Reidel, Dordrecht, 1987), p. 281.
2. R. Zinn, in *The Globular Cluster—Galaxy Connection,* Ed. by H. Smith and J. Brodee, Astron. Soc. Pac. Conf. Ser. **48**, 38 (1993).
3. S. R. Majewski, Astrophys. J., Suppl. Ser. **78**, 87 (1992).
4. B. W. Carney, Publ. Astron. Soc. Pac. **108**, 900 (1996).
5. R. B. Hanson, C. Sneden, R. P. Kraft, and J. Fulbright, Astron. J. **116**, 1286 (1998).
6. A. C. Layden, Astron. Soc. Pac. Conf. Ser. **136**, 14 (1998).
7. M. Chiba and Y. Yoshii, Astron. J. **115**, 168 (1998).
8. J. C. Martin and H. L. Morrison, Astron. J. **116**, 1724 (1998).
9. A. C. Layden, Astron. J. **108**, 1016 (1994).
10. R. Zinn and M. J. West, Astrophys. J., Suppl. Ser. **55**, 45 (1984).
11. A. C. Layden, R. B. Hanson, S. L. Hawley, *et al.*, Astron. J. **112**, 2110 (1996).
12. D. L. Lambert, J. E. Heath, M. Lamke, and J. Drake, Astrophys. J., Suppl. Ser. **103**, 183 (1996).
13. C. Allen and A. Santillan, Rev. Mex. Astron. Astrofis. **22**, 255 (1991).
14. T. V. Borkova and V. A. Marsakov, Astron. Zh. **77**, 750 (2000) [Astron. Rep. **44**, 665 (2000)].
15. B. W. Carney, *Globular Clusters* (Univ. Chapel Hill, USA, 1999).
16. J. X. Prochaska, S. O. Naumov, B. W. Carney, *et al.*, Astron. J. **120**, 2513 (2000).
17. O. J. Eggen, D. Lynden-Bell, and A. Sandadge, Astrophys. J. **136**, 748 (1962).
18. R. Zinn, Astrophys. J. **293**, 424 (1985).
19. V. A. Marsakov and Yu. G. Shevelev, Astron. Zh. **72**, 630 (1995) [Astron. Rep. **39**, 559 (1995)].

Translated by N. Samus'

Astronomy Reports, Vol. 46, No. 6, 2002, pp. 474–480. Translated from Astronomicheskiĭ Zhurnal, Vol. 79, No. 6, 2002, pp. 526–533.

Search for the General Magnetic Fields in Late-Type Giants

T. N. Tarasova

Crimean Astrophysical Observatory, p/o Nauchnyĭ, Crimea, 334413 Ukraine

Received November 15, 2001; in final form, November 23, 2001

Abstract—Surface-averaged longitudinal magnetic-field components (by analogy with the Sun called the general magnetic field) have been measured for 15 late-type giants with an accuracy of several Gauss. Statistically significant fields were detected for nine of these stars. The magnetic-field values obtained suggest the existence of general magnetic fields in these giants. © *2002 MAIK "Nauka/Interperiodica".*

1. INTRODUCTION

Studies of late-type stars have indicated that many display all the signs of solar-type activity: chromospheres and coronae, cycles of activity, and flares. All these manifestations of activity are associated with magnetic fields. Currently, magnetic fields have been detected and measured both indirectly [1–10] and directly in several types of stars, including T Tauri stars, RS CVn stars, solar-type stars, and M-dwarf flare stars [11–13].

The most active giants, which belong to RS CVn binaries, possess active regions and flares qualitatively similar to those on the Sun. In one such star (α Aur), a solarlike activity cycle has been detected using observations of the 10 830 Å neutral helium line [14]. Quantitatively, however, these stars are substantially more active than the Sun (both the size and total energy of their active regions exceed the corresponding solar parameters by several orders of magnitude). This is due to the fact that the axial and orbital motions in these systems are synchronized, which maintains a relatively high rotational velocity. Apart from their solarlike activity, RS CVn stars also display other types of activity associated with their binarity. These processes are due to interactions between the stellar winds from the two components and, possibly, between their magnetospheres [15].

Studies of the UV and X-ray emission from late-type giants less active than RS CVn stars have indicated that this radiation is also related to magnetic activity. The detection of X-ray flares in the single giant β Boo A [16] and the so-called hybrid giant α Tr A [17] also provides evidence for magnetic activity.

Studies of the activity of giants later than F0 at UV and X-ray wavelengths have indicated that a division can be marked in the HR diagram, with giants displaying dramatically different activity on opposite sides of this division. In giants on the blue (left) side of the dividing line, UV (CIV, SiIV, and other lines) [21] and X-ray [18–20, 46] radiation is detected, typical of the transition zone and coronal region of the Sun, respectively. The UV spectra of giants on the red (right) side of the division show only lines characteristic of the solar chromosphere (OI, SI, SiI, etc.), and essentially no X-ray emission from these stars is detected. At the same time, these giants display evidence of cool ($T \sim 20\,000$ K), massive ($\dot{M} \sim 10^{-10}$–$10^{-7} M_\odot$/yr) stellar winds [22–26], similar to those observed in solar coronal holes. So-called hybrid giants with mixed signs of activity [23, 24, 27] occupy an intermediate position between these two types.

The differences in the types of activity shown by the two groups of giants may be associated with the dominance of different types of magnetic-field structures on opposite sides of the dividing line [28].

Currently, the magnetic-field structures of rapidly rotating RS CVn stars and late-type dwarfs are best studied, since tomographic techniques can be applied in these cases. Mapping has revealed complicated structures for their magnetic fields, apparently manifestations of the toroidal and poloidal components of the large-scale magnetic field generated by the dynamo mechanism [29, 30]. Tomography cannot be applied to slowly rotating giants, and only direct measurements of the surface-averaged magnetic field (which we call the general magnetic field, by analogy with the Sun) can be made. Such measurements have been carried out by Borra *et al.* [31] and Hubrig *et al.* [32]. Borra *et al.* [31] reported a possible detection of the magnetic field of the RS CVn star UX Ari. Hubrig *et al.* [32] detected isolated cases of magnetic fields of several tens of gauss in four of twelve giants.

However, these data were insufficient to study the magnetic-field structures of late-type giants. Our goal was to obtain additional measurements of the magnetic fields in such objects.

1063-7729/02/4606-0474$22.00

Table 1. Magnetic-field strengths for the studied stars

Object	Date	JD 2400000+	B_e, G	σ, G	B_e/σ	References
δ And	Dec. 27, 1998	51175.173	7.7	1.7	4.5	
	Dec. 19, 1999	51532.254	8.5	2.8	3.0	
β And	Dec. 28, 1998	51175.213	12.6	2.2	5.7	
		45294.311	−0.1	2.4		[31]
η Psc	Sept. 14, 1998	51070.535	−2.6	3.8		
	Sept. 22, 1999	51443.570	0.9	5.4		
	Nov. 18, 2000	51867.324	11.4	3.9	2.9	
κ Gem	Nov. 11, 1998	51128.571	11.7	2.1	5.6	
	Nov. 16, 2000	51865.463	13.0	3.8	3.4	
β Gem	Nov. 11, 1998	51128.641	3.0	2.6		
	Sept. 25, 1999	50351.545	−5.5	3.7		
		45291.641	3.3	2.0		[31]
		45419.347	−3.2	1.5		[31]
		48643.353	−3.6	2.5		[32]
		48643.353	0.6	4.2		[32]
		48677.376	−3.3	8.8		[32]
		48678.378	16.9	8.2		[32]
		48709.234	12.3	6.8		[32]
β Cnc	Feb. 11, 1999	51221.478	3.1	2.5		
	Nov. 17, 2000	51865.544	−4.0	1.9		
ζ Hya	Dec. 19, 1997	50801.639	−15.3	2.9	5.3	
ϵ Vir	Jan. 2, 1999	51180.623	−10.8	3.2	3.4	
		45420.483	−3.2	5.4		[31]
		48728.251	−2.6	4.1		[32]
		48730.241	−10.2	4.9		[32]
		49040.360	−9.6	4.8		[32]
α Boo	May 15, 1998	50949.451	1.3	1.0		
		45111.476	−0.3	1.1		[31]
		45113.472	1.6	1.2		[31]
		45417.472	3.3	0.5	6.6	[31]
		45428.542	−1.1	1.5		[31]
		47616.565	8.5	8.8		[32]
		47643.432	2.3	2.5		[32]
		48021.298	2.9	1.8		[32]
ϵ Boo A	March 6, 1999	51244.459	−8.8	3.4		
α Ser	March 26, 1999	51264.481	2.4	1.8		
η Her	Apr. 20, 1999	51289.489	−5.7	5.3		

Table 1. (Contd.)

Object	Date	JD 2400000+	B_e, G	σ, G	B_e/σ	Reference
ϵ Cyg	Oct. 5, 1998	51092.231	9.3	2.5	3.7	
	July 27, 1999	51387.401	−2.6	1.4		
	July 29, 1999	51389.371	−8.7	2.6	3.4	
	July 30, 1999	51390.354	2.3	1.7		
	July 31, 1999	51391.409	3.3	1.5		
	Sept. 1, 1999	51423.477	1.8	1.7		
	Dec. 15, 2000	51894.188	0.1	2.9		
ζ Cyg	Oct. 6, 1998	51093.383	5.4	1.7	3.2	
	July 27, 1999	51387.457	−0.4	2.0		
	July 31, 1999	51391.441	0.2	1.8		
μ Peg	Sept. 6, 1998	51062.524	−11.3	3.2	3.5	
	Sept. 10, 1998	51067.452	−3.9	2.8		
	Sept. 14, 1998	51071.343	−3.4	2.8		
	Nov. 18, 2000	51866.323	−20.1	3.3	6.1	

2. OBSERVATIONS AND RESULTS

The observations were carried out with a modified Zeeman analyzer mounted at the Coudé focus of the 2.6-m Shain telescope of the Crimean Astrophysical Observatory. The detector and technique for determining the magnetic field are described in detail by Plachinda and Tarasova [33].

Almost all the stars were observed at 6200–6300 Å, except for ζ Hya, which was observed at 6149–6190 Å. The reciprocal dispersion was 3 Å/mm, and the resolution was 30 000. The signal-to-noise ratios were from 300 to 450. The spectra were preprocessed using the SPE code developed at the Crimean Astrophysical Observatory by S.G. Sergeev and V.V. Rumyantsev. Lines without blends deeper than 10% were chosen for the magnetic-field measurements. To this end, a synthetic spectrum was calculated for each star using the MERSEN code [34, 35] and the VALD database [36].

Table 1 presents the magnetic-field strengths acquired for the studied stars, along with values taken from other studies. We measured the surface-averaged longitudinal component of the field, or the general magnetic field as we call it by analogy with the Sun. Columns 1, 2, and 3 of Table 1 present the name of the star, the date of the observations, and the Julian date; columns 4, 5, and 6 present the strength of the magnetic field, the corresponding rms error, and the ratio of the field and its error, when this ratio is ≥ 3. We consider magnetic-field strengths exceeding their errors by more than a factor of three to be statistically significant. Column 6 presents references to other studies in which the magnetic fields for these giants were measured.

Statistically significant magnetic fields were obtained for 9 of the 15 studied giants, which have spectral types from G7 to M0. The magnitude of the fields of these stars did not exceed 20 G. One statistically significant value was recorded for each of the giants β And, η Psc, ζ Hya, ϵ Vir, and ζ Cyg. For δ And, κ Gem, ϵ Cyg, and μ Peg, statistically significant fields were detected twice. The measurements for δ And were separated by almost a year; both measurements are statistically significant and nearly the same (7.7 and 8.5 G). The measurements for κ Gem were separated by two years; as for δ And, both values are statistically significant and in good agreement (11.7 and 13 G). δ And displays signs of a hybrid giant. δ And and κ Gem belong to different groups, but have similar magnetic-field strengths.

For ϵ Cyg, two statistically significant values with opposite polarity were detected: +9.3 G and -8.7 G. The two measurements are separated by almost a year. We were able to make several measurements of the magnetic field of μ Peg; statistically significant values of the field are separated by more than two years. The values differ by a factor of two (−11.3 and −20.1 G) and have negative polarity. The observed field variations could be associated with rotation of the giants. Statistically significant magnetic fields were detected for ϵ Cyg on July 29, 1999, and for μ Peg on

Table 2. X-ray luminosity and $B-V$, M_v values specifying the giants' positions in the HR diagram

Object	HD	Spectral type	d, pc	$B-V$	M_v	$\log L_x$ [erg/s]	B_e, G
δ And	3627	K3III	31.1	1.28	0.81	28.5 [38]*	7.7, 8.5
β And	6860	M0III	61.1	1.58	−1.87		12.6
η Psc	9270	G7IIIa	90.2	0.97	−1.15		11.4
κ Gem	62345	G8IIIa	44.0	0.93	0.35	28.9 [38]*	11.7, 13.0
β Gem	62509	K0IIIb	10.3	1.00	1.06	27.6 [45]	
						27.7 [40]	
β Cnc	69267	K4III	89.0	1.48	−1.22		
ζ Hya	76294	G9II-III	46.2	1.00	−0.21	28.7 [47]*	−15.3
ϵ Vir	113226	G8IIIab	31.3	0.94	0.35	29.1 [45]	−10.8
						28.4 [40]	
α Boo	124897	K1.5III	11.3	1.23	−0.30	$<$25.8 [45]	
						$<$25.7 [40]	
ϵ BooA	129989	K0II-III	76.9	0.97	−1.70	28.9 [47]*	
α Ser	140573	K2IIIb	22.5	1.17	0.89	27.3 [45]	
						27.2 [40]	
η Her	150997	G7.5III	34.4	0.92	0.85	28.8 [45]	
ϵ Cyg	197989	K0III	22.1	1.03	0.74	$<$27.4 [40]	9.3, −8.7
						28.0 [47]*	
ζ Cyg	202109	G8II-III	46.3	0.99	−0.13	28.4 [47]*	5.4
μ Peg	216131	G8III	35.8	0.93	0.71	27.0 [45]	−11.3, −20.1
						26.7 [40]	

Note: Asterisks indicate that L_x was calculated from fluxes given in the studies noted.

September 6, 1998; however, no fields were detected on dates adjacent to these. We cannot explain this discrepancy. At the same time, we have no reason to doubt the reliability of the statistically significant values [33, 37].

β And is the only M star in our list. X-ray observations have indicated that there is a dividing line in the HR diagram, beyond which stars do not have coronas [18, 46]; these are giants later than K3. However, the recently completed catalog [38] includes 26 objects with $B-V \geq 1.3$ detected as X-ray sources. Moreover, Hunsch *et al.* [39] have presented evidence that some M giants may be X-ray sources. Only an upper limit to the X-ray flux of β And has been estimated: $\leq 5.3 \times 10^{-14}$ erg cm^{-2}s^{-1} [40]. We have one magnetic-field measurement for this giant, which is statistically significant and equal to 12.6 G. Borra *et al.* [31] did not detect the field of this star.

In addition to β And, the magnetic-field measurements of other authors are also available for β Gem, ϵ Vir, and α Boo. Table 1 shows that the accuracy of our measurements is close to that for the study of Borra *et al.* [31] and exceeds that of the study of Hubrig *et al.* [32]. No previous studies have detected significant magnetic fields for β Gem and α Boo. In spite of the fact that one of their measurements for α Boo exceeded the error by more than a factor of six, Borra *et al.* [31] claimed only a possible detection of the field in this star after a statistical analysis of the measurement errors. We are the only researchers to detect a statistically significant magnetic field for ϵ Vir. Other studies have not yielded any statistically significant values. This may be due to variations of the magnetic field with the phase of the rotational period; it is possible that other measurements have been carried out at times when the field was weak.

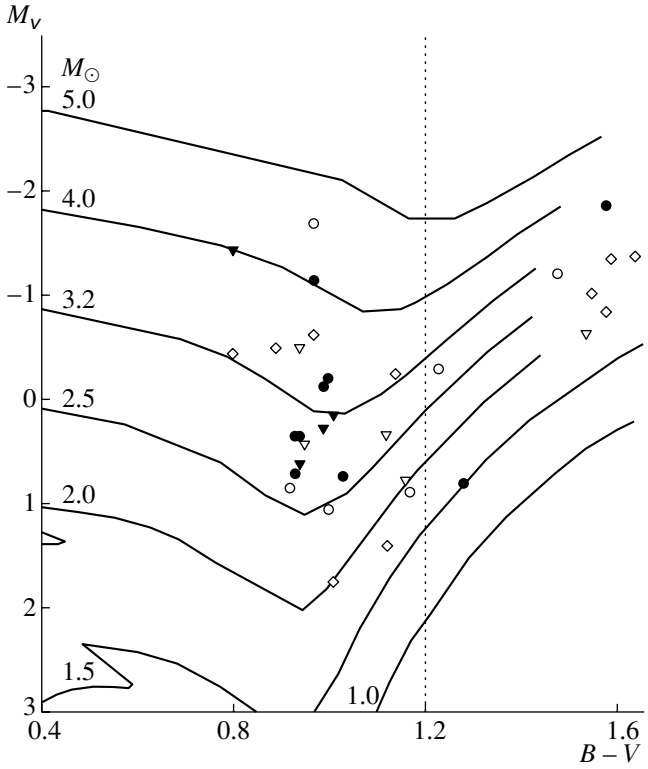

Positions of G–M giants in an evolutionary diagram. Circles denote giants whose magnetic fields were measured in the present study, triangles those measured by Hubrig *et al.* [32], and diamonds those measured by Borra *et al.* [31]. Filled symbols denote giants for which statistically significant magnetic fields were found. The dotted line indicates the position of the dividing line referred to in the text. The solid curves are evolutionary tracks for stars of the indicated masses.

3. DISCUSSION

We present measurements of the general magnetic fields of giants of spectral types from G7 to M0. Table 2 presents some parameters of the studied giants. Column 1 presents the name of the star, column 2 its HD number, column 3 its spectral type, and columns 4, 5, and 6 its distance in parsecs, $B-V$ color index, and absolute magnitude, respectively. As an estimate of the star's activity, column 7 presents the logarithm of its X-ray luminosity or an upper limit for this quantity; references to the studies from which the luminosities were taken are indicated. Asterisks denote studies from which we adopted fluxes and translated them into luminosities using the HIPPARCOS parallaxes; the distances presented in column 4 are those corresponding to these parallaxes. The last column of Table 2 contains the statistically significant magnetic-field values.

We can see from the last column of Table 2 that statistically significant magnetic fields were found for 9 of the 15 giants. This provides evidence for the existence of general magnetic fields in late-type giants.

In dynamo theory, the activity of late-type giants is determined by their magnetic fields. Almost all the giants for which statistically significant fields were found and for which X-ray luminosities were determined display a weak dependence between the field and X-ray luminosity. For κ Gem, ζ Hya, and ϵ Vir, the logarithm of the X-ray luminosity (in erg/s) exceeds that of the Sun at maximum activity and lies in the interval 28.7–29.1. The magnetic fields of these stars range from 10.8 to 15.3 G. In δ And, ϵ Cyg, and ζ Cyg, the logarithm of the X-ray luminosity is close to the solar value at maximum activity and lies in the range 28.0–28.5. The magnetic fields range from 5.4 to 9.3 G. It follows that the magnetic fields of the more active giants in our list do not significantly exceed those of less active giants.

The figure illustrates the general evolutionary status of the studied objects. The solid curves indicate evolutionary tracks based on the calculations of Claret [41]. These tracks were constructed using models with solar abundances for hydrogen, helium, and metals ($X = 0.8$, $Z = 0.02$). We used Kurucz's color tables for solar chemical composition to translate $T_{\rm eff}$ and $\log L$ into the observed $B-V$ and M_v values. We estimated the error of the translation of $T_{\rm eff}$ into $B-V$ using empirical values for $T_{\rm eff}$ [42]. The average difference between the empirical $B-V$ values and those calculated from Kurucz's tables was 0.03^m.

Since all the stars are within 100 pc, the interstellar absorption may be obtained in the same way as was done in [43]. The average value corresponding to the maximum correction is 0.05^m; for stars within 20 pc, this value is $< 0.02^m$.

The circles in the figure mark the positions of giants for which we derived magnetic-field measurements. The triangles present the positions of giants from the study of Hubrig *et al.* [32], and the diamonds, those from the study of Borra *et al.* [31]. The positions of all giants for which measurements were made in [32] and [33] are plotted in the HR diagram. Filled symbols denote the positions of giants for which statistically significant magnetic fields have been found.

The dotted line in the figure indicates the boundary dividing the region of giants for which EINSTEIN and ROSAT observations have detected X-ray emission from the region of giants with no X-ray detections [18, 19, 46]. We refer to this boundary as the dividing line, in accordance with the accepted nomenclature.

We can see from the figure that there are two giants on the red side of the dividing line for which statistically significant magnetic fields were detected that are comparable to those for giants located on the left of the line—δ And and β And. As in the case of the late-type dwarfs ξ Boo A and 61 Cyg A [37, 44], the statistically significant magnetic fields obtained for late-type giants could be a manifestation of their primordial magnetic field. In the theoretical model suggested in [28], when a star crosses the dividing line, the mechanism for the generation of the magnetic field changes. The action of the classical $(\alpha - \omega)$ dynamo that gives rise to large-scale, closed, loop-like magnetic field configurations ceases, and only small-scale magnetic fields formed by turbulent flows in the convective zone remain. Thus, if the dynamo mechanism produces the total magnetic field, the field structure should change when a star crosses the dividing line. If the general magnetic field is a manifestation of the primordial field, it should maintain its structure when the star crosses the dividing line. The fact that the M giant β And and the hybrid giant δ And are both on the red side of the dividing line in the HR diagram and have statistically significant magnetic fields may indicate that the measured magnetic fields are a manifestation of the primordial field of these stars. However, further studies are needed to reach final conclusions.

4. CONCLUSION

We have measured the surface-averaged longitudinal magnetic-field components (by analogy with the Sun, called the general magnetic fields) for 15 late-type giants with an accuracy of several gauss. Statistically significant fields were detected for nine of these stars. The magnetic fields of more active giants do not significantly exceed those of less active giants from our list. The magnetic-field values obtained suggest the existence of total magnetic fields in late-type giants.

The fact that the M giant β And and hybrid giant δ And display statistically significant magnetic fields may indicate that the measured fields are a manifestation of the primordial fields of the stars.

ACKNOWLEDGMENTS

The authors are grateful to R.E. Gershberg and S.I. Plachinda for useful comments, and to V.V. Tsymbal and C.R. Cowley for kindly presenting the code for the synthetic spectra calculations.

REFERENCES

1. R. D. Robinson, Astrophys. J. **239**, 961 (1980).
2. S. H. Saar, Astrophys. J. **324**, 441 (1988).
3. G. W. Marcy and G. S. Basri, Astrophys. J. **345**, 480 (1989).
4. G. Mathys and S. K. Solanki, Astron. Astrophys. **208**, 189 (1989).
5. G. S. Basri, G. W. Marcy, and J. A. Valenti, Astrophys. J. **390**, 622 (1992).
6. S. H. Saar and S. L. Baliunas, in *Proceedings of the 4th Solar Cycle Workshop "Solar Cycle,"* Ed. by K. L. Harvey (Astronomical Society of the Pacific, San Francisco, 1992), p. 197.
7. J. L. Linsky, C. Andrielis, S. H. Saar, *et al.*, in *Cool Stars, Stellar Systems, and the Sun,* Ed. by J.-P. Caillault (Astronomical Society of the Pacific, San Francisco, 1994), p. 438.
8. J. A. Valenti, G. W. Marcy, and G. S. Basri, Astrophys. J. **439**, 939 (1995).
9. I. Ruedi, S. K. Solanki, G. Mathys, and S. H. Saar, Astron. Astrophys. **318**, 429 (1997).
10. I. S. Savanov and Yu. Yu. Savel'eva, Astron. Zh. **74**, 919 (1997) [Astron. Rep. **41**, 821 (1997)].
11. C. M. Johns-Krull and J. A. Valenti, Astrophys. J. Lett. **459**, L95 (1996).
12. C. M. Johns-Krull, J. A. Valenti, A. P. Hatzes, and A. Kanaan, Astrophys. J. Lett. **510**, L41 (1999).
13. J.-F. Donati, M. Semel, B. D. Carter, *et al.*, Mon. Not. R. Astron. Soc. **291**, 658 (1997).
14. M. M. Katsova and A. G. Shcherbakov, Astron. Zh. **75**, 549 (1998) [Astron. Rep. **42**, 485 (1998)].
15. M. M. Katsova and A. G. Shcherbakov, Astron. Astrophys. **329**, 1080 (1998).
16. M. Hunsch and D. Reimers, Astron. Astrophys. **296**, 509 (1995).
17. V. Kashyap, R. Rosner, F. R. Harnden, *et al.*, Astrophys. J. **431**, 402 (1994).
18. T. R. Ayres, J. L. Linsky, G. S. Vaiana, *et al.*, Astrophys. J. **250**, 293 (1981).

19. B. M. Haisch, J. H. M. M. Schmitt, and C. Rosso, Astrophys. J. Lett. **383**, L15 (1991).
20. B. M. Haisch, J. H. M. M. Schmitt, and A. C. Fabian, Nature **360**, 239 (1992).
21. J. L. Linsky and B. M. Haisch, Astrophys. J. Lett. **229**, L27 (1979).
22. D. Reimers, Astron. Astrophys. **57**, 395 (1977).
23. L. Hartmann, A. K. Dupree, and J. C. Raymond, Astrophys. J. **246**, 193 (1981).
24. D. Reimers, Astron. Astrophys. **107**, 292 (1982).
25. D. J. Mullan and R. E. Stensel, Astrophys. J. **253**, 716 (1982).
26. T. Simon, J. L. Linsky, and R. E. Stensel, Astrophys. J. **257**, 225 (1982).
27. L. Hartmann, A. K. Dupree, and J. C. Raymond, Astrophys. J. Lett. **236**, L143 (1980).
28. R. Rosner, Z. E. Musielak, F. Cattaneo, *et al.*, Astrophys. J. Lett. **442**, L25 (1995).
29. J.-F. Donati, A. C. Cameron, G. A. J. Hussain, and M. Semel, Mon. Not. R. Astron. Soc. **302**, 437 (1999).
30. J.-F. Donati, Mon. Not. R. Astron. Soc. **302**, 457 (1999).
31. E. F. Borra, G. Edwards, and M. Mayor, Astrophys. J. **284**, 211 (1984).
32. S. Hubrig, S. I. Plachinda, M. Hunsch, and K. P. Schroder, Astron. Astrophys. **291**, 890 (1994).
33. S. I. Plachinda and T. N. Tarasova, Astrophys. J. **514**, 402 (1999).
34. C. R. Cowley, in *Model Atmospheres and Stellar Spectra,* Ed. by S. J. Adelman, F. Kupka, and W. W. Weiss (Astronomical Society of the Pacific, San Francisco, 1996), p. 170.
35. V. V. Tsymbal, private communication (1999).
36. F. Kupka, N. E. Piskunov, T. A. Ryabchikova, *et al.*, Astron. Astrophys., Suppl. Ser. **138**, 119 (1999).
37. S. I. Plachinda and T. N. Tarasova, Astrophys. J. **533**, 1016 (2000).
38. M. Hunsch, J. H. M. M. Schmitt, and W. Voges, Astron. Astrophys., Suppl. Ser. **127**, 251 (1998).
39. M. Hunsch, J. H. M. M. Schmitt, K. P. Schroder, and F. J. Zickgraf, Astron. Astrophys. **330**, 225 (1998).
40. M. Hunsch, J. H. M. M. Schmitt, K.-P. Schroder, and D. Reimers, Astron. Astrophys. **310**, 801 (1996).
41. A. Claret, Astron. Astrophys. **109**, 441 (1995).
42. G. V. Di Benedetto, Astron. Astrophys. **270**, 315 (1993).
43. G. V. Di Benedetto and Y. Rabbia, Astron. Astrophys. **188**, 114 (1987).
44. S. I. Plachinda, C. M. Johns-Krull, and T. N. Tarasova (in press).
45. K.-P. Schroder, M. Hunsch, and J. H. M. M. Schmitt, Astron. Astrophys. **335**, 591 (1998).
46. B. M. Haisch, J. H. M. M. Schmitt, and C. Rosso, Astrophys. J. Lett. **388**, L61 (1992).
47. A. Maggio, G. S. Vaina, B. M. Haisch, *et al.*, Astrophys. J. **348**, 253 (1990).

Translated by K. Maslennikov

Astronomy Reports, Vol. 46, No. 6, 2002, pp. 481–488. Translated from Astronomicheskiĭ Zhurnal, Vol. 79, No. 6, 2002, pp. 534–541.

The Possible Formation of Massive Tori in White-Dwarf Binary Systems

D. P. Savokhin and E. I. Staritsyn

Astronomical Observatory, Ural State University, Yekaterinburg, Russia

Received May 20, 2001; in final form, October 19, 2001

Abstract—Mass exchange in white-dwarf binary systems with mass ratios 0.35–0.55 and total masses exceeding the Chandrasekhar limit could lead to the disruption of the less massive component of the system and the formation of a torus around the more massive component. © *2002 MAIK "Nauka/Interperiodica".*

1. INTRODUCTION

The evolution of low- and moderate-mass stars ($0.8 \leq M/M_\odot \leq 10$) in close binary systems can lead to the formation of a pair of white dwarfs after the second stage of mass exchange [1–3]. The orbital period of such a pair will be much shorter than in the original system, due to the non-conservative nature of the mass exchange in the common-envelope stage. Fourteen white-dwarf pairs have already been discovered [4]. The observational characteristics of these systems can be derived in evolutionary computations for binary stars [5]. Most of the dwarfs in these pairs are helium stars with masses of 0.3–0.4 $M_\odot$. The conditions for the formation of binary white dwarfs and observational selection effects favor the detection of precisely such systems [4]. If the distance between the white dwarfs does not exceed $\sim 3R_\odot$, they can approach each other due to the loss of energy via the radiation of gravitational waves, and the less massive of the two will fill its inner critical surface on a time scale that is much less than the cosmological time scale [2, 3]. The detected binary white dwarfs include a number of systems with very short periods P: WD 2331 + 290, ($P \approx 4^{\rm h} - 4\overset{\rm h}{.}8$)[6]; WD 1704 + 481A, ($P = 3\overset{\rm h}{.}48$)[7]; PG 1101 + 364, ($P = 3\overset{\rm h}{.}47$)[8]; WD 0957 − 666 ($P = 1\overset{\rm h}{.}46$)[9]. The mutual approach of the dwarfs in these pairs will occur on time scales of less than 10^8–10^9 years. The total mass of the two white dwarfs does not exceed the Chandrasekhar limit. It is very likely that Roche-lobe filling and the flow of matter from these systems leads to the formation of isolated objects: helium subdwarfs or R Cor Bor stars [10].

The merging of two white dwarfs whose total mass exceeds the Chandrasekhar limit can lead to a type Ia supernova [2, 3]. One candidate type Ia supernova precursor has been identified, the binary system KPD 1930 + 2752, ($P = 2\overset{\rm h}{.}28$), made up of a helium subdwarf with a mass of $\approx 0.5M_\odot$ and a carbon–oxygen dwarf with a mass of $\approx M_\odot$ [11]. The components of KPD 1930 + 2752 will approach each other due to the radiation of gravitational waves over about 800 million years, and the system will become semidetached. By this time, the subdwarf will have evolved into a white dwarf [4]. If there is mass exchange in the binary white dwarf over the dynamical time scale, the less-massive dwarf will be completely disrupted. The matter from the disrupted white dwarf has some angular momentum; if this angular momentum is modest, the matter will immediately be added to the more massive component. If this angular momentum is sufficiently large, most of the matter from the less-massive dwarf may be concentrated in a torus around the more-massive dwarf. Subsequent accretion of the torus matter by the massive white dwarf is possible after the removal of some of the angular momentum from layers at the inner edge of the torus.

The total energy and angular momentum of the two white dwarfs when the less-massive dwarf fills its inner critical surface is insufficient to support a torus with the mass of the less-massive dwarf in equilibrium if the mass of the more-massive dwarf is 1 $M_\odot$ [12, 13]. Three-dimensional hydrodynamical computations indicate that mass exchange in binary white dwarfs with masses of 1.2 $M_\odot$ + 0.9 $M_\odot$ [14] and 0.9 $M_\odot$ + 0.6 $M_\odot$ [15] occur on the dynamical time scale. The less-massive dwarf is completely disrupted over a time exceeding about 2.2–2.5 periods of the binary system, before the onset of mass exchange. As a consequence of the collision of matter lost by the less massive dwarf with the surface of the more massive dwarf, a shock wave forms, in which the kinetic energy of the accreted matter is transformed into heat. As a result, a single axially symmetric object forms, in which the central degenerate core is surrounded by a carbon-burning shell, and the outer circumequatorial

1063-7729/02/4606-0481$22.00

layers are in a state of rapid rotation [14–17]. The total energy and angular momentum of the system are conserved within the computational accuracy. The mass of ejected matter cannot exceed 0.3% [14]. The disruption of a white dwarf in a binary with a low-mass black hole leads to the formation of a torus, with the angular momentum of the white dwarf stored in the torus matter [18].

In the current study, we have constructed stationary models for a self-gravitating torus in the gravitational field of a nonrotating dwarf. By comparing the total energies and angular momenta of the dwarf–torus system and of semidetached dwarf binaries with component masses equal to those of the central star and torus, we can identify dwarf pairs for which the possible formation of a torus from the matter of the less massive component is not excluded by the conservation laws.

2. METHOD FOR COMPUTING THE STRUCTURE OF THE SELF-GRAVITATING TORUS

Stationary, axially symmetrical models for differentially rotating tori with masses characteristic of white dwarfs were constructed taking into account the gravitational fields of both the torus itself and of the white dwarf at the center of the configuration. The equation of motion of an element of the torus volume has the form

$$\rho(\mathbf{v}\nabla)\mathbf{v} + \nabla P + \rho\nabla\Phi = 0,$$

where ρ is the density of the matter. The pressure of the matter $P(\rho)$ is related to the density by the equation of state for a degenerate electron gas [19]:

$$\begin{cases} P(x) = a\{x(1+x^2)^{1/2}(2x^2/3-1) + \ln(x+(1+x^2)^{1/2})\}/8\pi^2 \\ \rho(x) = bx^3, \end{cases}$$
$$a = m_e c^2/\lambda_e^3, \quad b = m_H/(3\pi^2\lambda_e^3 Y_e), \quad x = p_F/(m_e c),$$

where m_e and m_H are the electron mass and the atomic mass unit, respectively; λ_e is the Compton wavelength of the electron; c is the speed of light; p_F is the Fermi momentum of the degenerate electron gas; and $1/Y_e = \mu_e$ is the molecular weight of the gas. In the case of a barotropic equation of state, the surfaces of constant pressure and constant density coincide and the angular velocity of rotation $\Omega(\varpi)$ is a function only of the distance from the rotational axis ϖ [20]. The linear velocity of a matter element is related to the angular velocity by the expression

$$\mathbf{v} = \varpi\Omega(\varpi)\mathbf{e}_\varphi,$$

where $\mathbf{e}_\varphi$ is a unit vector in the direction of the azimuthal angle φ.

Integrating the equation of motion, we can obtain the Bernoulli integral

$$H(\rho) + \Phi + \Psi(\varpi) = C, \qquad (1)$$

where C is the constant of integration; $H(\rho)$ is the enthalpy, given by the expression

$$H(\rho) = \int dP(\rho)/\rho;$$

and $\Psi(\varpi)$ is the centrifugal potential, which is related to the angular velocity by the expression

$$\Psi(\varpi) = -\int \Omega^2(\varpi)\varpi d\varpi.$$

The angular velocity of the near-equatorial regions of the product of a merger of two white dwarfs with masses 0.9 $M_\odot$ and 0.6 $M_\odot$ falls off with distance from the rotational axis in approximately the same way as for Kepler's third law [15]. Here, we have computed torus models for cases when the decrease in the angular velocity with distance from the rotational axis has precisely the form

$$\Psi(\varpi) = C_\Psi/\varpi \qquad (2a)$$

or is more gradual

$$\Psi(\varpi) = -C_\Psi \ln(\varpi). \qquad (2b)$$

The gravitational potential Φ is determined by the matter of both the torus and the central white dwarf:

$$\Phi = \Phi_t + \Phi_d. \qquad (3)$$

The gravitational potential of the torus satisfies the Poisson equation

$$\triangle^2\Phi_t = 4\pi G\rho. \qquad (4)$$

We do not take into account the effect of the torus on the structure of the white dwarf. The potential of the white dwarf Φ_d is assumed to be spherically symmetrical and completely determined by the specified mass M_d.

After expressing the density from the Bernoulli integral (1) as an inverse function of the enthalpy

and substituting this and Eqs. (2) and (3) into (4), we obtain an equation in the gravitational potential of the torus Φ_t, the constant C, and C_Ψ. Specifying the maximum density of the torus matter, the ratio of the inner and outer radii of the torus in the equatorial plane, and the boundary conditions for the field [21, 22], we can find a simultaneous solution for the constant C, C_Ψ, and the field Φ_t. Further, we calculate from (1) the distribution of the density of the torus matter and its mass M_t, angular momentum J_t, and gravitational W_t, kinetic T_t, and internal U_t energies. We monitored the accuracy of the computations using a virial test [23]:

$$VT = \mid 2T_t + W_t + 3\Pi \mid / \mid W_t \mid,$$

where Π is given by the expression

$$\Pi = \int P d\mathbf{r}$$

and $d\mathbf{r}$ is a volume element. For all the computed models, $VT \approx 10^{-4}$–10^{-5}.

The method described [24, 22] was applied earlier to compute models of rapidly rotating neutron stars and white dwarfs [25, 26].

The radial distributions Φ_t, Φ and the effective potential $\Phi + \Psi$ in the equatorial plane for a system with a white dwarf and torus with masses of $M_d = 1.2\ M_\odot$ and $M_t = 0.5 M_\odot$ are shown in Fig. 1. The rotation of the torus is specified by formula (2a).

3. MODELS OF SELF-GRAVITATING TORI IN THE GRAVITATIONAL FIELD OF A CENTRAL STAR

The angular momentum of the torus is determined by its mass, the position of its inner edge, and the rotation curve and mass of the central white dwarf. For fixed masses of the torus and white dwarf, the angular momentum of the torus decreases as its inner edge approaches the white-dwarf surface (Fig. 2). If the torus rotation curve is given by (2a), the minimum radius of its inner edge corresponds to contact of the torus with the white-dwarf surface. When the torus rotation is given by (2b), the effective gravitational acceleration (the sum of the gravitational and centrifugal accelerations) at its inner edge vanishes when this edge is some distance from the white-dwarf surface. The radius of the inner edge of a stationary torus must exceed this distance. At smaller distances, stationary models of tori whose rotation is given by (2b) cannot exist. The angular momenta of tori rotating in accordance with (2b) is higher than those rotating in accordance with (2a). These values exceed the orbital angular momenta of the corresponding binary white dwarfs with component masses M_d and M_t when the dwarf with mass M_t fills its Roche lobe.

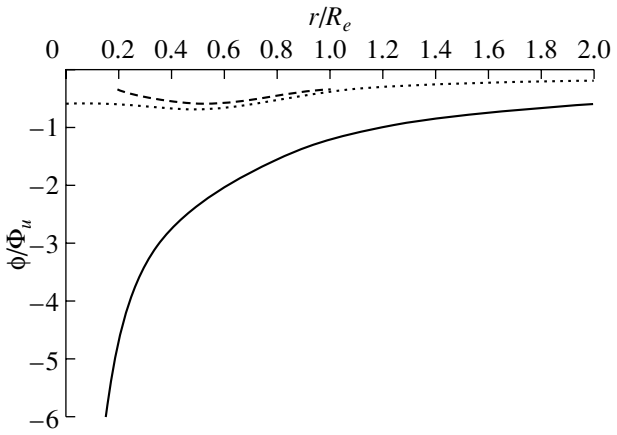

Fig. 1. Radial distribution of the potential ϕ in the equatorial plane (in relative units Φ_u). R_e is the radius of the outer edge of the torus. The dotted curve shows the gravitational potential of the torus ($\phi = \Phi_t$), the solid curve the sum of the gravitational potentials of the center of the white dwarf and the torus ($\phi = \Phi_d + \Phi_t$), and the dashed curve the sum of this gravitational potential and the centrifugal potential of the torus ($\phi = \Phi_d + \Phi_t + \Psi$).

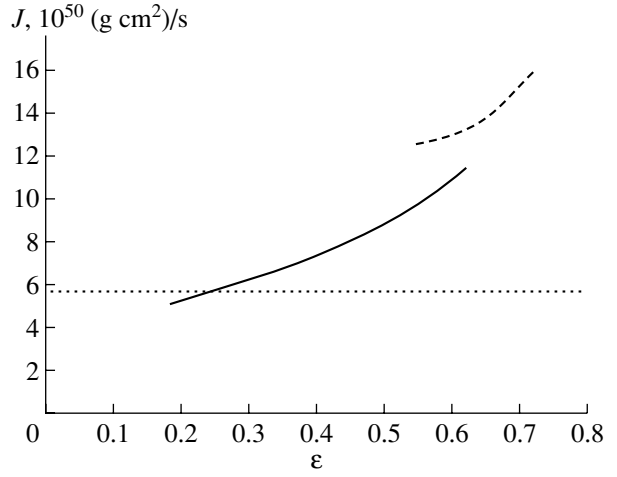

Fig. 2. Angular momentum of the torus J as a function of the ratio ε of the radii of the inner and outer edges of the torus in the equatorial plane for the rotation laws (2a), shown by the solid curve, and (2b), shown by the dashed curve. The masses of the torus and white dwarf are 0.5 $M_\odot$ and 1 $M_\odot$. The left boundaries of the curves correspond to contact between the inner edge of the torus and the white-dwarf surface (solid curve) and the vanishing of the effective gravitational acceleration at the inner edge of the torus (dashed curve). The dotted line shows the orbital angular momentum of a semidetached system with two white dwarfs with masses 0.5 $M_\odot$ + 1 $M_\odot$.

The formation of a stationary torus from the matter of the less massive component of the binary is not possible if the angular velocity of rotation of the torus falls off with distance from the rotational axis more slowly than a Kepler law. The angular momentum of

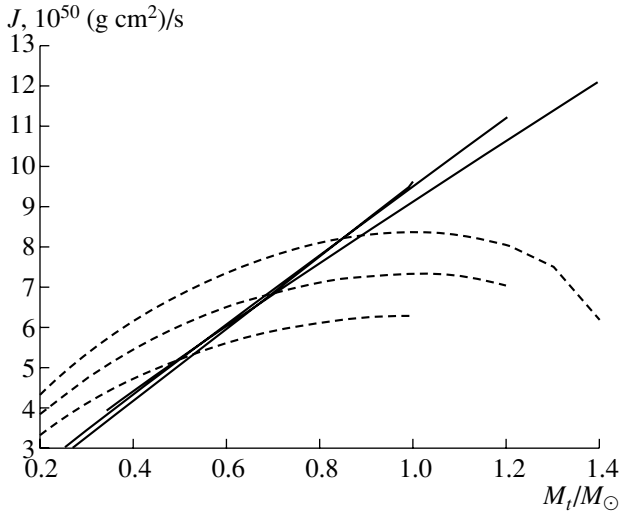

Fig. 3. Angular momentum J of a white dwarf–torus system as a function of the torus mass M_t for the three white-dwarf masses $M_d/M_\odot$ =1; 1.2; 1.4 (solid lines). The dashed curves show the angular momenta J of semidetached systems with two white dwarfs as a function of the mass of the secondary M_t for the same three masses of the primary M_d. The right boundaries of all the curves correspond to the case $M_t = M_d$.

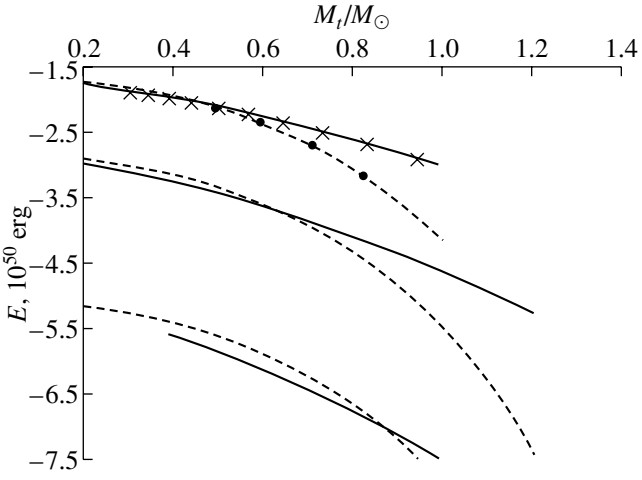

Fig. 4. Energies E of a system of a white dwarf and torus with masses M_d and M_t (solid curves) and of a semidetached system of two white dwarfs with masses M_d and M_t (dashed curves) as a function of M_t. The upper pair of curves corresponds to $M_d = 1\ M_\odot$, the middle pair to $M_d = 1.2M_\odot$, and the lower pair to $M_d = 1.4\ M_\odot$. The circles and x's show the results of [12, 13], respectively.

a torus rotating in accordance with (2a) is lower than the orbital angular momentum of the corresponding binary system if the inner edge of the torus is sufficiently close to the white-dwarf surface (Fig. 2). A similar result is obtained when the angular velocity of rotation of the torus falls off with distance from the rotational axis more rapidly than the Kepler law [12, 13].

Figures 3 and 4 show the angular momentum of the torus and total energy of the white dwarf–torus system in the case of contact as a function of the torus mass for the three fixed white-dwarf masses $M_d/M_\odot = \{1.0; 1.2; 1.4\}$. The gravitational and internal energies of the white dwarf were estimated neglecting the influence of the torus on the structure of the dwarf. The rotation of the torus was specified by (2a). These same figures show the dependences of the angular momentum and total energy of a semidetached binary white-dwarf system on the mass of the less massive component for the same fixed masses for the more massive dwarf M_d. As in [12], the total energy of the white dwarf–torus system with $M_d = 1\ M_\odot$ and $M_t \geq 0.5\ M_\odot$ is higher than that for a semidetached system with white dwarfs with the same masses M_d and M_t. However, for each mass M_d, we can indicate a mass $M_t^{\rm up}$ such that the total energy and angular momentum of a semidetached binary system for which $M_t \leq M_t^{\rm up}(M_d)$ will be lower than those of the corresponding white dwarf–torus system. The dependence $M_t^{\rm up}(M_d)$ is shown in Fig. 5.

Three-dimensional hydrodynamical computations of flows of matter in binary white-dwarfs demonstrate a decrease in the orbital momentum due to the formation of a disk [14, 18]. The total angular momentum of the disk and binary is conserved. As a result, the distance between the components grows less than when the angular momentum of the binary system alone is conserved, or even remains unchanged. The storage of momentum in the forming disk promotes instability in the mass exchange in the binary white dwarf and the disruption of the less massive component on the dynamical time scale. Figure 5 shows the minimum mass $M_t^{\rm low}$ for which the mass exchange can still proceed over the dynamical time scale as a function of M_d, in accordance with [14]. Tidal interactions are not able to transfer the angular momentum of the forming disk to the binary, due to the short time scale for the transfer of matter and disruption of the less massive dwarf in systems with $M_t^{\rm low}(M_d) < M_t$.

The region of binary white-dwarf parameters for which we expect disruption of the less massive component and the formation of a torus around the more massive component is bounded from above by the requirement that the angular momentum and total energy of the binary system exceed those of the corresponding white dwarf–torus system, and from below by the requirement that there be mass exchange on the dynamical time scale (Fig. 5). This region is bounded on the right by the Chandrasekhar limit for the mass of the more massive dwarf in the binary

system. The total mass of nearly all pairs of white dwarfs exceeds the Chandrasekhar limit.

4. THE POSSIBLE FORMATION OF PRECURSORS TO TYPE Ia SUPERNOVAE

The region of component masses for binary white dwarfs whose total mass exceeds the Chandrasekhar limit can be divided into four subregions (Fig. 5).

Subreqion A contains binary dwarfs with similar masses. If the mass of each dwarf exceeds $\approx 1.2\ M_\odot$ and the mass exchange is not conservative in the common-envelope stage, the formation of a single object with a mass exceeding the Chandrasekhar limit and a central density of $\approx 10^{10}$ g/cm^3 is possible [12]. White dwarfs with masses exceeding 1.1–1.2 $M_\odot$ are made up of a mixture of oxygen and neon [3]. Neutronization of the matter in the neon cores is likely to stimulate the collapse of the product of a merger of two such dwarfs. However, according to the three-dimensional hydrodynamical computations of [14], common envelopes are not able to form in systems with component mass ratios that are not very different from unity. The mass of the binary system should be conserved in the merger of the components. In this case, rapidly rotating, very elongated white dwarfs are formed. The density in these dwarfs does not exceed $\approx 2 \times 10^8$ g/cm^3 [26]. Their further evolution may be accompanied by a transfer of angular momentum from the inner regions, followed by an increase in the density and possibly a loss of matter and angular momentum from the circumequatorial region. When the density in the product of a merger of carbon–oxygen dwarfs reaches $\approx 10^{10}$ g/cm^3, a nuclear explosion and the formation of a type Ia supernova is possible.

Subregion B contains pairs in which the matter lost by the less massive dwarf is heated when it collides with the surface of the more massive dwarf. The structure of the single object that forms was derived in the three-dimensional hydrodynamical computations of matter flows in such pairs of dwarfs, carried out in [14, 15]. The matter is heated sufficiently for the thermonuclear burning of carbon to occur [14–17]. The subsequent evolution of the single object that forms is determined by the total mass of the initial pair of dwarfs and the relationship between the rate of thermonuclear burning in the carbon-burning shell and the rate of mass loss via the stellar wind. The carbon burning propagates inward as a consequence of the thermal conductivity of the matter, reprocessing the carbon–oxygen mixture into a mixture of oxygen, neon, and magnesium [27]. The density in the central region grows as angular momentum is transported outward. The subsequent neutronization in the neon and magnesium cores stimulates the collapse of the merger product [15, 27]. If the mass of the merger product becomes lower than the Chandresekhar limit as a consequence of mass loss via the stellar wind, the final result of its evolution will be a hot, rapidly rotating white dwarf [15]. The boundary between subregions A and B (Fig. 5) has been drawn arbitrarily, and corresponds to pairs of dwarfs for which the difference in their surface potentials is sufficient to heat the accreted matter to 8×10^8 K.

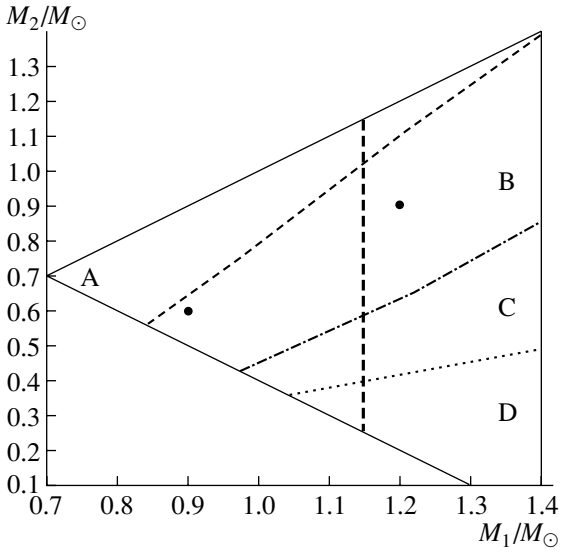

Fig. 5. Subregions A, B, C, and D in the plane of the masses M_1 and M_2 of the primary and secondary components of a degenerate-dwarf binary system. The upper solid line corresponds to $M_1 = M_2$, the lower solid line to $M_1 + M_2 = 1.4\ M_\odot$, and the vertical solid line to $M_1 = 1.4\ M_\odot$. The dashed line shows the case of a dwarf pair in which the difference in the surface potentials is sufficient to heat matter to a temperature of 8×10^8 K, the dot–dashed line the dependence $M_t^{\rm up}(M_1)$, and the dotted line the dependence $M_t^{\rm low}(M_1)$. The vertical dashed line marks the boundary between carbon–oxygen and oxygen–neon dwarfs. The circles represent binary systems for which the dynamics of the disruption of the less massive component were computed in [14] (right) and [15] (left).

Subregion C contains pairs of dwarfs for which the orbital angular momentum and total energy are sufficient to support the equilibrium of a torus with the mass of the less massive dwarf forming at some distance from the more massive dwarf. Ballistic estimates indicate that the specific angular momentum of the matter at the inner Lagrangian point at the onset of the mass exchange in such pairs is sufficient for an element of matter to pass around the more massive component, even taking into account the pull of the less massive component. This suggests that, with the onset of mass exchange, a disk begins to form around the massive component. The storage

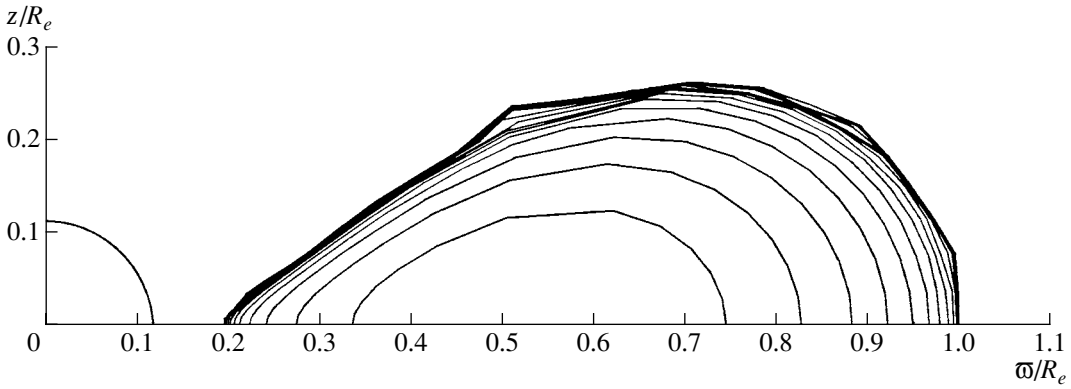

Fig. 6. Contours of constant density for a model torus with mass 0.5 $M_\odot$ rotating in accordance with (2a) in the gravitational field of a white dwarf with mass 1.2 $M_\odot$. The densities of neighboring lines differ by a factor of two. The circle shows the position of the white-dwarf surface.

of angular momentum in the disk could lead to the disruption of the less massive component over the dynamical time scale [14, 18]. The formation of a torus from the matter of the less massive dwarf must be confirmed by hydrodynamical computations.

Figure 6 shows an example of such a torus with mass $M_t = 0.5\ M_\odot$. The maximum density in the torus is 9.04×10^4 g/cm^3. The mass of the white dwarf is $M_d = 1.2\ M_\odot$. The total energy and angular momentum in this white dwarf–torus system are 0.1 and 9% lower than the corresponding values for a semidetached system with white dwarfs with masses 0.5 $M_\odot$ and 1.2 $M_\odot$.

To determine the distance between the components of a semidetached white-dwarf binary, we used a standard model with two point masses, assuming that the rotation of the components is synchronized with their orbital motion. Given the finite dimensions of the components, the distance between the components of close binary systems when the inner Roche lobe is filled will be greater [29]. The increase in this distance over that for the point-mass model is $\approx 4\%$ for two neutron stars with the same mass [29]. During the approach of the pair of white dwarfs due to the radiation of gravitational waves, the frequency of the orbital motion increases. If a corresponding unwinding of the dwarf pair does not take place, the frequency of their own rotations will become less than the orbital frequency. In this case, the distance between the components of the semidetached system will be less than for the case of their synchronized rotation [30]. The maximum decrease in this distance is $\approx 6\%$ for a wide range of component mass ratios and corresponds to the absence of rotation of the two stars [30]. The total action of these effects, which partially compensate each other, amounts to only a slight change in the distance between the components, and consequently to a small change in the estimated interaction energy for the pair. Since the mass ratios in the considered pairs differ appreciably from unity, the contribution of the interaction energy to the total energy of the binary does not dominate. Thus, effects due to the extent of the binary components and their possible nonsynchronous rotation only weakly influence the position of the boundary $M_t^{\rm up}$ separating subregions B and C in Fig. 5. The subsequent evolution of the dwarf–torus system is linked to the accretion of the torus matter by the white dwarf and is determined by the mechanism for transporting angular momentum outward from the inner layers of the torus. The longest torus lifetime is achieved when the angular momentum is carried outward due to the viscosity of the degenerate electron gas, and is $\approx 10^9$ yr [17]. If the torus matter is subject to shear turbulence, the transfer of angular momentum is much more rapid, and the lifetime of the torus may be shortened to ≈ 10 days [17]. In this case, an important role in the subsequent evolution of the dwarf–torus system is played by processes heating matter via accretion and the dissipation of turbulent energy. The chemical composition of the initial white dwarfs is no less important. The accretion of torus matter by carbon–oxygen dwarfs provides another opportunity for the formation of type Ia supernova precursors. The gravitational-potential difference between the inner edge of the torus and the surface of the white dwarf, shown in Fig. 6, is insufficient to heat the matter to the temperatures required for carbon burning. If the less massive component was a helium or hybrid dwarf, the accretion of the torus matter leads to the formation of a helium-burning shell at the surface of the carbon–oxygen dwarf. This could lead to the formation of an R Cor Bor star, as has been proposed for the case of mass exchange in binaries consisting of a carbon–oxygen and helium dwarf [2]. If the more massive component were an oxygen–neon

dwarf, the evolution of the merger product would end in the collapse of the central region. Final conclusions about the final evolution of such white-dwarf pairs require both hydrodynamical computations of mass exchange in the pairs and studies of the torus stability, processes transporting angular momentum in the torus, the stability and rate of mass-loss by the torus, and so on.

Subregion D (Fig. 5) contains pairs consisting of an oxygen–neon and a helium dwarf. The mass exchange in these pairs occurs on the time scale for the loss of energy via gravitational radiation. The boundary between subregions C and D nearly coincides with the lower limit for the mass of carbon–oxygen and hybrid dwarfs [3].

5. CONCLUSION

The orbital angular momentum and total energy of a semidetached dwarf binary with the mass of the more massive component $M_d > 1\ M_\odot$ and the mass ratio M_t/M_d not exceeding 0.5–0.6 are sufficient to maintain the equilibrium of a stationary, self-gravitating torus with mass M_t in the gravitational field of a white dwarf with mass M_d. The angular velocity of rotation in such tori must decrease with distance from the rotational axis in accordance with or more rapidly than the Kepler law. The relatively small torus mass (30–60% of the mass of the central star) justifies the assumption of spherical symmetry for the gravitational field at the center of the star. Indeed, three-dimensional hydrodynamical computations of the disruption of white dwarfs in systems with component mass ratios of 0.75 [14] and 0.66 [15] show that the more massive dwarf is essentially undeformed by tidal forces.

The disruption of the less massive dwarf and formation of a torus can occur on the dynamical time scale in close pairs of white dwarfs with component mass ratios no lower than 0.3–0.4 [14]. The storage of angular momentum in a disk forming around the massive dwarf in the final stages of mass exchange decreases the angular momentum of the orbital motion of the binary components and is the main reason for the disruption of the less massive dwarf on the dynamical time scale [14, 18]. The possible formation of a torus from the less massive dwarf must be confirmed by dynamical computations.

Population-synthesis studies [4, 5] indicate that pairs of white dwarfs with similar masses should comprise a large fraction of binary white dwarfs. Precursors of type Ia supernova most likely form as the result of mergers of carbon–oxygen dwarfs in such pairs. Some type Ia precursors may form from systems of carbon–oxygen dwarfs with mass ratios of 0.35–0.55. The type Ia precursor candidate binary system KPD 1930 + 2752 has a mass ratio of ≈ 0.5 [11]. The merging of components in such pairs may be accompanied by the formation of a torus from the matter of the less massive dwarf. The gravitational potential difference between the inner edge of the torus and the white-dwarf surface is not sufficient to heat matter to the temperatures required for the thermonuclear burning of carbon. The subsequent evolution of the white dwarf–torus system requires a whole series of further studies.

ACKNOWLEDGMENTS

The author thanks S.I. Blinnikov, who provided the method and code for computing the structures of single rapidly rotating stars [24, 22].

REFERENCES

1. A. V. Tutukov and L. R. Yungelson, Acta Astron. **29**, 665 (1979).
2. I. Iben and A. V. Tutukov, Astrophys. J. **282**, 615 (1984).
3. A. G. Masevich and A. V. Tutukov, *Evolution of Stars: Theory and Observations* [in Russian] (Nauka, Moscow, 1988).
4. G. Nelemans, L. R. Yungelson, S. F. Portegis Zwart, and F. Verbunt, Astron. Astrophys. **365**, 491 (2001).
5. G. Nelemans, F. Verbunt, L. R. Yungelson, and S. F. Portegis Zwart, Astron. Astrophys. **360**, 1011 (2000).
6. T. R. Marsh, V. S. Dhillon, and S. R. Duck, Mon. Not. R. Astron. Soc. **275**, 828 (1995).
7. P. Maxted, T. R. Marsh, C. Moran, and Z. Han, Mon. Not. R. Astron. Soc. **314**, 334 (2000).
8. T. R. Marsh, Mon. Not. R. Astron. Soc. **275**, L1 (1995).
9. C. Moran, T. R. Marsh, and A. Bragaglia, Mon. Not. R. Astron. Soc. **288**, 538 (1997).
10. I. Iben, A. V. Tutukov, and L. R. Yungelson, Astrophys. J. **475**, 291 (1997).
11. P. Maxted, T. R. Marsh, and R. C. North, Mon. Not. R. Astron. Soc. **317**, L41 (2000).
12. I. Hachisu, Y. Eriguchi, and K. Nomoto, Astrophys. J. **308**, 161 (1986).
13. I. Hachisu, Y. Eriguchi, and K. Nomoto, Astrophys. J. **311**, 214 (1986).
14. W. Benz, R. L. Bowers, A. G. Cameron, and W. H. Press, Astrophys. J. **348**, 647 (1990).
15. L. Segretain, G. Chabrier, and R. Mochkovitch, Astrophys. J. **481**, 355 (1997).
16. R. Mochkovitch and M. Livio, Astron. Astrophys. **209**, 111 (1989).
17. R. Mochkovitch and M. Livio, Astron. Astrophys. **236**, 378 (1990).
18. C. L. Frier, S. E. Woosley, M. Herant, and M. B. Davies, Astrophys. J. **520**, 650 (1999).

19. S. L. Shapiro and S. A. Teukolsky, *Black Holes, White Dwarfs, and Neutron Stars: the Physics of Compact Objects* (Wiley, New York, 1983; Mir, Moscow, 1985), Vol. 1.
20. J.-L. Tassoul, *Theory of Rotating Stars* (Princeton Univ. Press, Princeton, 1979; Mir, Moscow, 1982).
21. M. J. Clement, Astrophys. J. **194**, 709 (1974).
22. A. G. Aksenov and S. I. Blinnikov, Astron. Astrophys. **290**, 674 (1994).
23. J. P. Ostriker and P. Bodenheimer, Astrophys. J. **151**, 1089 (1968).
24. O. S. Bartunov and S. I. Blinnikov, Astron. Astrophys. **273**, 106 (1993).
25. A. G. Aksenov, S. I. Blinnikov, and V. S. Imshennik, Astron. Zh. **72**, 717 (1995) [Astron. Rep. **39**, 638 (1995)].
26. D. P. Savokhin, E. I. Staritsin, and S. I. Blinnikov, Astron. Zh. **78**, 798 (2001) [Astron. Rep. **45**, 692 (2001)].
27. H. Saio and K. Nomoto, Astrophys. J. **500**, 388 (1998).
28. K. Nomoto, in *Problems of Collapse and Numerical Relativity,* Ed. by D. Bancel and M. Signore (Reidel, Dordrecht, 1984), p. 89.
29. O. A. Kuznetsov, M. E. Prokhorov, M. V. Sazhin, and V. M. Chechetkin, Astron. Zh. **75**, 725 (1998) [Astron. Rep. **42**, 638 (1998)].
30. D. V. Bisikalo, A. A. Boyarchuk, O. A. Kuznetsov, and V. M. Chechetkin, Astron. Zh. **76**, 270 (1999) [Astron. Rep. **43**, 229 (1999)].

Translated by D. Gabuzda

Astronomy Reports, Vol. 46, No. 6, 2002, pp. 489–496. Translated from Astronomicheskiĭ Zhurnal, Vol. 79, No. 6, 2002, pp. 542–550.

Variability of the Photospheric Radiation of Active K–M Dwarfs and Their X-ray Luminosities

N. I. Bondar'

Crimean Astrophysical Observatory, p/o Nauchnyĭ, Crimea, 334413 Ukraine

Received April 20, 2001; in final form, November 23, 2001

Abstract—Variability of the photospheric radiation of 40 (dKe–dMe) dwarfs in the solar neighborhood due to variations in the spottedness of their surfaces is analyzed based on the behavior of their mean annual brightnesses over long time intervals. The amplitudes and characteristic time scales of the variations of the mean annual brightness are taken to be indicators of photospheric activity and were used to infer the levels of photospheric activity in the stars studied. The influence of axial rotation on the development of cyclic activity in young red dwarfs and F–M main-sequence stars is analyzed. The durations and amplitudes of the photospheric variability of rapidly rotating (dK0e–dK5e) stars testifies to a higher level of photospheric activity among red dwarfs and solar-type stars. The X-ray luminosities of these stars grow with the amplitude of the variations of the mean annual brightness. However, this is not typical of rapidly rotating M dwarfs, for which the X-ray emission varies by more than two orders of magnitude, although their degrees of spottedness are all virtually the same. A linear relationship between the X-ray and bolometric luminosities is observed for young (dKe–dMe) stars, with their ratios $\log(L_x/L_{bol})$ being about -3. These properties can be used to determine whether a red dwarf is a young star or is already on the main sequence.

1. INTRODUCTION

The magnetic activity of stars is accompanied by a number of phenomena that arise as a consequence of variations in the physical conditions in local regions, which further develop in time throughout all layers in the atmosphere. Such regions form due to the emergence of magnetic fields at the stellar surface. In the end, magnetic activity leads to the dynamical reconstruction of the outer atmosphere of the star [1].

According to models for the generation of magnetic fields in stars with convective envelopes, the intensity of active processes depends on the star's age, the rate of its axial rotation, and the depth of its convective zone [2, 3]. Systematic observations of indicators of activity that are sensitive to variations of the magnetic field carried out over a wide range of wavelengths have confirmed this picture. Slow variations of mean annual activity indices have been detected for various types of stars; these can have a cyclic or irregular character or be manifest in the form of trends [4–6]. The activity cycles of some stars have durations comparable to that of the Sun, while others are appreciably shorter or longer. These data and detailed studies of the relationship between the physical characteristics of F–M dwarfs and activity indicators associated with various atmospheric layers lead to the conclusion that the magnetic activity of the Sun and solar-type stars is produced by the same set of processes, but other mechanisms come into action in the transition to other types of stars [7–12].

In red dwarfs, this is brought about by rapid rotation and the formation of a fully convective envelope in stars later than M5. In contrast to solar-type stars, their activity cycles can have durations of decades. Data on the cyclic activity of several spotted red dwarfs have been obtained from studies of their light curves over long time intervals [13–16], and flare phenomena [17, 18] and X-ray variability [19] have been detected and studied for individual stars. However, the development of cyclic phenomena in the atmospheres of late dwarfs remains poorly studied.

Our investigations are directed toward a search for activity cycles in (dKe–dMe) stars included in the catalog by Gershberg *et al.* [20], which contains 463 objects. Here, we analyze the behavior of the mean annual brightness of 40 K–M dwarfs on time intervals from several years to several decades, published in [21–23]. We compare the variability of the mean annual brightness (its amplitude and characteristic time scale) with the periods of axial rotation of the stars P_{rot} and their bolometic and X-ray luminosities L_{bol} and L_x, taken from [6, 20, 24].

Based on these analyses, we investigate differences in the activity levels of K and M dwarfs and compare these results with the activity of solar-type

1063-7729/02/4606-0489$22.00

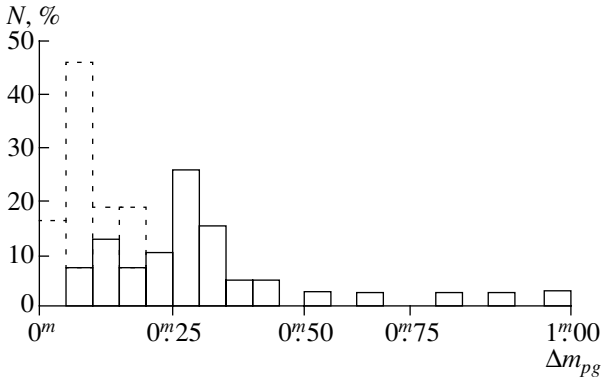

Fig. 1. Histogram of variations in the mean annual brightnesses Δm_{pg} for 40 (dKe–dMe) stars and their control stars (dashed lines).

stars. We also consider the influence of surface spottedness on K and M dwarfs on their coronal X-ray emission.

2. LONG-TERM BRIGHTNESS VARIATIONS IN 40 (dKe–dMe) STARS

Variability in the intensity of processes forming spots on the surfaces of red dwarfs lead to slow variations of their mean brightness, which become appreciable over time scales of several years. Similar to the mean annual Wolf number, the amplitude of these variations can be used as an index of photospheric activity.

We investigated the behavior of the mean annual brightnesses of 40 active red dwarfs using photographic plates in the collections of the Sternberg Astronomical Institute, the Odessa Astronomical Observatory, and the Sonneberg Observatory. We also used photoelectric data taken from the literature or obtained on the 125-cm telescope of the Crimean Astrophysical Observatory [25, 26]. We chose the stars for our study from the catalog of UV Ceti stars and related objects [20], taking into account the contents of the photographic plates in the collections indicated above.

The program list (Table 1) includes stars of various brightnesses with M_v in the range from 6^m to 15^m. Eight of the dwarfs have spectral types K1–K8.5, and 28 have spectral types M0–M7; four do not have accurately determined spectral types but have been identified as flaring red dwarfs based on photometric data. We also studied the brightness of a control star with similar brightness and spectral type near each program star. The mean annual magnitudes of the control stars showed comparable dispersions, with a mean weighted rms error of $\sigma = 0^m.05$. The weights were determined by the number of points in the light curves constructed using the mean annual values. For all the control stars, the variations of these values $\Delta m_{pg} = m_{\max} - m_{\min}$ did not exceed $0^m.2$, which corresponds to 4σ. Consequently, their brightnesses remained constant in the time intervals studied at the $\alpha = 0.05$ confidence level. The absence of variability in the control stars is confirmed by the distribution of their Δm_{pg} values, indicated by the dashed lines in the histogram in Fig. 1. The values of Δm_{pg} for the program stars are presented in Table 2, and their distribution is indicated by the solid lines in the histogram in Fig. 1.

Eight stars display clear variability in their mean annual brightness exceeding $0^m.3$. In all, the photographic data for 23 dwarfs exhibited variability with $\Delta m_{pg} > 5\sigma$ or low-amplitude brightness variations, which were confirmed by the photoelectric observations. Conclusions about the variability of each star were drawn taking into account the light curve for the corresponding control star. This enabled us to exclude from the list of variable objects those for which apparent brightness variations were produced by changes in the photographic emulsion used.

It was difficult to establish the type of variability observed in V910 Ori and HZ Aqr using the data described. The brightness of V910 Ori cannot be adequately described using mean annual values, since the star is either not visible on the plate and its brightness is conditionally indicated as 18^m, or it is in a state of enhanced brightness, when its brightness grows by $1^m.5 - 2^m$. For HZ Aqr, we obtained only scattered and sparse data.

The variations in the mean annual brightnesses of the remaining 15 stars in our list were the same as those for the control stars in the intervals studied; i.e., they did not exceed $0^m.2$. However, note that some of these exhibited individual events of increase or decrease in their year by mean magnitudes exceeding $0^m.2$ [22, 23].

The mean annual brightnesses of V780 Tau and DX Cnc show a large dispersion, testifying to appreciable yearly variations in the spottedness of their photospheres. We cannot rule out the possibility that there is variability in their mean brightnesses on more extended time intervals.

3. ACTIVITY LEVEL OF THE RED DWARFS

3.1. Variability of the Photospheric Radiation of K *and* M *Dwarfs*

The light curves for ten of the studied stars show variations in their mean annual brightness with a cyclic character, while 13 of the dwarfs exhibit irregular variability or slow trends [22, 23]. The identification of cycles of photospheric activity for the (dKe–dMe) stars remain in most cases only tentative, since

Table 1. Objects for our studies of long-term brightness variations

Star	Gliese number	$\alpha_{1950.0}$	$\delta_{1950.0}$	V	$B-V$	Spectrum	Type of star*	References
V388 Cas	51	$01^h00^m.1$	62°05′.8	13.66	1.68	dM5e	F	[27, 28]
V987 Tau		04 19.2	19 08.5	12.90	1.70	dM4.5e	F	[20]
V833 Tau	171.2	04 33.7	27 02.0	8.40	1.10	dK5e	BY, SB1	[27]
V808 Tau		04 46.2	24 43.0	9.52	1.03	dK3e + dK3e	BY, SB2	[20]
V998 Ori	206	05 29.5	09 47.3	11.50	1.62	dM4e	F	[27, 28]
V780 Tau	1083 AB	05 37.4	24 46.8	14.87	1.88	dM6e	F, VB	[27]
V910 Ori		05 45.2	07 52.0	15.50			F	[20]
V1003 Ori		05 47.3	06 46.0	14.50	1.68		F	[20]
OU Gem	233	06 23.2	18 47.3	6.76	0.94	dK3e	BY, SB2, T	[28, 29]
V577 Mon	234 AB	06 26.9	−02 46.2	11.07	1.71	dM4.5e + dM5e	F, VB	[27, 28, 31]
PZ Mon		06 45.8	01 16.6	9.50	1.10	dK2e	F	[27, 28]
YZ CMi	285	07 42.1	03 40.8	11.23	1.61	dM4.5e	BY	[27, 28, 31]
DX Cnc	1111	08 26.9	26 57.1	14.81	2.06	dM6.5e	F	[27]
CU Cnc		08 28.8	19 39.0	11.93	1.40	dM5e	F, SB	[27, 32]
CV Cnc		08 28.8	19 39.0	13.25	2.50	dM6e	F	[27]
AA Cnc		08 34.4	26 33.2	14.19	1.53			[20]
EI Cnc		08 55.4	19 57.4	13.72	1.87	dM5.5e	F, VB	[33, 34]
GL Vir	1156	12 16.5	11 24.0	13.79	1.83	dMe	F	[27, 33]
FL Vir	473 AB	12 30.9	09 17.6	12.49	1.84	dM5.5e	F, VB	[27, 28, 31]
BF CVn	490 A	12 55.3	35 29.6	10.60	1.42	dM1.5e	BY, VB	[27]
DT Vir	494	12 58.3	12 38.7	9.73	1.49	dM1.5e	BY, SB?	[27, 28]
VW Com	516 AB	13 30.3	17 04.2	11.39	1.53	dM3.5 − 4e	F, VB?	[27, 28]
EQ Vir	517	13 32.1	−08 05.1	9.31	1.21	dK8.5e	BY, SB	[28, 31]
V647 Her	669 A	17 17.9	26 32.8	11.36	1.55	dM4e	F	[27]
V639 Her	669 B	17 17.9	26 32.8	12.97	1.64	dM4.5e	F	[27]
V2354 Sgr		18 27.1	−24 54.1	13.20		dM5	F	[20]
BY Dra	719	18 32.8	51 41.0	8.60	1.19	dK5e + dK7e	BY, SB2	[27, 28]
V816 Her		18 40.4	13 51.0	12.81	1.80	dM4e	F	[27]
V1216 Sgr	729	18 46.7	−23 53.5	10.95	1.60	dM4.5e	F	[27, 28]
V1285 Aql	735	18 53.1	08 20.3	10.07	1.53	dM2 − 3e	F, SB2	[27, 28]
V775 Her		18 53.8	23 29.7	8.04	0.91	dK1e	BY, SB1	[35]
V1816 Cyg		19 29.3	31 15.7				BY	[20]
V1513 Cyg	781	20 03.9	54 18.2	11.97	1.52	dM3e	F, SB	[27]
HU Del	791.2	20 27.4	09 31.2	13.08	1.68	dM7e	F, AB	[27, 28, 36]
V1396 Cyg	815 AB	20 58.2	39 52.7	10.12	1.51	dM3e	BY, T, VB, SB2	[27]
HZ Aqr		21 29.6	00 00.0	9.89	0.98	dK3e + dK7e	BY, SB2	[20]
FG Aqr	852 AB	22 14.7	−09 03.0	13.24	1.74	dM4.5e	F, AB	[20]
DO Cep	860 B	22 26.2	57 26.8	9.59	1.65	dM4.5e	F	[27, 28]
HK Aqr	890	23 05.7	−15 40.8	10.82	1.39	dM1.5e	BY, EB?	[27, 37, 38]
	907.1	23 45.8	−13 15.9	9.61	1.26	dM0e	BY	[39]

* SB1, SB2—spectral binary, VB—visual binary, AB—astrometric binary, EB—eclipsing binary, T—triple system, F— flare star, BY—BY Dra variable.

Table 2. Variations in the mean annual brightness of 40 (dKe–dMe) stars

Star	Interval studied, yrs	Number of plates	Collection*	Variability amplitude Δm_{pg}	Variability time scale, yrs	Type of variability**
V388 Cas	1938–1991	172	3	0.27	6	var
V987 Tau	1960–1988	165	1	0.14		const
V808 Tau	1905–1988	231	1	0.30	17	cyc
V833 Tau	1905–1988	357	1	0.65	16, 60	cyc
V998 Ori	1941–1991	243	3	0.23		const
V780 Tau	1973–1989	99	1	0.34		var
V910 Ori	1951–1993	87	1	~2		?
V1003 Ori	1951–1993	87	1	0.17		const
OU Gem	1899–1987	123	1	0.20	16	var
V577 Mon	1909–1988	70	1	0.40	35	cyc
PZ Mon	1899–1988	565	1–3	1.00	52	cyc
YZ CMi	1927–1990	157	3	0.35	3, 28	cyc
DX Cnc	1984–1989	43	1	0.17		const
CU Cnc	1897–1989	80	1	0.28	16	var
CV Cnc	1963–1989	70	1	0.26	6	var
AA Cnc	1983–1990	60	1	0.06		const
EI Cnc	1963–1987	56	1	0.80	8, 50	var
GL Vir	1963–1991	110	3	0.19		const
FL Vir	1896–1992	404	1, 3	0.38	16	cyc
BF CVn	1899–1989	104	1	0.26	40	var
DT Vir	1911–1989	137	1, 2	0.24	17	var
VW Com	1953–1991	141	3	0.26	20	var
EQ Vir	1914–1988	53	1	0.25	12	var
V647 Her	1939–1991	129	1	0.30	16	var
V639 Her	1939–1991	129	1	0.30	12	var
V2354 Sgr	1960–1988	211	1	0.15		const
BY Dra	1904–1989	125	1	0.50	8, 50	cyc
V816 Her	1899–1989	55	1	0.16		const
V1216 Sgr	1960–1988	237	1	0.11		const
V1285 Aql	1899–1987	108	1	0.17		const
V775 Her	1899–1989	97	1	0.25	28	cyc
V1816 Cyg	1960–1992	188	1	0.28	4	cyc
V1513 Cyg	1952–1989	88	1	0.21		const
HU Del	1940–1990	116	1, 3	0.30	10	cyc
V1396 Cyg	1896–1990	358	1, 3	0.22	16	var
HZ Aqr	1912–1970	66	1	0.26		?
FG Aqr	1966–1989	120	1	0.23		const
DO Cep	1899–1989	152	1	0.20		const
HK Aqr	1960–1989	55	1	0.07		const
Gl 907.1	1925–1989	41	1	0.05		const

* Collections: 1—Sternberg Astronomical Institute, 2—Odessa Observatory, 3—Sonneberg Observatory.

** Type of variability: cyc—cyclic, var—irregular; ?—unknown, const—constant brightness level within the accuracy of the photographic measurements.

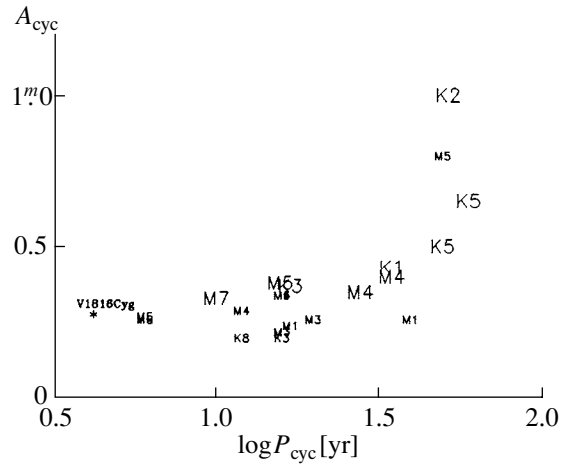

Fig. 2. Amplitudes and characteristic time scales for variability of the mean annual brightnesses of (dKe–dMe) stars. The spectral types indicated in large and small font denote stars with cyclic and irregular variability, respectively; the asterisk shows the position of V1816 Cyg, whose spectral type has not been determined.

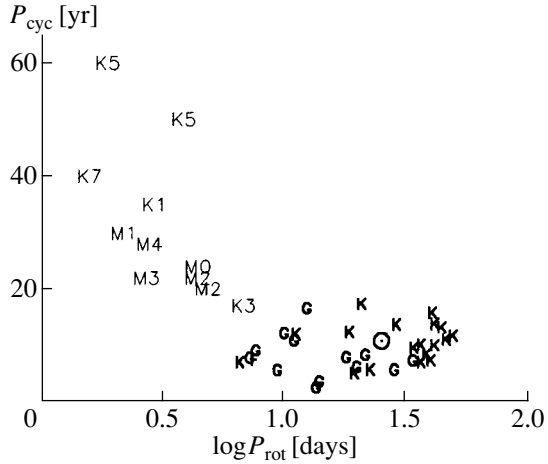

Fig. 3. Rotational periods and durations of the activity cycles of the F–M dwarfs. The spectral types in normal font denote (dKe–dMe) stars from our program and from [24], while those in bold font denote F–K dwarfs studied in the H–K project [6]. The position of the Sun is also indicated.

the durations of the photometric series cover no more than one or two suggested cycles. The characteristic variability times indicated in Table 2 were determined for most stars from the positions of maxima and/or minima in their light curves. In cases when they can be estimated with certainty, the errors in these characteristic times are 1–2 yr. Note that the accuracy in the photometric characteristics depends, first and foremost, on the number of data points, which determines the extent and density of the photometric series. For example, based on photometric series with different durations, cycles of 8 yr [13], 14 yr [14], and 50 yr [16] have been found for BY Dra.

Our results indicate that slow variations in the photospheric brightness on characteristic time scales of 28–60 yr are observed for eight stars. The existence of photospheric activity cycles can be identified with the most certainty for V833 Tau, YZ CMi, and BY Dra, which were first detected in [15, 16] and are confirmed by our own and other independent studies. The durations of the cycles in these stars are 60, 28, and 50 yr, respectively. There are also variations in their mean brightnesses on times scales of $\sim$16 yr, 3 yr, and 8 yr. One characteristic feature of the short time-scale variations is that the maximum brightness is not reached; i.e., the spot-formation processes do not entirely cease, but the spotted regions occupy a smaller fraction of the surface and their effect on the optical radiation of the stars decreases appreciably.

The characteristic time scales for the irregular variability in the mean brightness observed for most of the (dKe–dMe) stars in our list are 8–17 yr, which is comparable to the duration of the 11-year solar cycle. Only three dwarfs display appreciable variability in their photospheric radiation over intervals of 4–6 yrs.

Another indicator of photospheric activity is the amplitude of variations in the mean brightness relative to its maximum. For the stars studied, this quantity has values from $0^m.2$ to $1^m.0$; i.e., it is a factor of 10^2–10^3 higher than for solar-type dwarfs [40]. Active regions occupy a substantial fraction of the surfaces of red dwarfs. The most extensive dark spots are observed at individual epochs for dKe stars. Among the M dwarfs, large-amplitude variability was found only for EI Cnc. It is known that this is a binary star (GJ 1116AB) with high levels of flare activity [34] and X-ray emission [19].

Figure 2 presents a comparison of the characteristics of the variability in the mean brightness, A_{cyc} and P_{cyc}, for the K and M dwarfs. The stars with cyclic activity have a tendency for the variability amplitude to grow with the cycle duration. The highest level of photospheric variability is shown by dwarfs of spectral types K2e–K5e (PZ Mon, V833 Tau, BY Dra). The M dwarfs show variations of $0^m.2$–$0^m.4$, but there is no close relationship between the variability amplitude the $B-V$ color index. In addition, longer cycles are also suspected for the most spotted dKe stars. Thus, the amplitudes and characteristic time scales for the long-term brightness variations of the dKe stars indicate that they have higher level of photospheric activity than the dMe stars.

Our data are not numerous enough to determine the statistical significance of dependences between A_{cyc} and P_{cyc}. Nevertheless, we can see in Fig. 2 that the stars with irregular variability form a group

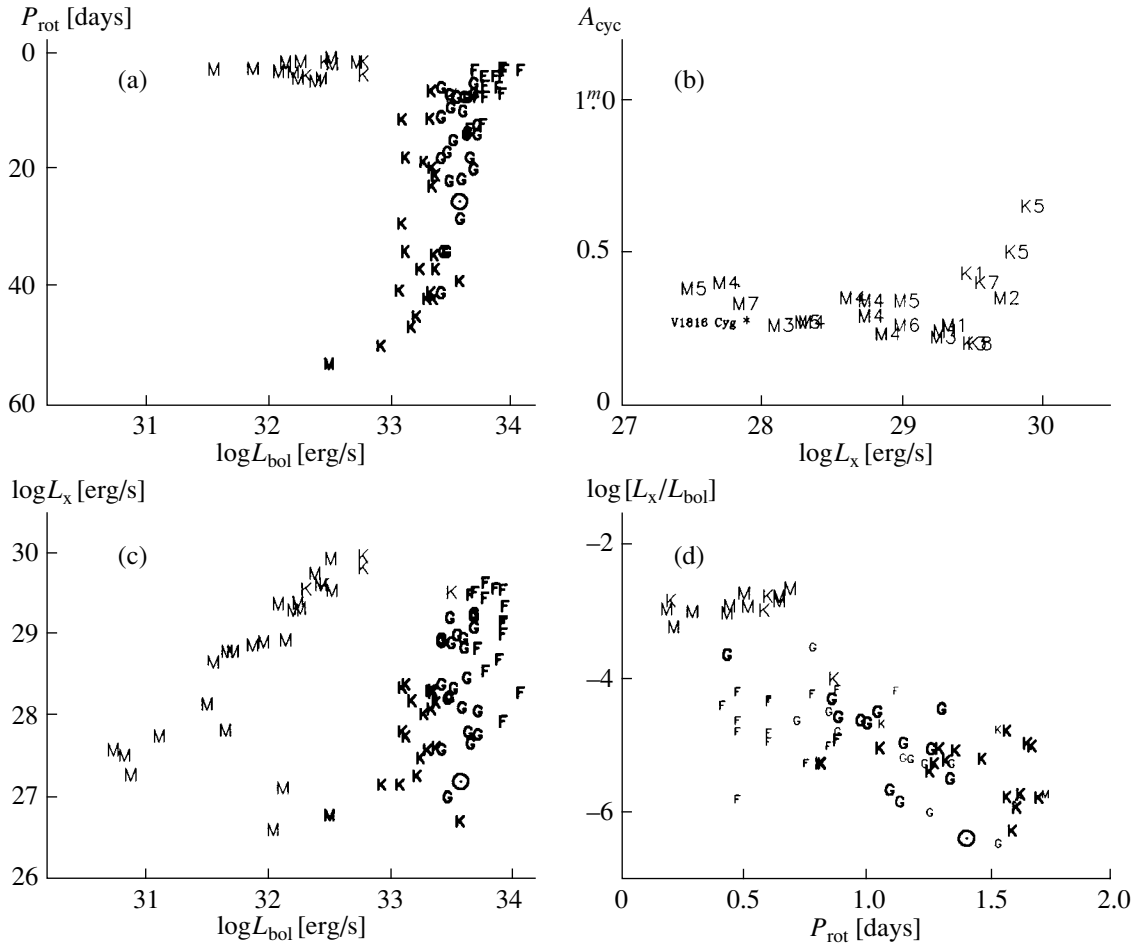

Fig. 4. Rotational period and activity of F–M dwarfs. (a) Rotational periods of (dKe–dMe) stars from our program and F–M main-sequence dwarfs; (b) amplitudes of photospheric variability and X-ray luminosities of (dKe–dMe) stars; (c,d) bolometric and X-ray luminosities of F–M dwarfs and the relationships between these parameters and the rotational period. The normal, large font denotes (dKe–dMe) stars, and the bold font chromospherically active F–M stars from [6]. The asterisk indicates the position of V1816 Cyg, and the position of the Sun is also shown. In the $\log(L_x/L_{bol})$–$\log P_{rot}$ diagram, the small font denotes stars with chaotic variability according to [6].

separate from those with cyclic variations, which is characterized by low-amplitude brightness variations independent of the time scale for the variability. Figure 2 suggests that the photospheric variability of V639 Her, V647 Her, CU Cnc, and CV Cnc may have a cyclic character, since their positions are close to those for dwarfs with cyclic variability. We can even use this figure to conclude that the spectral type of V1816 Cyg should be close to M5.

The development of magnetic cycles is affected by a star's rate of axial rotation and internal structure. An observational relationship between rotation and the duration of stellar cycles was investigated by Vogt [41] based on data for a small number of BY Dra and RS CVn stars. He concluded that the durations of the cycles in rapidly rotating BY Dra stars grow linearly as their rotational periods decreased. Here, we considered the influence of axial rotation on the activity levels of the 11 (dKe–dMe) stars for which there are known values of P_{cyc} and P_{rot} from our results and the data of Alekseev [24]. Figure 3 compares these quantities for the red dwarfs; for comparison, the positions of F–K dwarfs and the Sun based on the data of [6] are also shown. There is no single, clear dependence between the periods of axial rotation and the durations of the proposed cycles for the active F–M dwarfs. Figure 3 can be divided into two sequences: one is formed by the rapidly rotating red dwarfs, and the other by F–K sarfs with rotational periods of 10–50 days. The (dKe–dMe) dwarfs with rotational periods less than 10^d are characterized by a growth in P_{cyc} as the rotational period decreases, but the relationship is not linear; the two stars V833 Tau and BY Dra deviate from the overall dependence, and the positions of two more stars with long cycles are not known, since there is no information about

their rotational periods. The question of a possible relationship between the axial rotation of red dwarfs and the duration of their activity cycles requires further investigation. In contrast to the rapidly rotating (dKe–dMe) stars, the durations of the cycles for the chromospherically active F–K dwarfs with $P_{rot} > 10^d$ are virtually independent of the rate of axial rotation but have an upper envelope of $P_{cyc} < 20$ yrs.

3.2. Bolometric and X-ray Luminosities of the (F–M) Dwarfs

The red dwarfs in our sample are young stars that have not reached the main sequence, as is indicated by Fig. 4a, where they form a group of rapidly rotating objects with logarithmic bolometric luminosities from 32.78 to 30.8 distinct from the HK-project stars [6]. We can see in Fig. 4a that all the F–M dwarfs rotate rapidly before their arrival to the main sequence, after which the rotational periods for stars of a given spectral type increase with age, with the increase being more marked for later-type stars. For example, the rotational periods for the K dwarfs change from 5^d to 50^d, while those for the F dwarfs change from 3^d to 12^d.

The coronal X-ray emission of active, young (dKe–dMe) stars is more powerful than that of stars of the same spectral types on the main sequence (Fig. 4c). The stars in our sample show a linear relationship between $\log L_x$ and $\log L_{bol}$, which can be described by the function $y = 0.96x - 1.76$, with a correlation coefficient of 0.76.

The most energy is radiated by the coronae of highly spotted K dwarfs, but the X-ray luminosities of M dwarfs differ by nearly a factor of 100 in the presence of roughly similar degrees of spottedness for their surfaces (Fig. 4b).

The ratio $\log(L_x/L_{bol})$ for young (dKe–dMe) stars, irrespective of their rotation period, is close to -3 (Fig. 4d). This luminosity ratio is a factor of 10–100 lower for rapidly rotating F–K stars approaching the main sequence, and does not depend on the rotational period. This group of F–K dwarfs includes stars without well-established activity cycles [4, 6]. Activity cycles begin to be observed for stars with $P_{rot} = 8^d$. Activity cycles with durations not exceeding 20 yrs are established in most stars with their entry onto the main sequence. The various indicators of activity show that its intensity, like the rate of axial rotation, decreases with age [7–10]. The ratio L_x/L_{bol} decreases by approximately a factor of 100 compared to its value during the approach to the main sequence.

Note that the positions of three stars from our sample in Figs. 4c, 4d do not correspond to the group of young red dwarfs: OU Gem (K3) has just recently approached the main sequence, while Gl 48 (M3.5) and Gl 229 (M2.5) have already arrived at the main sequence. The HK-project star EK Dra is a young star that has not yet reached the main sequence.

4. CONCLUSION

The photospheric activity of (dKe–dMe) stars associated with the spottedness of their surfaces is highest for rapidly rotating stars of spectral types K2–K5. Evidence for this is provided by the high amplitude of the variations of their mean brightness and the characteristic time scales for their variability (several decades). Computations carried out for zonal spottedness models [42], some using our photometric data, have shown that spots cover 50–70% of the surfaces of K dwarfs, while active regions occupy no more than 30% of the photospheric area of M dwarfs.

Rapidly rotating dKe stars differ from dMe stars in the high luminosity of their X-ray emission; they also show a tendency for $\log L_x$ to grow with the amplitude of the photospheric variability, which is not characteristic of M dwarfs. This latter property of M dwarfs testifies to the action of a different coronal-heating mechanism, such as impulsive flare heating [43, 44]. The red dwarfs investigated by us are young stars that have not reached the main sequence, except for OU Gem, Gl 48, and Gl 229, which are on the verge of entering the main sequence. The rotational periods for the K and M dwarfs in our sample are from 1^d to 7^d. The level of their activity is determined to an appreciable extent by variations in the physical conditions in surface and subphotospheric layers in the transition from K0 to later-type stars.

The activity of rapidly rotating, young red dwarfs differs from that of main-sequence stars in its scale and a number of regularities in its behavior. The spots of solar-type stars cover a small fraction of the surface, with the typical variability of their photospheric radiation being thousandths of a magnitude [40]. The spotted regions in young dwarfs cover up to tens of percent of the photosphere, leading to a growth in the variability amplitude by two to three orders of magnitude. The activity cycles of F–M main-sequence dwarfs have durations not exceeding 20 yrs, independent of the rate of axial rotation. Young (dKe–dMe) stars are characterized by a tendency for the cycle duration to grow to several decades as the rotational period decreases. The X-ray luminosities of young red dwarfs grow linearly with increasing bolometric luminosity. Their coronal emission is more powerful than that of dwarfs of the same spectral types that have reached the main sequence. The ratio $\log(L_x/L_{bol})$ for these stars is about -3, while that for F–M main-sequence dwarfs is two to three orders of magnitude lower.

These regularities indicate that, knowing the rotational period and bolometric and X-ray luminosities of a star, we can determine whether it is a young dwarf or has already become a main-sequence star.

ACKNOWLEDGMENTS

The author is deeply grateful to R.E. Gershberg for discussion of the paper and useful comments. This work was supported by the Ukrainian Foundation for Fundamental Research (grant 02.07/00300).

REFERENCES

1. I. Yu. Alekseev, R. E. Gershberg, M. M. Katsova, and M. A. Livshits, Astron. Zh. **78**, 558 (2001) [Astron. Rep. **45**, 482 (2001)].
2. E. N. Parker, Astrophys. J. **122**, 293 (1955).
3. S. I. Vainshtein, *Magnetic Fields in Space* [in Russian] (Nauka, Moscow, 1983).
4. S. L. Baliunas, R. A. Donahue, W. H. Soon, *et al.*, Astrophys. J. **438**, 269 (1995).
5. G. W. Loockwood, B. A. Skiff, and R. R. Radick, Astrophys. J. **485**, 789 (1997).
6. E. A. Bruevich, M. M. Katsova, and D. D. Sokolov, Astron. Zh. **78**, 827 (2001) [Astron. Rep. **45**, 718 (2001)].
7. S. H. Saar and S. L. Baliunas, Astron. Soc. Pac. Conf. Ser. **27**, 150 (1992).
8. R. W. Noyes, L. W. Hartmann, S. L. Baliunas, *et al.*, Astrophys. J. **279**, 763 (1984).
9. T. N. Rengarajan, Astrophys. J. Lett. **283**, L63 (1984).
10. T. A. Fleming, J. H. M. M. Schmitt, and M. S. Giampapa, Astrophys. J. **450**, 401 (1995).
11. M. M. Katsova and V. Tsikoudi, Astrophys. J. Lett. **402**, L9 (1993).
12. B. J. Kellett and V. Tsikoudi, Mon. Not. R. Astron. Soc. **288**, 411 (1997).
13. P. F. Chugainov, Izv. Krym. Astrofiz. Obs. **48**, 3 (1973).
14. L. N. Mavridis, G. Asteriadis, and F. M. Mahmoud, Contr. Depart. Geodet. Astron. Univ. Thessaloniki **41**, 253 (1982).
15. L. Hartmann, B. W. Bopp, M. Dussault, *et al.*, Astrophys. J. **249**, 662 (1981).
16. M. J. Phillips and L. Hartmann, Astrophys. J. **224**, 182 (1978).
17. B. R. Pettersen, K. P. Panov, M. S. Ivanova, *et al.*, in *Flare Stars in Stellar Clusters, Associations, and Solar Vicinity,* Ed. by L. V. Mirsoyan *et al.* (Kluwer, Dordrecht, 1990), p. 15.
18. I. Yu. Alekseev and R. E. Gershberg, Astron. Soc. Pac. Conf. Ser. **154**, CD-1471 (1999).
19. H. M. M. Schmitt, Jr., T. A. Fleming, and T. S. Giampapa, Astrophys. J. **450**, 392 (1995).
20. R. E. Gershberg, M. M. Katsova, M. N. Lovkaya, *et al.*, Astron. Astrophys., Suppl. Ser. **139**, 555 (1999).
21. N. I. Bondar', Astron. Astrophys., Suppl. Ser. **93**, 111 (1995).
22. N. I. Bondar', Izv. Krym. Astrofiz. Obs. **93**, 215 (1996).
23. N. I. Bondar', Izv. Krym. Astrofiz. Obs. **97**, 17 (2001).
24. I. Yu. Alekseev, Astron. Zh. **77**, 784 (2000) [Astron. Rep. **44**, 696 (2000)].
25. I. Yu. Alekseev and N. I. Bondar', Pis'ma Astron. Zh. **23**, 294 (1997) [Astron. Lett. **23**, 257 (1997)].
26. I. Yu. Alekseev and N. I. Bondar', Astron. Zh. **75**, 742 (1998) [Astron. Rep. **42**, 655 (1998)].
27. B. R. Pettersen, Mem. Soc. Astron. Ital. **62**, 217 (1991).
28. S. M. White, P. D. Jackson, and M. R. Kundu, Astrophys. J., Suppl. Ser. **71**, 895 (1989).
29. R. E. Griffin and B. Emerson, Observatory **95**, 23 (1975).
30. B. W. Bopp, P. V. Noah, A. Klimke, and J. Africano, Astrophys. J. **249**, 210 (1981).
31. J. G. Doyle and C. J. Butler, Astron. Astrophys. **235**, 335 (1990).
32. B. R. Pettersen and M. K. Tsvetkov, Inf. Bull. Var. Stars **2660**, 1 (1985).
33. W. Gliese and H. Jahreiss, Astron. Astrophys., Suppl. Ser. **38**, 423 (1979).
34. B. R. Pettersen, A. L. Cochran, and E. S. Barker, Astron. J. **90**, 2296 (1985).
35. K. G. Strassmeier, D. S. Hall, M. Zeilik, *et al.*, Astron. Astrophys., Suppl. Ser. **72**, 291 (1988).
36. A. P. Cowley and F. D. Hartwick, Astrophys. J. **253**, 237 (1982).
37. A. Young, A. Skumanich, C. Heller, and S. Temple, in *Proceedings of the 3rd Cambridge Workshop on Cool Stars, Stellar Systems, and the Sun,* Ed. by S. L. Baliunas and L. Hartmann (Springer-Verlag, Berlin, 1984), p. 112.
38. P. B. Byrne and D. McKay, Astron. Astrophys. **227**, 490 (1990).
39. B. W. Bopp, Astrophys. J. **317**, 781 (1987).
40. R. R. Radick, G. W. Loockwood, and B. A. Skiff, Astrophys. J., Suppl. Ser. **118**, 239 (1998).
41. S. S. Vogt, in *Activity in Red-Dwarf Stars (IAU Colloq. 71)*, Ed. by P. B. Byrne and M. Rodono (Reidel, Dordrecht, 1975), p. 137.
42. I. Yu. Alekseev, *Low-Mass Spotted Stars* [in Russian] (Astroprint, Odessa, 2001).
43. M. M. Katsova, O. G. Badalyan, and M. A. Livshits, Astron. Zh. **64**, 1243 (1987) [Sov. Astron. **31**, 652 (1987)].
44. J. C. Doyle and C. J. Butler, Nature **313**, 378 (1985).

Translated by D. Gabuzda

Astronomy Reports, Vol. 46, No. 6, 2002, pp. 497–514. Translated from Astronomicheskiĭ Zhurnal, Vol. 79, No. 6, 2002, pp. 551–569.

Flare-Plasma Diagnostics from Millisecond Pulsations of the Solar Radio Emission

V. F. Melnikov [1], G. D. Fleishman[2], Q. J. Fu[3], and G.-L. Huang[4]

[1] *Radiophysical Research Institute, ul. Bolshaya Pecherskaya 25/14, Nizhni Novgorod, 603600 Russia*

[2] *Ioffe Physicotechnical Institute, Russian Academy of Sciences, ul. Politekhnicheskaya 26, St. Petersburg, 194021 Russia*

[3] *Beijing Astronomical Observatory, National Astronomical Observatories, Beijing, 100012 P. R. China*

[4] *Purple Mountain Observatory, National Astronomical Observatories, Nanjing, 210008 P. R. China*

Received September 14, 2001; in final form, November 23, 2001

Abstract—Two solar radio bursts exhibiting narrow-band millisecond pulsations in intensity and polarization are analyzed. There were considerable time delays between the left- and right-circularly polarized components of the radio emission. The observed oscillations of the degree of polarization are due to the different group velocities of the ordinary and extraordinary modes in their propagation from the source to the observer; the frequency dependence of the delay is in excellent agreement with the theoretically calculated group delay in a magnetoactive plasma. It unambiguously follows that the pulsed radio emission is generated near the double upper hybrid frequency by the nonlinear plasma mechanism, since the source emission has a low degree of polarization. In addition to dispersion effects, a Fourier analysis also reveals effects associated with the source inhomogeneity. We detected a frequency drift of pulsations (autodelays) with different signs for different polarization components. This drift suggests that, apart from the dispersion effects, there are also the effects related to inhomogeneity of the radio source. It is shown, in particular, that the upper hybrid modes (generating the radio emission) are unstable in regions with enhanced gradients of the plasma density and/or magnetic field. © *2002 MAIK "Nauka/Interperiodica"*.

1. INTRODUCTION

The phenomenon of solar flares is inseparably linked to processes enabling powerful energy release in the solar corona plasma. The stored energy is released in the form of macroscopic motion of the medium, plasma heating, and acceleration of some fraction of the charged particles to high energies.

In recent years, much attention has been given to studies of the X-ray radiation of solar flares, due to clear successes in improving X-ray observational databases and the relative simplicity of interpreting the available observational data. The intensity of soft X-rays is determined by the emission measure and plasma temperature, while that of hard X-rays is determined primarily by the spectrum of fast (suprathermal) electrons.

Interpreting radio observations is considerably more complicated. Even in the relatively simple case of radio continuum bursts, the properties of the radio emission (its spectrum and polarization, as well as their time dependence) depend on many parameters: the magnetic-field intensity, background plasma density, and spectrum of the injected electrons, and their kinetics in a magnet trap, which in turn are determined by the trap size, mirror ratio, and distribution of thermal plasma [1, 2].

If, in addition, collective effects are important in generating the radio emission, the analysis becomes even more complicated and requires a detailed theory. Another important factor complicating analysis of the general properties of the radio emission is the effects of its propagation through the corona (which, generally speaking, will be different for the ordinary and extraordinary eigenmodes), which include absorption and scattering (depolarization) of the radio waves, as well as manifestations of frequency dispersion.

To illustrate the importance of propagation effects for reliable interpretation of the radio data, we give a simple example. It is well known that the polarization of received radiation plays an important role in our identification of the microscopic mechanism generating this radiation.

Let us suppose that a radio source emits unpolarized radiation that then propagates through the corona, where the extraordinary waves are absorbed much more strongly than the ordinary waves (this is possible if the radio frequency is close to low harmonics of the gyrofrequency). In this case, the observed

1063-7729/02/4606-0497$22.00

radio emission is nearly 100% polarized. On the contrary, let the source generate 100% polarized radio emission that then passes through a region of enhanced scattering, where the ordinary and extraordinary waves can be transformed into each other. In this case, we will observe weakly polarized emission. This demonstrates that the observed polarization can differ strongly from the intrinsic source polarization, and a straightforward use of polarization data to identify the emission mechanism may lead to serious errors.

In this paper, we analyze bursts of solar radio emission displaying quasi-periodic millisecond pulsations (with a period of $\sim$40 ms) recorded with a time resolution of 8 ms and a spectral resolution of 10 MHz in both left- and right-circular polarizations (LCP and RCP). As we will show below, the observed unusual behavior of the polarization (which oscillates with the same period as the emission intensity) enables us to conclude that the source emission has a low degree of circular polarization. This unambiguously demonstrates that the radio emission is generated by the nonlinear plasma mechanism, enabling us to apply the detailed theory for this mechanism in our analysis [3–6]. Moreover, a careful analysis of the frequency dependences of the group delays enables us to separate the effects of propagation of the emission from the effects of source inhomogeneity. All this provides a set of detailed diagnostics of the flare plasma.

2. OBSERVATIONS

2.1. Description of the Instrument

The events in question were registered at the Huayrou station with the radio spectrometer of the Beijing Astronomical Observatory at frequencies of 2.6–3.8 GHz [7]. The duration of a spectrum record was 8 ms for a total frequency bandwidth of 1.2 GHz. This band was divided into four 300-MHz subbands, each having 30 parallel channels (with bandwidths of 10 MHz). During the first 4 ms of each 8-ms interval, the computer stored data for the LCP signal, using 1 ms consecutively for each of the four 300-MHz subbands, beginning with the lowest frequency subband; this procedure was repeated for the RCP signal during the second 4 ms. In each 1-ms interval, the first 0.8 ms was used to integrate the signal, while the remaining 0.2 ms were used for signal output and recording in all thirty parallel channels.

2.2. Description of the Events

In the growth phase of the radio continuum burst of November 2, 1997, from 03:02:17 to 03:02:21 UT, we recorded two trains of narrow-band pulsations at frequencies $f = 2.80$–2.89 and 3.02–3.09 GHz (Figs. 1, 2). The Hiraiso station simultaneously recorded a pulsed radio burst with a maximum flux density of about 5 sfu near 3 GHz; intense type III bursts were observed at meter and decimeter wavelengths [8]. At the same time, the GOES spacecraft recorded an impulsive flare in soft X-rays. A corresponding H_α flare (SB) took place near the solar disk center (S20 E01).

This burst was observed in Beijing at noon, when the Sun was high in the sky, and the contribution of the beam sidelobes was negligible. We observed no similar effects in other time intervals. Thus, we feel confident of the solar origin of the bursts in question.

Figure 2 shows dynamic spectra of the pulsations for both polarizations. The time profiles of the intensities of the LCP and RCP components and of the degree of polarization are presented in Fig. 3. Figure 4 shows that the pulsations in opposite polarizations are shifted relative to each other by a significant fraction of the period. No other such delays have been reported in the literature, to our knowledge.

Like the degree of polarization, the emission in both polarizations oscillates with a period of $\tau \approx 40$ ms. The degree of polarization reaches values close to 100%. The time-averaged degrees of circular polarization are small (1–10%, depending on the averaging time), and, overall, the emission displays weak circular polarization.

3. ANALYSIS OF THE PERIODICITY AND TIME DELAYS

3.1. Periodicity of the Pulsations

We used the Fourier method to perform a quantitative analysis of the oscillations. Figure 5 shows the Fourier spectra of the high- and low-frequency events.

Narrow spectral peaks are clearly visible near $\tau = 40$ ms and $\tau = 20$ ms, with the amplitude considerably exceeding the noise level for both events. The peak at $\tau = 20$ ms is less intense and is obviously the second harmonic of the main peak at $\tau = 40$ ms. In contrast to the low-frequency event, there are three relatively weak additional peaks in the high-frequency event, at $\tau \approx 29$, 67, and 100 ms, reflecting the less regular character of the radio pulsations in this event. Figures 5c, 5d show detailed profiles of the main spectral peak for both events. We obtained these curves using the zero addition method, which improves the accuracy of the spectral-peak frequency when a Fast Fourier Transform is used [9]. We can see that the halfwidth of the resulting peak is on the order of 1 ms.

The position of the spectral peak (and, accordingly, the pulsation period) varies slightly (by about 0.2–0.4 ms) as a function of the duration of the chosen segment and the signal frequency and mode (Fig. 6).

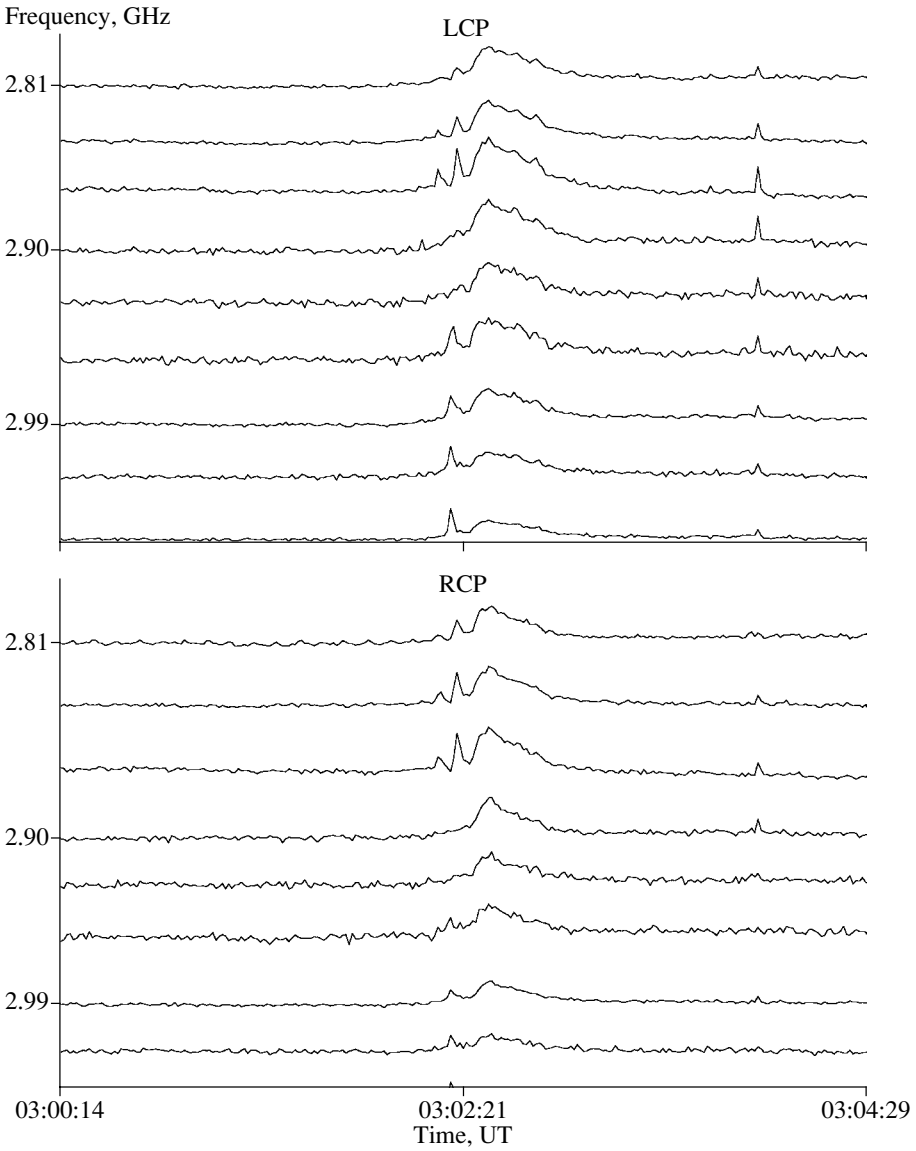

Fig. 1. Time profiles of the radio burst of November 2, 1997, with 1-s time resolution. The narrow-band pulsations took place in the growth stage, from 03:02:17 UT to 03:02:21 UT.

However, these period variations are not large. The finite duration of the pulsation trains ($\Delta t \sim 2 - 3$ s) limits the accuracy of the period:

$$\Delta\tau \sim \tau^2/\Delta t \sim 0.8 \text{ ms}. \quad (1)$$

This value is consistent with the halfwidth of the spectral peak in Fig. 5, which is close to 1 ms (Figs. 5c, 5d). Since the period variations we have found do not exceed 0.8 ms, we conclude that there were no significant changes of the pulsation period in these events.

3.2. The Frequency Spectrum of the Pulsations

We found the shape of the pulsation frequency spectrum from the Fourier amplitudes of the pulsation trains in each frequency channel. These spectra are presented in Fig. 7 separately for the left- and right-circularly polarized components. We see that, in general, these spectra are similar. The spectral full widths at half maximum are 40–50 MHz for both components, i.e., about 1.5% of the central frequency. The RCP emission peaks at $f = 2.85$ GHz and the LCP emission at $f = 2.87$ GHz. However, an interesting thing is that the spectra are appreciably shifted in frequency from each other.

3.3. Frequency Dependence of the Group Delay between Eigenmodes of the Magnetoactive Plasma

The simplest and most natural explanation for the observed time delays between the LCP and RCP

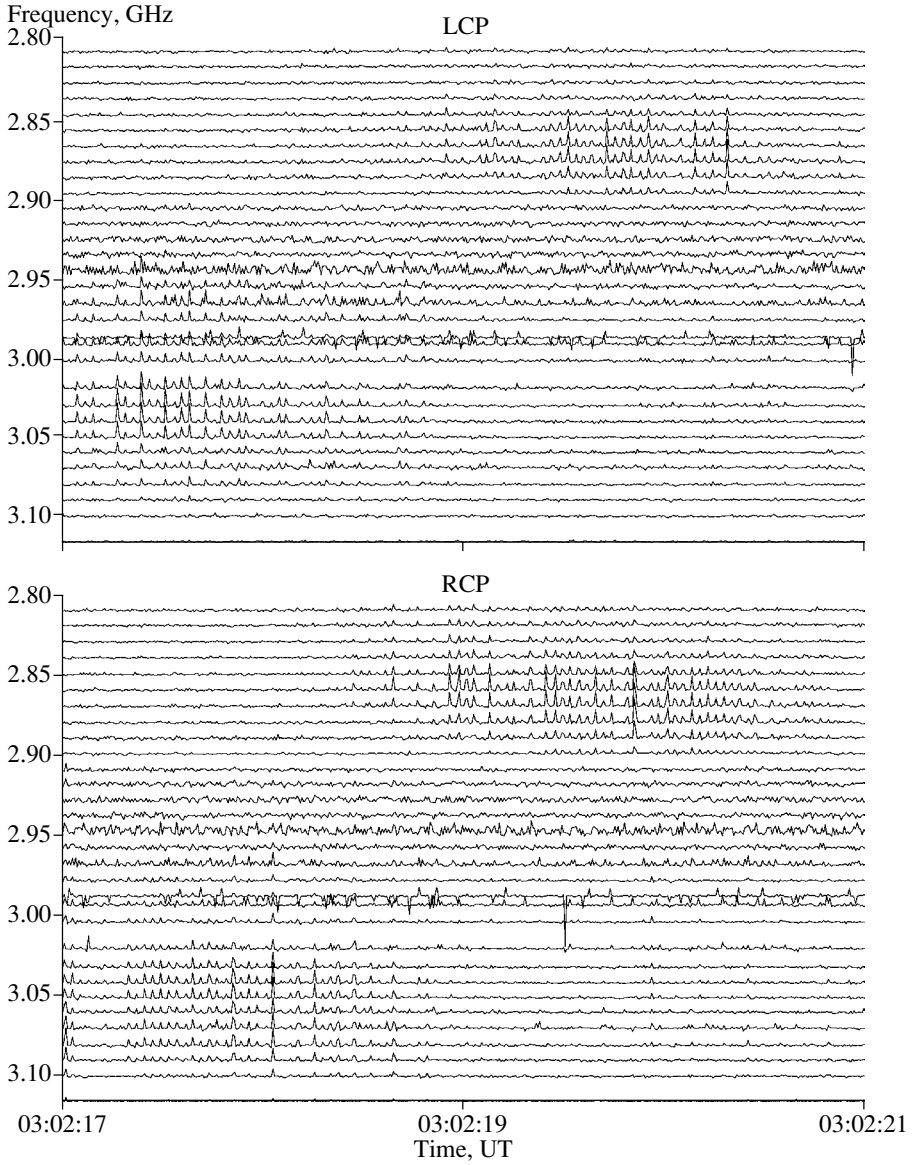

Fig. 2. Dynamical spectra of the pulsations in the LCP and RCP channels. Two narrow-band events are clearly visible near 2.85 and 3.05 GHz.

signals is probably the following. A relatively compact source generates pulsed radio emission with a low degree of circular polarization [i.e., the ordinary (O) and extraordinary (X) modes are emitted in phase], after which these waves propagate in the corona with different group velocities so that the peaks of the LCP and RCP signals do not reach the Earth simultaneously. Thus, the LCP signal dominates during one part of the period, and the RCP signal, during the other part, leading to the observed oscillations of the degree of circular polarization of the emission.

Let us find the frequency dependence of the time delay associated with this effect. In this section, for simplicity, we will assume that the source is unresolved and that the square of the emission frequency is much greater than the square of the plasma frequency along the path of the radio signal: $\omega^2 \gg \omega_p^2$. Then, the group velocities of the eigenmodes can be written

$$\frac{c}{v_{x,o}} \approx 1 + \frac{\omega_{pe}^2}{2\omega^2} - \sigma\frac{\omega_{pe}^2\omega_{Be||}}{\omega^3}, \qquad (2)$$

where $\sigma = 1$ for O waves and $\sigma = -1$ for X waves.

The time delay between simultaneously emitted O and X waves is described by the integral along the propagation path of the wave:

$$\Delta t_g = \int_0^\infty (\frac{1}{v_x} - \frac{1}{v_o})dz \qquad (3)$$
$$= \frac{2}{c}\int_0^\infty \frac{\omega_{pe}^2(z)\omega_{Be||}(z)}{\omega^3}dz;$$

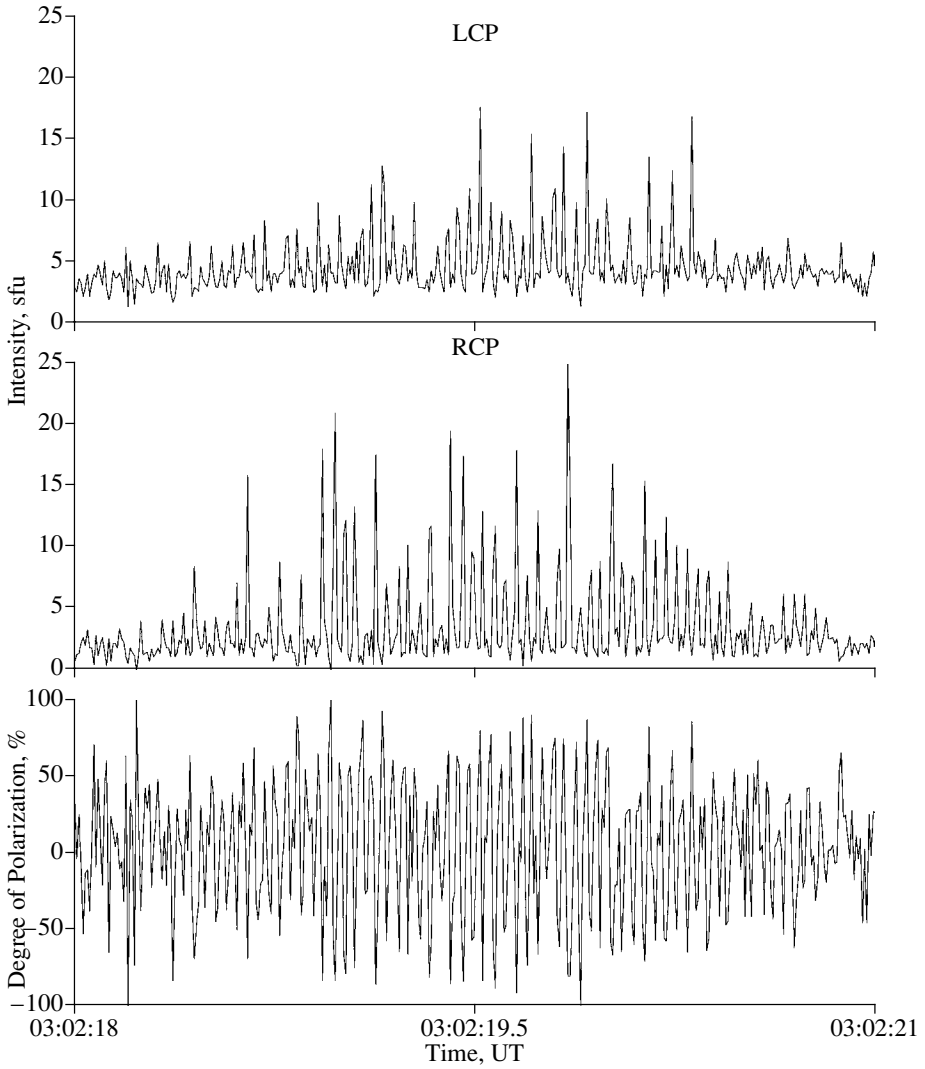

Fig. 3. Time profiles of the LCP and RCP intensities and the degree of polarization at $f = 2.85$ GHz.

i.e., in the absence of other effects, the group delay decreases as the third power of the signal frequency:

$$\Delta t_g \propto f^{-3}. \tag{4}$$

We can readily estimate that the absolute value of the difference of the group delays at 2.81 and 2.89 GHz in our case is

$$\delta t_g \approx \Delta t_g \frac{3\Delta f}{f_o} \sim 1.7 \text{ ms}. \tag{5}$$

In spite of the fact that this quantity is much smaller than the instrumental resolution (8 ms), the presence of numerous oscillation periods enables us to determine the relative delays to a much higher accuracy, considerably exceeding the time resolution.

3.3.1. Derivation of the delays using the Fourier method. For quasi-periodic pulsations (with narrow spectral peaks, Fig. 5), we can apply well-known Fourier methods to accurately determine the signal phase. A digitized signal carries very precise information on the parameters of the real signal, including its phase, if the sampling rate provides more than two points per period of the signal. This condition is fulfilled in our case, since there are five points per period. Thus, we expect to be able to obtain precise estimates of the delays, which will enable us to establish their frequency dependence.

Fourier analysis enables us to calculate the phase of each spectral component using the formula

$$\phi(\nu) = \arctan\left(\frac{\mathrm{Im}I(\nu)}{\mathrm{Re}I(\nu)}\right), \tag{6}$$

where $\mathrm{Re}I(\nu)$ and $\mathrm{Im}I(\nu)$ are the real and imaginary parts of the Fourier transform at frequency ν. For quasi-periodic signals, the problem reduces to a search for the signal phase at the frequency of the spectral peak $\nu_p = 1/\tau_p$ (Fig. 5). After finding the

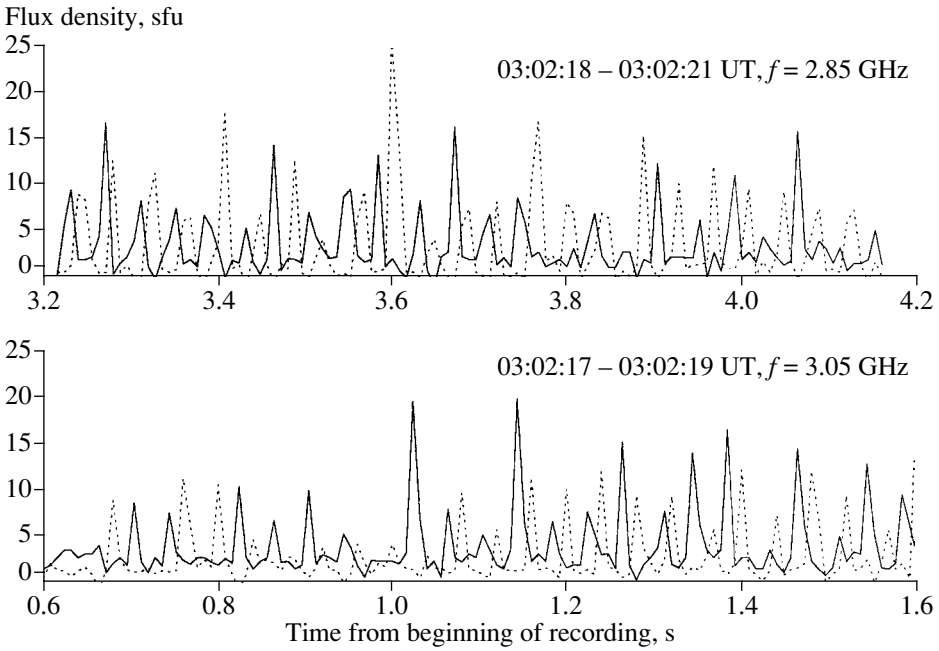

Fig. 4. Selected fragments of the RCP (solid curve) and LCP (dashed curve) recordings for $f = 2.85$ and 3.05 GHz. The time delay between the components is readily visible.

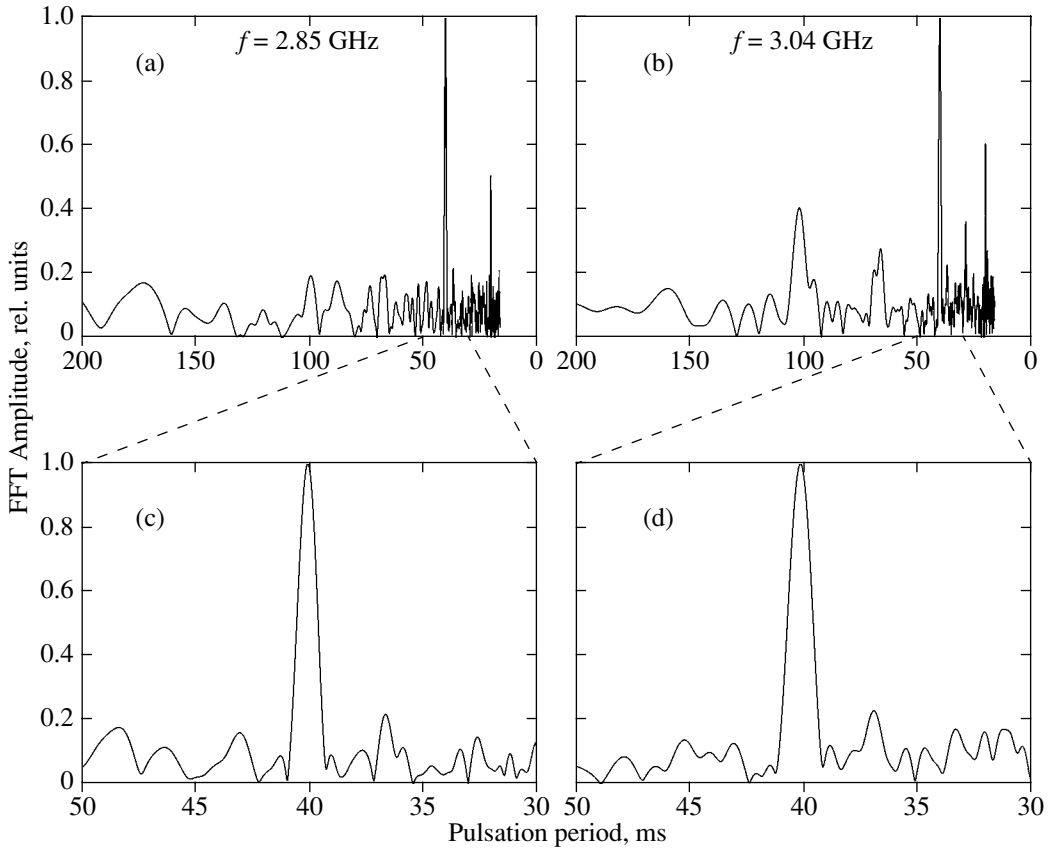

Fig. 5. Fourier spectra of the RCP components for the (a) low-frequency and (b) high-frequency events, obtained at 03:02:18.5–03:02:20.5 UT and 03:02:17.0–03:02:18.5 UT, respectively (see. Fig. 2). The main spectral peaks for these events are shown in more detail in the bottom panels (c, d).

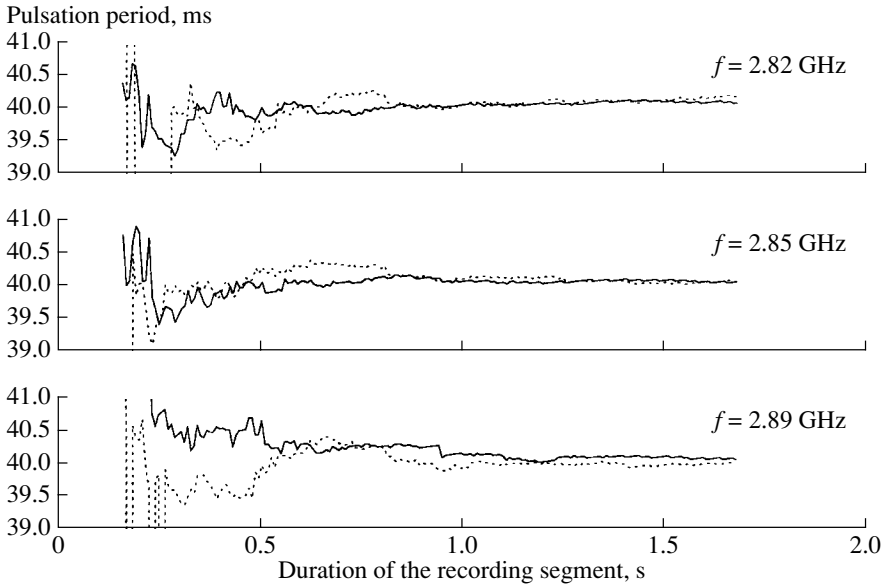

Fig. 6. Pulsation period τ_p at various frequencies as a function of the duration of the analyzed record segment for the RCP (solid curve) and LCP (dashed curve) components.

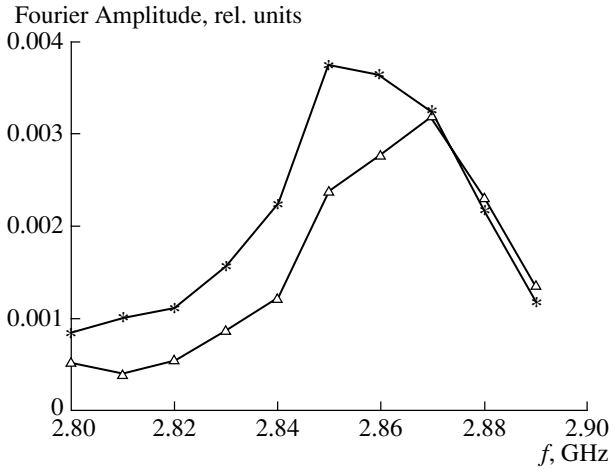

Fig. 7. Fourier amplitudes of the pulsations as a function of frequency for the RCP (asterisks) and LCP (triangles) components.

phases of the RCP and LCP components (in a certain time interval), the delay between these signals is calculated as

$$\Delta t_d = \frac{\phi_R(\nu_p) - \phi_L(\nu_p)}{2\pi\nu_p}, \qquad (7)$$

where $\nu_p = \nu_{pL}$ or $\nu_p = \nu_{pR}$ is one of the two slightly differing values of the spectral-peak frequency, found for the LCP and RCP signals, respectively.

Note that, owing to the signal's periodicity, the delay found in this way is subject to ambiguities. Let us consider a simple situation where there is one true delay Δt_{ph} between the signals. Generally speaking, this delay can be either greater or smaller than the period, and can be negative or positive. How will the presence of such a delay be manifest in the Fourier analysis? It is easy to understand that, even if the delay is greater than the period, i.e.,

$$\Delta t_{ph} > \tau, \qquad (8)$$

the Fourier analysis would find a delay Δt_d in the interval

$$0 < |\Delta t_d| < \tau \qquad (9)$$

so that

$$\Delta t_d = \Delta t_{ph} + m\tau, \qquad (10)$$

where m is an integer. In particular, the value $\tau - \Delta t_d$ is also in the interval (9). Thus, if we have found some value of the delay Δt_d, this means that there are a

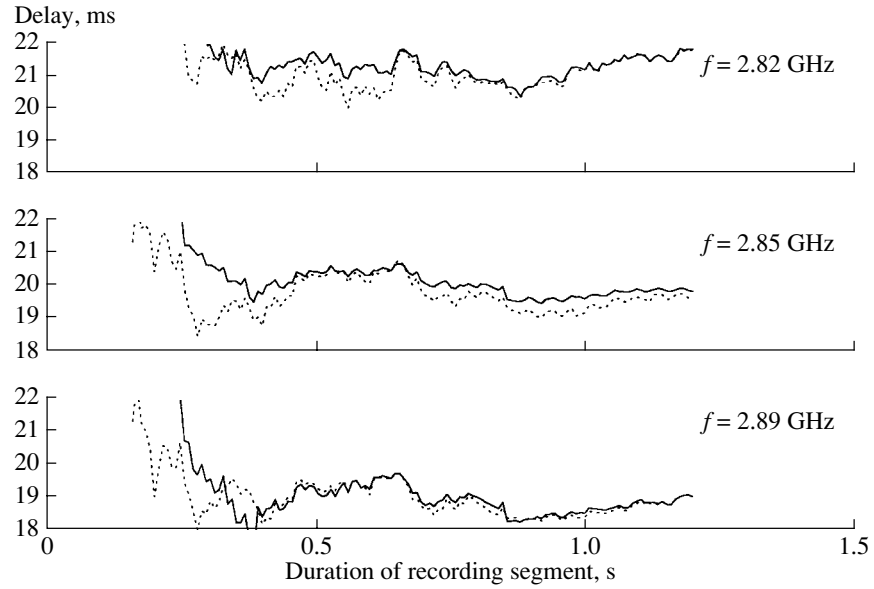

Fig. 8. Dependence of the delay at various frequencies on the duration of the analyzed recording segment for the RCP (solid curve) and LCP (dashed curve) components.

whole series of possible values of the true delay. To choose the true value from the series (10), we must take into account additional considerations.

3.3.2. Errors of the delays. The delays we have calculated vary quite widely as functions of the chosen frequency channel and duration of the analyzed interval of the pulsations (Fig. 8). For segments that are too short and channels with signal-to-noise ratios that are too low, the delays are unstable. For the low-frequency event, we could obtain stable values only at frequencies 2.81–2.89 GHz for intervals longer than 0.5 s.

Let us consider in more detail the stability of the obtained delays and probable sources of errors. It is known that the error of the phase of an oscillating function with superimposed noise is [10]:

$$\delta\phi = \frac{\text{noise}}{\text{signal}}\frac{1}{\sqrt{K}}, \qquad (11)$$

where K is the number of periods of the analyzed periodic function.

To estimate the error of the delay between the RCP and LCP components, we can use the obvious relationship $\delta t_d = \Delta\phi/(2\pi\nu_p)$, or

$$\delta t_d = \frac{\sigma_N}{\sqrt{2}\sigma_S}\frac{1}{(\sqrt{K}2\pi\nu_p)}, \qquad (12)$$

where σ_N is the standard deviation in the noise signal before the onset of the pulsations or after their termination, and σ_S is the standard deviation in the pulsed signal.

Thus, the error of the delay depends strongly on the signal-to-noise ratio and the number of oscillation periods. In particular, in the low-frequency event at frequency $f = 2.85$ GHz the signal-to-noise ratio for the first 50 periods is ~ 5 and the error of the delay is ~ 0.3 ms. For this same time interval, the error at 2.81 GHz grows to 0.8 ms due to the reduced signal-to-noise ratio at this frequency.

Finally, recall that the procedure used by the radio spectrometer to record the signal results in a systematic 4-ms shift between the LCP and RCP records at each frequency. This systematic error was removed by applying an appropriate 4-ms correction.

3.3.3. Frequency dependences. We analyzed various time intervals of the records for both pulsed events and found a fairly stable power-law frequency dependence for the delays. The dependence for the low-frequency event is more pronounced (since it is characterized by a single strong spectral peak; i.e., the periodicity is expressed more strongly than in the high-frequency event).

We choose one of the delays from set (10) using a cross-correlation method. Since both the envelope and carrier are correlated for two real signals having a common physical origin, we can determine the number of periods by which the quasi-periodic signals are shifted relative to each other by analyzing the envelope of the cross-correlation function. Since we are interested in time intervals of the order of the oscillation period, we can neglect differences of 1–2 ms and analyze the signal summed over all the frequency channels (this procedure improves the signal-to-noise ratio, increasing the stability of the results).

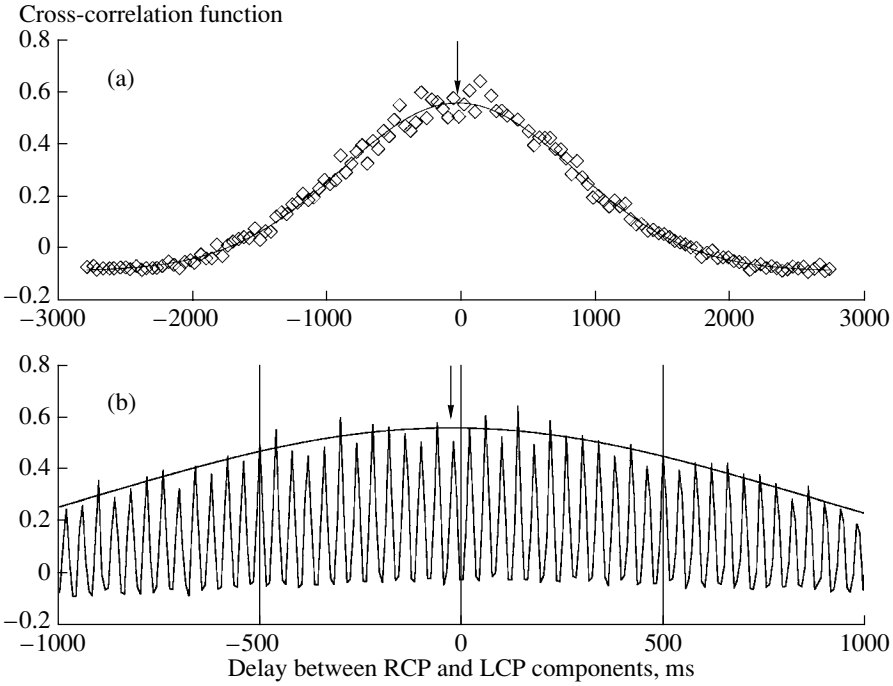

Fig. 9. (a) Peaks of the cross-correlation function of the signal integrated over nine frequency channels (squares) and the corresponding Gaussian fit (solid curve). (b) Cross-correlation function and Gaussian fit for a limited range of time delays. The arrow shows the position of the Gaussian peak.

Figure 9 shows the resulting cross-correlation function, whose envelope has been approximated with a Gaussian. The Gaussian maximum (marked by an arrow) corresponds to a relative shift of the signals by approximately a half-period, with the LCP signal lagging. Thus, this procedure enables us to choose a single value (namely, $m = 0$) from the set (10).

A typical example of the frequency dependence of the delay is given in Fig. 10. The delay was calculated for the frequencies of the spectral peaks of the RCP and LCP components (Fig. 7). These values are close to each other and are within the errors in the delays, illustrating the stability of the method used to determine the delays.

The frequency dependence of the delay is clearly visible in Fig. 10. The correlation coefficients for various 1-s intervals are in the range 0.80–0.96. The increased error at the lower frequencies is due to the corresponding decrease in the signal-to-noise ratio. On the whole, the errors, 0.3–0.8 ms, are considerably smaller than the range of the delay variations with frequency, ~ 2 ms.

In this case, the RCP component leads the LCP component (by approximately 20 ms); i.e., the RCP waves represent the ordinary mode and the LCP waves the extraordinary mode. Thus, in the region providing the observed group delay, the magnetic field is directed away from the Earth; that is (in a simple geometry), the corresponding sunspot on the photosphere has southern polarity.

Using the Fourier method for determining the delays reveals a frequency drift of the pulsations, i.e., the frequency dependence of the time shift (autodelay) of the pulsating signal at a given frequency relative to the corresponding signal at some reference frequency for the same polarization component. The correlation diagram for this dependence is shown in Fig. 11. We chose 2.81 GHz as the reference frequency. The triangles and circles mark the autodelays for the right- and left-circularly polarized signals, respectively. Note that the autodelays behave differently for different radiation modes: the delay increases for the R-modes and decreases for the L-mode with increasing frequency.

4. RADIO EMISSION MECHANISM AND SOURCE PLASMA DIAGNOSTICS

The results of the previous section are of fundamental importance for determining the microscopic mechanism for the radio emission in these pulsed events. It has been unambiguously shown that the appreciable (and oscillating) degree of polarization developed due to the effects of propagation in the corona, while the source actually generates radio emission with a low degree of polarization.

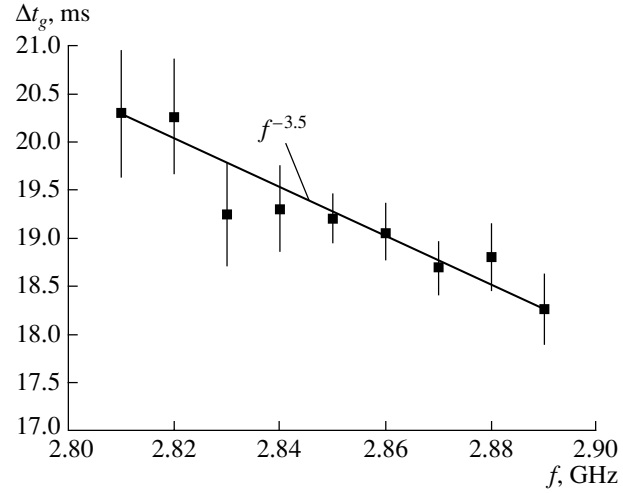

Fig. 10. Frequency dependence of the delay between the RCP and LCP components of the pulsation. The delays were determined for the oscillation frequencies corresponding to the Fourier peaks for the RCP and LCP components. The line shows the theoretical relation obtained using exact formulas for the group velocities of the transverse waves and taking into account the inhomogeneity of the source ($\propto f^{-3.5}$).

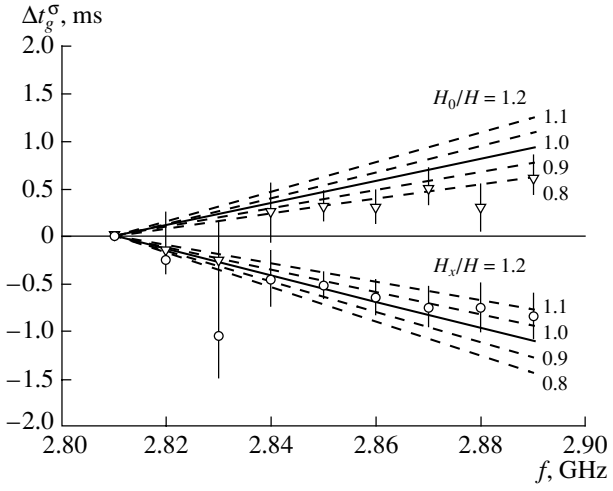

Fig. 11. Delays of the wave arrival at an arbitrary frequency relative to the arrival of waves with the same polarization at the reference frequency $f = 2.81$ GHz (autodelays) for the RCP (triangles) and LCP (circles) components. The lines show the model curves obtained for various ratios of the effective scales; the solid lines correspond to identical values of the effective scales.

On the other hand, it is obvious that such narrowband radio emission can only be generated by a coherent mechanism; i.e., either a cyclotron maser or plasma mechanism. For our analysis, it is fundamentally important that both cyclotron maser emission near any harmonic of the gyrofrequency and plasma emission near the first harmonic of the plasma frequency have a very high degree of polarization in the source (close to 100%).

A definite conclusion follows: in the pulsed events considered, the emission must be generated by the plasma mechanism near the *second* harmonic of the plasma frequency (since only then can the degree of circular polarization of the source emission be low).

It is well known [3, 4] that the plasma mechanism can generate pulsed radio emission if nonlinear interactions of plasma waves with each other are important. This type of plasma mechanism is usually called the nonlinear plasma mechanism for radio emission [3, 4].

4.1. The Nonlinear Plasma Mechanism for Radio Emission

For convenience and completeness, we will summarize the basic properties of the nonlinear plasma mechanism. In general, the plasma mechanism for radio emission is a two-step process. The first stage is the generation of plasma (Langmuir, upper hybrid, etc.) waves, and the second is the conversion of the plasma waves into radio waves (O, X modes). In the nonlinear plasma mechanism, the evolution of the plasma waves is substantially influenced by nonlinear interactions between the waves.

Numerical studies of the nonlinear plasma mechanism [5, 6] show that the energy density of the excited plasma (upper hybrid) waves displays either nonperiodic pulsations or quasi-periodic oscillations, depending on the size and shape of the region of instability of the upper hybrid waves provided by the realized distribution of fast electrons.

Quasi-periodic solutions appear for relatively narrow (in the wave-vector plane) regions of instability, while nonperiodic pulsations arise for more extended regions. Naturally, if the distribution of fast electrons changes, the region of plasma-wave instability can also change, together with the mode of the pulsations. Such changes may be observed as phase jumps or variations in the oscillation period.

In our subsequent analysis, it is important to take into account the fact that the effective increment for the plasma-wave generation is determined by the difference between the wave increment provided by the fast electrons and the (collisional and collisionless) decrement associated with the background plasma. Narrow regions of instability are formed more easily if the instability operates in a weakly above-threshold regime (with the threshold determined by the wave decrement). In this case, we expect that the conditions for instability are fulfilled only in a small region of a nonuniform magnetic trap, while wave attenuation dominates in the bulk of the trap. Precisely this may

be the origin of the narrow spectral band occupied by the pulsations in the analyzed events.

4.2. Radio Source Diagnostics

Since the total spectral width of the radio emission is

$$\Delta f/f \approx 3\%, \tag{13}$$

we can, to first approximation (i.e., with an accuracy of $\sim 3\%$) consider the radio source to be homogeneous. We will use this approach to find the mean source parameters in this section, considering later the effects of source inhomogeneity.

In a plasma with

$$Y = \omega_{pe}/\omega_{Be} \geq 1, \tag{14}$$

it is most easy to generate upper hybrid waves. The spectrum of such waves in a cold plasma is

$$\omega_{UH}^2 = \left[\frac{1}{2}(\omega_{pe}^2 + \omega_{Be}^2)\right. \tag{15}$$
$$\left. + \frac{1}{2}\left[(\omega_{pe}^2 + \omega_{Be}^2)^2 - 4\omega_{pe}^2\omega_{Be}^2\cos^2\theta\right]^{1/2}\right],$$

where θ is the angle between the wave vector and the magnetic field. The thermal motion of the electrons of the background plasma gives a correction to this frequency

$$\delta\omega_{UH}^2 = 3\omega_{UH}^2 k^2 d_e^2, \tag{16}$$

where d_e is the electron Debye radius. The distribution of fast electrons, which has a loss cone along the magnetic field, generates upper hybrid waves in directions quasi-transverse to the magnetic field [5, 6]; i.e.,

$$\omega_{UH} \approx (\omega_{pe}^2 + \omega_{Be}^2)^{1/2}, \tag{17}$$

so the frequency of the observed radio emission is twice the upper hybrid frequency:

$$\omega \approx 2\omega_{UH}. \tag{18}$$

For $Y \geq 1$, the value of ω_{UH} varies from ω_{pe} (for $Y \gg 1$) to $\sqrt{2}\omega_{pe}$ (for $Y = 1$). Note that an appreciable group delay can arise only if the plasma gyrotropy is sufficiently strong; i.e., if ω_{Be} is not too small compared to ω_{pe} and Y is close to unity. On the other hand, we can estimate an upper limit for the gyrofrequency under the following assumptions. It is known that extraordinary waves in the solar corona are strongly attenuated in the gyrolayers $\omega = \omega_{Be}$, $2\omega_{Be}$, $3\omega_{Be}$. Since the average polarization of the pulsations is low, this means that extraordinary waves have reached the Earth without being absorbed in these gyrolayers, and, consequently, we have in the source and along the ray path

$$\omega_{Be} \leq \omega/3 \tag{19}$$

or, using (17) and (18),

$$\omega_{Be} \leq 0.89\omega_{pe}. \tag{20}$$

If we take into account that

$$\omega \approx 2\pi(2.85 \pm 0.04) \times 10^9 \text{ s}^{-1}, \tag{21}$$

we obtain

$$B < 325 \text{ G}, \tag{22}$$

$$1.3 \times 10^{10} < n < 2.5 \times 10^{10} \text{ cm}^{-3}, \tag{23}$$

where B is the magnetic field (the estimate relates both to the source and to the entire path to the Earth) and n is the electron density in the source.

An analysis of the Fourier spectra of the pulsations (Fig. 7) yields a much more precise estimate of the magnetic field (and, as a consequence, of the electron density of the background plasma). Indeed, the ratio of the spectra of the LCP and RCP components radically changes for a frequency change of only 0.3%, at the transition from 2.86 GHz to 2.87 GHz: in the high-frequency part of the spectrum ($f \geq 2.87$ GHz), the Fourier amplitudes for the LCP and RCP signals coincide, whereas in the low-frequency part ($f \leq 2.86$ GHz) the Fourier amplitudes of the LCP signal are systematically lower than for the RCP signal.

Such a stepwise change should be due to a transition of the system through some threshold. It is natural to suppose that this threshold is the fourth gyrolevel:

$$4f_{Be} = 2.865 \pm 0.005 \text{ GHz}, \tag{24}$$

which is transparent to the ordinary wave and partially opaque to the extraordinary wave. We then find from (24)

$$B = 255.7 \pm 0.5 \text{ G}, \tag{25}$$

and, using (18), we obtain for the background plasma density

$$n = (1.9 \pm 0.1) \times 10^{10} \text{ cm}^{-3}. \tag{26}$$

The value of n is determined with poorer relative accuracy than B, since the exact angle at which the upper hybrid waves are generated is not known.

Combining (25) and (26), we determine the ratio of the plasma frequency to the gyrofrequency in the source:

$$Y = 1.7. \tag{27}$$

The considerable group delay between the LCP and RCP components in the event analyzed suggests that conditions favorable for the manifestation of the group effect were realized. Let us return to our analysis of the relationship for the group delay (3), given in Section 3.3. This can be written

$$\Delta t_g = \frac{2}{c}\int_0^\infty \frac{\omega_{pe}^2(z)\omega_{Be||}(z)}{\omega^3}dz \tag{28}$$

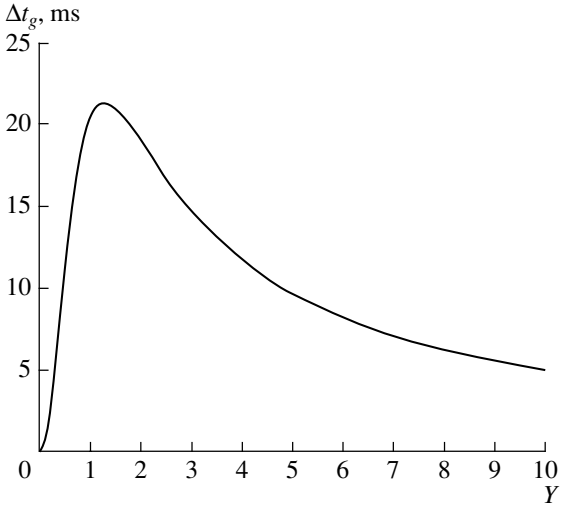

Fig. 12. Group delay for waves emitted at the double hybrid frequency in a uniform magnetoactive plasma with a linear size of 4.5×10^9 cm as a function of the ratio of the plasma frequency to the gyrofrequency $Y = f_p/f_B$.

$$= \frac{2}{c}\frac{\omega_{ps}^2\omega_{Bs||}}{\omega^3}H,$$

where ω_{ps} and ω_{Bs} are the plasma and gyrofrequency in the source and

$$H = \int_0^\infty \frac{\omega_{pe}^2(z)\omega_{Be||}(z)}{\omega_{ps}^2\omega_{Bs||}}dz \qquad (29)$$
$$= \int_0^\infty \frac{n(z)B_{||}(z)}{n_s B_{s||}}dz$$

is the effective scale of the integration.

We should note the following, fundamentally important point. In Section 3.3, we analyzed the frequency dependence of the delay Δt_g without specifying the emission mechanism in any way (we only assumed that $\omega^2 \gg \omega_{pe}^2, \omega_{pe} > \omega_{Be}$), so the frequency ω was an independent variable. Now we have identified the emission mechanism, and the frequency of the radio emission is expressed in terms of the frequencies ω_{ps} and ω_{Bs} in accordance with (17) and (18).

Substituting the frequency (18) into (28) and making a transformation to the dimensionless variable $Y_s = \omega_{ps}/\omega_{Bs}$, we obtain

$$\Delta t_g = \frac{H}{4c}\left(\frac{2f_{UHs}}{f}\right)^3 \frac{Y_s^2}{(1+Y_s^2)^{3/2}}, \qquad (30)$$

where $2f_{UHs}/f \approx 1$. We emphasize that this formula describes the group delay not in the arbitrary case, as for (28), but only for waves emitted near the double upper hybrid frequency.

Equation (30) reaches its maximum when (Fig. 12)

$$Y = \sqrt{2} \approx 1.4. \qquad (31)$$

It is easy to see that the values of Y obtained from the observations (27) and theoretically (31) are indeed close to each other, confirming our assumption. Using relationship (30) simultaneously with (27), we can estimate the scale length on which the group delay occurs:

$$H \approx 5 \times 10^9 \text{ cm}. \qquad (32)$$

Let us now proceed to an analysis of the turbulence properties of the upper hybrid waves generated by the fast electrons, turning to the spectral properties of the radio emission. It is obvious that the bandwidth of the radio emission consists of the intrinsic width arising in a homogeneous source and the contribution of the inhomogeneity of the real source. It is clear that the theoretically predicted intrinsic width of the plasma waves should not exceed the observed width of the pulsations.

If the upper hybrid waves were distributed isotropically, then, according to (15), the corresponding intrinsic width (near $Y \approx 1.7$) would be

$$\frac{\Delta\omega}{\omega} \sim 10\text{–}20\%. \qquad (33)$$

However, the observed total width is only $\sim 3\%$. Consequently, the plasma turbulence in the source is distributed anisotropically.

Numerical studies of the nonlinear plasma mechanism [5, 6] yield characteristic values of the angle θ at which the upper hybrid waves are generated, their wave number k, and the scatter of these quantities Δk and $\Delta\theta$:

$$kd_e \sim 0.1, \qquad (34)$$

$$\theta \sim 80^\circ, \qquad (35)$$

$$\Delta k d_e \sim 0.1, \qquad (36)$$

$$\Delta\theta \leq 30^\circ \qquad (37)$$

so that $\Delta k \sim k$, providing the intrinsic emission width is [see (15) and (16)]

$$\frac{\Delta\omega}{\omega} \sim 1\text{–}2\%. \qquad (38)$$

This means that the contribution of the source inhomogeneity to the total width may be comparable to the intrinsic spectral width for the emission mechanism.

The theory of the nonlinear plasma mechanism predicts a relation between the oscillation period and plasma wave parameters. In the case of strong oscillations, we have [3–6]:

$$\tau = \ln(W_{\max}/W_0)/\gamma_{\text{eff}}, \qquad (39)$$

where W_0 and $W_{\max}$ are the initial and maximum levels of the energy density of the plasma waves and

γ_{eff} is the effective decrement for the plasma-wave attenuation, which can be determined either by collisional attenuation of the waves in a plasma or by absorption of the waves by fast electrons. Since the oscillation period does not change in our case (within the errors), we can confidently conclude that collisional attenuation dominates, so

$$\gamma_{\text{eff}} \approx \nu_{ei} \approx 60\ nT^{-3/2}. \quad (40)$$

Since we have already found the period and plasma density, and $\ln(W_{\max}/W_0) \sim 10$, the electron temperature of the background plasma can be estimated to be

$$T \approx 3 \times 10^6\ \text{K}. \quad (41)$$

Since the time scales for the growth and decay of the intensity in the pulsations are of the same order, the maximum increment for the amplification of the waves is of the order of the effective wave decrement: $\gamma_{\max} \sim \gamma_{\text{eff}}$. Hence, the maximum increment is

$$\gamma_{\max} \approx (2-3) \times 10^2 c^{-1} \approx (3-4) \times 10^{-8} \omega_{pe}. \quad (42)$$

Then, the density of fast electrons in the source of emission can be estimated to be

$$n_{\text{b}} \sim 10^5\ \text{cm}^{-3}, \quad (43)$$

since it is known [4] that

$$\gamma_{\max} \sim 10^{-2}(n_{\text{b}}/n)\omega_{pe}. \quad (44)$$

The dimensionless energy density of the plasma waves is related to the pulsation period and their frequency [4] by the expression

$$w = \frac{W}{nT} \sim \frac{100}{f\tau} \approx 10^{-6}. \quad (45)$$

The brightness temperature of the emission generated by the plasma mechanism at the second harmonic is described by the formula [4]

$$T_{\text{b}} = a_\omega L_{||} = \frac{(2\pi)^3}{15\sqrt{3}} \frac{c^3 L_{||}}{f_{pe}^2 V_{ph}} \frac{w^2}{\zeta^2} nT, \quad (46)$$

where a_ω is the emission coefficient; $L_{||}$ is the source size along the line of sight; V_{ph} is the phase velocity of the transverse waves (for $f \approx 2f_{UH}$); and $\zeta = (c/\omega_{pe})^3(\Delta k)^3$ is related to the phase volume occupied by the plasma waves, which is ≈ 30 in our case [see (36)].

On the other hand, the brightness temperature can be calculated from the observed flux (the pulsation amplitude $F \approx 20$ sfu):

$$T_{\text{b}} \approx 1.4 \times 10^{26} \frac{F_{sfu}}{f_{GHz}^2 L_\perp^2}\ \text{K}, \quad (47)$$

where $L_\perp$ (cm) is the source size perpendicular to the line of sight. It is natural to assume that the longitudinal and transverse sizes of the source are of the same order:

$$L_{||} \sim L_\perp. \quad (48)$$

We then find from (46) and (47) the brightness temperature

$$T_{\text{b}} \sim 5 \times 10^{12}\ \text{K} \quad (49)$$

and the source size

$$L \sim 10^7\ \text{cm}. \quad (50)$$

The resulting source size is in excellent agreement with our earlier assumption that the main contribution to the observed group delay occurs on the way from the source to the observer, not in the source itself. If this effect were strong within the source, then, in addition to the delay, it would result in a considerable decrease of the depth of modulation of the emission (first and foremost for the extraordinary waves, i.e., the LCP waves), which is not observed.

Thus, we have obtained a harmonious and logically consistent picture of the emission assuming a homogeneous source and have found the average values of numerous relevant parameters. Let us now take into account the source inhomogeneity.

4.3. Radio Source Inhomogeneity

In our analysis of the bandwidth of the pulsations, we already pointed out that the contribution of the source inhomogeneity may be comparable to the intrinsic width for the emission mechanism; i.e., the effects of source inhomogeneity may be important, in spite of the relatively small source size.

As already stated, the radio emission frequency is twice the upper hybrid frequency, which is determined by the values of the plasma frequency and gyrofrequency. In the solar corona, these frequencies (determined by the plasma density and magnetic field strength) decrease with increasing distance from the solar surface. This means that, on average, the higher frequency emission (of each mode) is generated in deeper layers of the corona and travels a longer distance to the observer than the low-frequency emission.

If these signals had identical group velocities, this effect would result in a delay of the arrival of the high-frequency signal relative to the low-frequency signal. In fact, the group velocity depends on the frequency, asymptotically approaching the velocity of light with increasing frequency. Thus, high-frequency waves propagate faster than low-frequency waves, and, under real conditions, high-frequency waves can

either lead or lag low-frequency waves, depending on the conditions realized.

We will study these effects quantitatively as follows. Let us assume that the peak of the low-frequency emission (at frequency $\omega_o = 2\pi f_o$, in our case $f_o = 2.81$ GHz) is generated at $z = 0$ and that the emission peak at other frequencies is generated at $-z(\omega)$ (where $z(\omega)$ is a positive quantity). We can then write for each mode the autodelay as a function of frequency and the (already analyzed above) mutual delay between the modes taking into account the source inhomogeneity.

The time after which the signal of mode σ at the reference frequency ω_o reaches the Earth is

$$t_o^\sigma = \int_0^{R_{SE}} \frac{dz}{v_\sigma(\omega_o)}. \quad (51)$$

The same time for a signal at an arbitrary frequency is

$$t_\omega^\sigma = \int_{-z(\omega)}^{R_{SE}} \frac{dz}{v_\sigma(\omega)}. \quad (52)$$

Accordingly, the relative delay of these signals is determined by the difference of relationships (52) and (51). Before writing this delay, we will make the following important remark. In the previous sections, we used expansions of the wave refractive indices and group velocities in the parameter $\omega_{pe}^2/\omega^2 \ll 1$, providing accuracy of the order of 20%, sufficient for estimates of various mean quantities. In this section, we wish to study effects of the radio source inhomogeneity with a relative size on the order of the total width of the pulsations, i.e., of about 3%. This means that we cannot use these expansions for the refractive indices and group velocities. Therefore, in our subsequent analysis, we use their exact expressions (in a cool plasma) [11] and carry out expansions only in the small quantity $\Delta\omega/\omega \sim 3\%$.

Let us introduce (for compactness of the subsequent formulas) the new functions:

$$F_\sigma(\omega) = c/v_\sigma(\omega), \quad F(\omega) = F_X(\omega) - F_O(\omega). \quad (53)$$

Then, the formulas for the autodelay of mode σ at frequency ω relative to the reference frequency ω_o are

$$\Delta t_\omega^\sigma = t_\omega^\sigma - t_{\omega_o}^\sigma = \frac{1}{c}\int_{-z(\omega)}^{0} F_\sigma(\omega)dz + \frac{1}{c}\int_0^\infty (F_\sigma(\omega) - F_\sigma(\omega_o))dz. \quad (54)$$

With this definition, the delay will be negative if the high-frequency signal reaches the Earth first and positive if the low-frequency signal arrives first. In the latter integral, the upper limit can be replaced with ∞, because parts of the path distant from the source do not make an appreciable contribution to (54).

When calculating the autodelay (54), we use the narrowness of the bandwidth of the pulsations: $\Delta\omega/\omega_o \ll 1$. In the second term, this enables us to expand the function $F_\sigma(\omega)$ of the frequency in a series with an accuracy to within $\Delta\omega/\omega_o$ and to simplify the integral. To calculate the first term to the same accuracy, we note that the region of integration for this term is a small quantity of the same order as $\Delta\omega/\omega_o$: $z(\omega)/H_{\text{eff}} \sim \Delta\omega/\omega_o$, where H_{eff} is a characteristic length giving the main contribution to the integration of the second term.

The autodelay then becomes

$$\Delta t_\omega^\sigma = \frac{z(\omega)}{c}F_\sigma(\omega_o) + \frac{1}{c}\frac{\Delta\omega}{\omega_o}\int_0^\infty \left(\omega\frac{\partial F_\sigma(\omega)}{\partial\omega}\right)_{\omega=\omega_o} dz. \quad (55)$$

As we shall see below, to study the function $z(\omega)$, it is convenient to consider the sum of the delays in the X and O modes:

$$\Delta t_\omega^X + \Delta t_\omega^O = \frac{z(\omega)}{c}(F_X(\omega_o) + F_O(\omega_o)) + \frac{1}{c}\frac{\Delta\omega}{\omega_o}\int_0^\infty \omega_o\left(\frac{\partial F_X(\omega)}{\partial\omega} + \frac{\partial F_O(\omega)}{\partial\omega}\right)_{\omega=\omega_o} dz. \quad (56)$$

It is obvious that the integral in the second term can be represented as a product of the integrand evaluated at $z = 0$ and the effective integration scale H_{eff}. To a first approximation in $\Delta\omega/\omega_o$, the function $z(\omega)$ can be written

$$z(\omega) = æ\frac{\Delta\omega}{\omega_o}H_{\text{eff}}, \quad (57)$$

where æ is an unknown dimensionless parameter. Then,

$$\Delta t_\omega^X + \Delta t_\omega^O = \frac{H_{\text{eff}}}{c}\frac{\Delta\omega}{\omega_o}\left\{æ(F_X(\omega_o) + F_O(\omega_o)) + \omega_o\left(\frac{\partial F_X(\omega)}{\partial\omega} + \frac{\partial F_O(\omega)}{\partial\omega}\right)_{\omega=\omega_o}\right\}. \quad (58)$$

Let us now derive a more precise relation than (28) for the mutual delay Δt_g, taking into account, in particular, the radio source inhomogeneity. Similar to the derivation of (55), we obtain

$$\Delta t_g(\omega) = \frac{z(\omega)}{c}F(\omega_o, 0) + \frac{1}{c}\int_0^\infty F(\omega_o, z)dz \quad (59)$$

$$+\frac{1}{c}\frac{\Delta\omega}{\omega_o}\int_0^\infty\left(\omega\frac{\partial F(\omega,z)}{\partial\omega}\right)_{\omega=\omega_o}dz.$$

Taking into account that

$$\int_0^\infty F(\omega_o,z)dz = F(\omega_o,0)H, \qquad (60)$$

$$\int_0^\infty\left(\omega\frac{\partial F(\omega,z)}{\partial\omega}\right)_{\omega=\omega_o}dz=\left(\omega\frac{\partial F(\omega,0)}{\partial\omega}\right)_{\omega=\omega_o}H_1,$$

where H and H_1 are the corresponding effective integration scales, and also using (57), we find

$$\Delta t_g(\omega)=\frac{HF(\omega_o)}{c}\left\{1+\frac{H_1}{H}\frac{\omega_o}{F(\omega_o)}\right. \qquad (61)$$

$$\left.\times\left(\frac{\partial F(\omega)}{\partial\omega}\right)_{\omega=\omega_o}\frac{\Delta\omega}{\omega_o}+æ\frac{H_{\rm eff}}{H}\frac{\Delta\omega}{\omega_o}\right\}.$$

Let us analyze this formula in more detail. The frequency dependence of Δt_g is described by the second and third terms in braces. If the emission frequency were much higher than the plasma frequency, we would have $H_1 = H$ and

$$\alpha=\frac{\omega_o}{F(\omega_o)}\left(\frac{\partial F(\omega)}{\partial\omega}\right)_{\omega=\omega_o}\approx -3, \qquad (62)$$

in accordance with the approximate formula (28) derived in Section 4.2. The $\alpha(\omega)$ dependence for a fixed plasma frequency is presented in Fig. 13a. We can see that α can be quite different from -3 near the plasma frequency. In our case, the emission frequency (18) is close to the plasma frequency, and their ratio is determined solely by the value of Y. Figure 13b shows α as a function of Y; α differs appreciably from its asymptotic value (-3) at all values of Y and varies from -3.9 to -3.75 in the range of Y of interest for us.

The third term in braces in (61), related to the source inhomogeneity, is appreciably positive and is determined solely by the constant æ (for a fixed ratio of the effective integration scales $H_{\rm eff}/H$).

Let us now proceed to finding the value of æ. For this purpose, we express this quantity in terms of the sum of the autodelays (58):

$$æ=\frac{\omega_o\left(\frac{\partial F_X(\omega)}{\partial\omega}+\frac{\partial F_O(\omega)}{\partial\omega}\right)_{\omega=\omega_o}}{F_X(\omega_o)+F_O(\omega_o)} \qquad (63)$$

$$+\frac{\omega_o}{\Delta\omega}\frac{c(\Delta t_\omega^X+\Delta t_\omega^O)}{H_{\rm eff}(F_X(\omega_o)+F_O(\omega_o))}.$$

The first term in this formula is a function of Y and does not depend on other parameters of the source or on the observational errors. In the second term, the quantity $\omega_o/\Delta\omega$ is known, and the delays Δt_ω^σ are known from the observations (with some error),

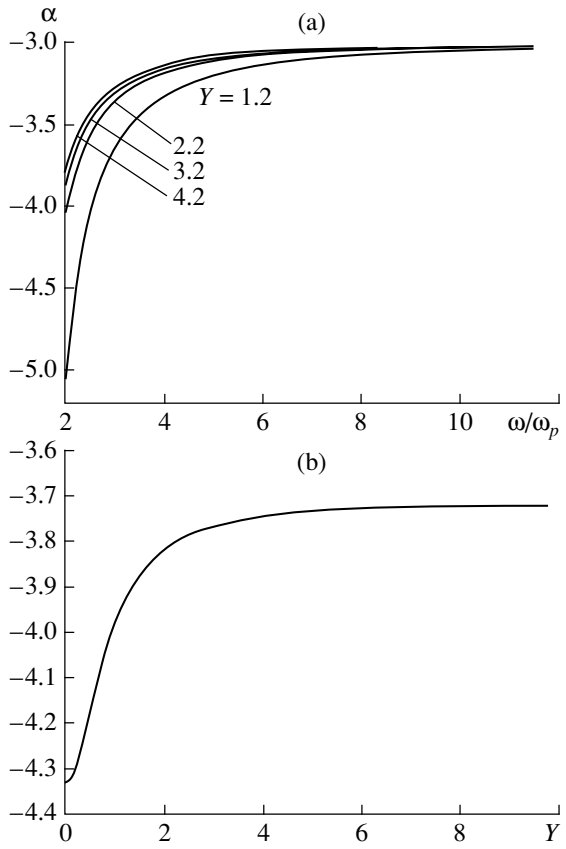

Fig. 13. Index α (a) as a function of frequency for various values of Y and (b) as a function of Y for waves at the double hybrid frequency.

whereas the scale $H_{\rm eff}$ is not known. Therefore, it is convenient to transform the second term using (61). We multiply and divide this term by $\Delta t_g/H$, noting also that we have at the reference frequency ω_o

$$c\Delta t_g/H = F(\omega_o). \qquad (64)$$

Formula (63) then reduces to

$$æ=\frac{\omega_o\left(\frac{\partial F_X(\omega)}{\partial\omega}+\frac{\partial F_O(\omega)}{\partial\omega}\right)_{\omega=\omega_o}}{F_X(\omega_o)+F_O(\omega_o)} \qquad (65)$$

$$+\frac{\omega_o}{\Delta\omega}\frac{F(\omega_o)}{F_X(\omega_o)+F_O(\omega_o)}\frac{\Delta t_\omega^X+\Delta t_\omega^O}{\Delta t_g}\frac{H}{H_{\rm eff}}.$$

The advantage of this form is that æ now depends on the ratio of the effective scales $H/H_{\rm eff}$, which is of the order of unity, rather than on the absolute value of $H_{\rm eff}$.

The dependence of æ on Y for various values of $H/H_{\rm eff}$ is presented in Fig. 14. Note the weak dependence of æ on both Y and $H/H_{\rm eff}$. This is due to the smallness of the sum of the autodelays $\Delta t_\omega^X+\Delta t_\omega^O$ in the analyzed event. To an accuracy sufficient for the

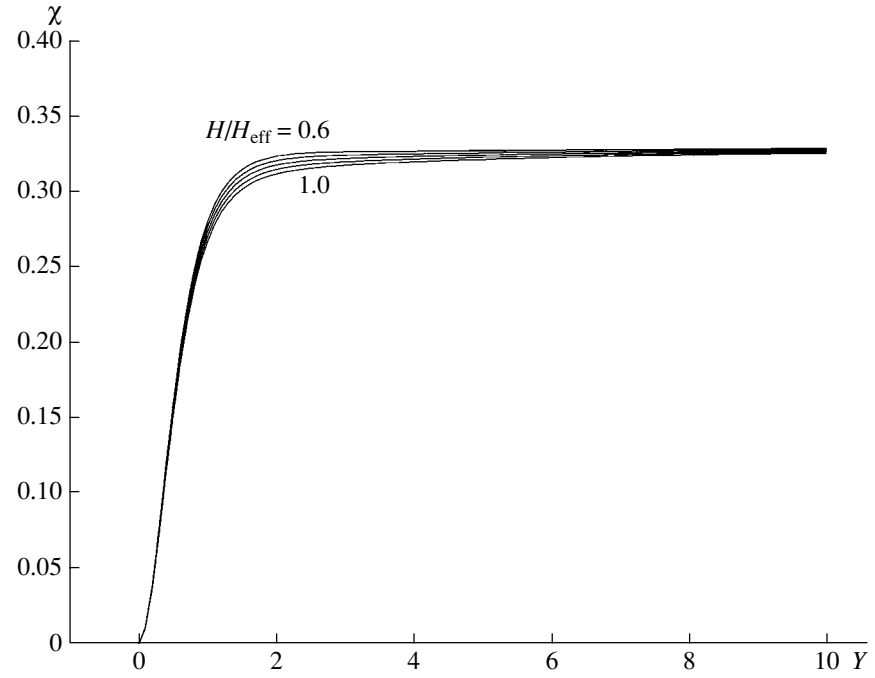

Fig. 14. Inhomogeneity index æ as a function of Y for various values of $H/H_{\text{eff}} = 0.6, 0.7, 0.8, 0.9, 1.0$.

subsequent analysis, we can assume that

$$æ = 0.32 = \text{const}(Y, H/H_{\text{eff}}). \qquad (66)$$

Let us now consider the expressions for the autodelays. Substituting the expression for $z(\omega)$ (57) into (55) and introducing the effective integration scales H_σ ($\sigma = X, O$), we obtain

$$\Delta t_\omega^\sigma = \frac{H_{\text{eff}}}{c}\frac{\Delta\omega}{\omega_o} \qquad (67)$$
$$\times \left\{ æ F_\sigma(\omega_o) + \frac{H_\sigma}{H_{\text{eff}}}\left(\omega\frac{\partial F_\sigma(\omega)}{\partial\omega}\right)_{\omega=\omega_o}\right\}.$$

Figure 11 shows the theoretical dependences Δt_ω^σ taking into account (66) for various values of H_σ/H_{eff}, together with the observational data. Note that the effect of source inhomogeneity is dominant for the ordinary waves (i.e., the low-frequency signal reaches the observer first so that the delays are positive), while the effect of dispersion dominates for the extraordinary waves (i.e., the delays are negative).

Above, in our analyses of various integrals, we introduced five different effective scales having the same order of magnitude. Note that not all of these scales are independent. It is easy to show that

$$H_{\text{eff}} = \left\{\frac{\frac{\partial F_X(\omega)}{\partial\omega}H_X + \frac{\partial F_O(\omega)}{\partial\omega}H_O}{\frac{\partial F_X(\omega)}{\partial\omega} + \frac{\partial F_O(\omega)}{\partial\omega}}\right\}_{\omega=\omega_o}, \qquad (68)$$

$$H_1 = \left\{\frac{\frac{\partial F_X(\omega)}{\partial\omega}H_X - \frac{\partial F_O(\omega)}{\partial\omega}H_O}{\frac{\partial F_X(\omega)}{\partial\omega} - \frac{\partial F_O(\omega)}{\partial\omega}}\right\}_{\omega=\omega_o}. \qquad (69)$$

Hence, in particular, it is clear that, if $H_X = H_O$, then $H_{\text{eff}} = H_1 = H_X = H_O$. Generally speaking, the frequency dependences of the delays allow us to determine the relative values of the effective scales. However, the presence of errors in the observational data prevents us from deriving the true differences in the scales. Therefore, we will assume the scales to be identical and equal to H.

Under this condition, the frequency dependence of the mutual delay is represented in Fig. 10 by a straight line, consistent with the observational data. The condition of equal scales corresponds to solid curves in Fig. 11, also in agreement (within the errors) with the observational data.

The scale H can be estimated from the graph in Fig. 12. It is clear that $H > 4 \times 10^9$ cm for any Y, and we have for $Y = 1.7$

$$H \sim 5 \times 10^9 \text{ cm}. \qquad (70)$$

4.4. The Role of Inhomogeneity

An analysis of the frequency dependence of the autodelays provides further confirmation of the solar origin of the radio pulsations and enables us to obtain new information about the radio source.

Let us consider the source linear size $l \approx z$ (2.89 GHz):

$$l = æH_{\text{eff}}\frac{\Delta f}{f_o} \approx 4 \times 10^7 \text{ cm}. \quad (71)$$

This quantity exceeds by several times the source size found from the radio flux and brightness temperature of the radio emission (50). This discrepancy has a simple logical explanation. In Section 4.2, we calculated the size of a homogeneous radio source radiating with the intrinsic bandwidth; i.e., the effective source size at each frequency was ~ 100 km. Hence, solving (71) for $\Delta f/f_o$ and substituting $l = 100$ km, we can estimate the intrinsic bandwidth of the emission mechanism as $\Delta f/f_o \sim 1\%$, or $\Delta f \approx 20$ MHz.

However, regions radiating at different (though similar) radio frequencies are spatially shifted relative to each other. In this section, we find the total size l of the nonuniform source (from the level of maximum emission at the highest frequency to that at the lowest frequency) radiating at all frequencies in a bandwidth ~ 80 MHz to be ≈ 400 km, based on an analysis of the frequency dependences of the delays.

The gradients of physical parameters in the radio source are also of interest. To analyze these gradients, we rewrite (71) as

$$\frac{\Delta f}{l} = \frac{f_o}{æH_{\text{eff}}}. \quad (72)$$

Owing to the narrow frequency bandwidth and small source size, we can assume that $\Delta f/l \approx df/dz$, and then

$$\frac{df_{UH}}{dz} = \frac{f_{UH}}{æH_{\text{eff}}} \quad (73)$$

is the gradient of the upper hybrid frequency in the source. Since d/dz is, on average, $\sim H_{\text{eff}}^{-1}$ along the line of sight in the corona, we see that the gradient in the radio source is approximately a factor of three greater than the mean gradient. Thus, the instability of the upper hybrid modes arises in a (locally) more nonuniform (than average) site of a magnetic trap. This can take place either at the feet of a loop or in a "local magnetic trap." Recall that such local traps are sources of radio spikes in plasma with $Y < 1$ [12].

5. CONCLUSION

We have studied in detail the properties of pulsed radio bursts in a solar flare. Our Fourier analysis of the radio signal has demonstrated that the observed oscillations of the degree of polarization of the radio emission are due to the relative shifts of the extraordinary and ordinary waves, which have different group velocities.

In the source, these waves are generated with similar intensities so that the source emission has a low degree of circular polarization. This imposes very strict constraints on the mechanism for the radio emission, and we conclude that it must be the plasma mechanism operating at the second harmonic of the local upper hybrid frequency.

Applying the theory of the nonlinear plasma mechanism and taking into account the inhomogeneity of the radio source, we have established a considerable number of parameters of the plasma, fast electrons, and plasma turbulence for this event:

Background plasma density	$n = 1.9 \times 10^{10}$ cm^{-3}
Magnetic field	$B = 256$ G
Kinetic electron temperature	$T \approx 3 \times 10^6$ K
Number density of fast electrons	$n_{\text{b}} \sim 10^5$ cm^{-3}
Increment of the plasma waves	$\gamma_{\max} \sim 300$ s^{-1}
Spectral bandwidth of the generated plasma waves	$\Delta\omega/\omega \leq 3\%$
Wavenumber of the generated plasma waves	$kd_e \approx 0.1$
Scatter of the wavenumbers	$c\Delta k/\omega_{pe} \approx 3$ or $\Delta k d_e \approx 0.1$
Direction of maximum amplification of the plasma waves	$\theta \approx 80°$
Angular scatter of the generated plasma waves	$\Delta\theta \approx 30°$
Level of plasma turbulence	$w = W/nT \approx 10^{-6}$
Brightness temperature of the emission	$T_{\text{b}} \approx 5 \times 10^{12}$ K
Source size at the chosen frequency	$L \approx 100$ km
Total source size	$l \approx 400$ km
Plasma parameter in the source	$Y = 1.7$
Intrinsic width of the spectral line	$\Delta f/f \approx 1\%$
Homogeneity size scale:	
average in the corona	$H \approx 5 \times 10^9$ cm
in the radio source	$æH \approx 1.5 \times 10^9$ cm

This summary of parameters shows that an accurate analysis of the spectral properties of the pulsed

radio emission can be used to extract detailed information on the source properties; such detailed information cannot be obtained from analyses of electromagnetic waves in other (outside the radio) spectral ranges.

The potential of such diagnostics is far from exhausted: new information can be obtained (at least in principle) from the frequency dependences of the pulsation period, wave modulation depth, etc. It is no less important to study the magnitude of these effects in other events demonstrating millisecond radio pulsations.

ACKNOWLEDGMENTS

The authors are grateful to A.T. Altyntsev, A.S. Grebinskiĭ, I.E. Kozhevatov, and I. Yan for interesting discussions of the problems addressed in this paper. This work was supported by the Russian Foundation for Basic Research (project nos. 00-02-16356, 99-02-16914, 01-02-16586) and the State Science and Technology Program in Astronomy.

REFERENCES

1. V. F. Melnikov and A. Magun, Sol. Phys. **178**, 591 (1998).
2. V. F. Melnikov and A. V. R. Silva, in *Magnetic Fields and Solar Processes,* ESA SP-448, Vol. 2, p. 1053.
3. V. V. Zaitsev, Sol. Phys. **20**, 95 (1971).
4. V. V. Zaitsev and A. V. Stepanov, Sol. Phys. **88**, 297 (1983).
5. V. B. Korsakov and G. D. Fleishman, Izv. Vyssh. Uchebn. Zaved., Radiofiz. **41**, 46 (1998).
6. G. D. Fleishman and V. B. Korsakov, in *Magnetic Fields and Solar Processes,* ESA SP-448, Vol. 2, p. 803.
7. Q. J. Fu, Z. H. Qin, H. R. Ji, and L. B. Pei, Sol. Phys. **160**, 97 (1995).
8. *SGD: Solar Geophysical Data* (Inst. for Environmental Research, Washington, 1997), Nos. 640–641, Part 1.
9. S. L. Marple, Jr., *Digital Spectral Analysis: with Applications* (Prentice-Hall, Englewood Cliffs, 1987).
10. A. R. Thompson, J. M. Moran, and G. W. Svenson, *Interferometry and Synthesis in Radio Astronomy* (Wiley, New York, 1990).
11. A. I. Akhiezer, I. A. Akhiezer, R. V. Polovin, A. G. Sitenko, and K. H. Stepanov, *Plasma Electrodynamics* (Nauka, Moscow, 1974; Pergamon, Oxford, 1975).
12. G. D. Fleishman and V. F. Melnikov, Usp. Fiz. Nauk **168**, 1265 (1998) [Phys. Usp. **41**, 1157 (1998)].

Translated by G. Rudnitskiĭ

Astronomy Reports, Vol. 46, No. 6, 2002, pp. 515–520. Translated from Astronomicheskiĭ Zhurnal, Vol. 79, No. 6, 2002, pp. 570–576.

Variations of the Amplitude of the Chandler Wobble

G. S. Kurbasova[1], L. V. Rykhlova[2], and M. N. Rybalova[1]

[1]*Crimean Astrophysical Observatory, p/o Nauchnyĭ, Crimea, 334413 Ukraine*

[2]*Institute of Astronomy, Pyatnitskaya 48, Moscow, 109017 Russia*

Received August 15, 2001; in final form, November 23, 2001

Abstract—The main force and parametric actions on oscillations in the Earth–Moon system are compared. Parametric excitations due to external periodic changes in the distance between the Earth's and Moon's centers of mass occur in a limited number of frequency intervals. We demonstrate the role of a nonlinear parameter that limits the oscillation amplitudes, and compute the frequency interval for excitations near the Chandler frequency. © *2002 MAIK "Nauka/Interperiodica"*.

1. INTRODUCTION

Numerous scientific and practical applications require data on the Earth's size and position in space, as well as data on its complicated progressive and rotational motion, which are affected by both its internal structure and its attraction to other celestial bodies. These data include the Earth orientation parameters (the coordinates X_p and Y_p of the pole and the time UT1), derived from astronomical observations. The general requirements for the accuracy of the Earth orientation parameters are determined by their role in the establishment of reference systems required for modern, high-precision geodynamical and astronomical observations and theoretical models of the Earth.

The difficulty in establishing such reference systems is that theoretical models of the Earth's structure and rotation cannot explain the observed variations in the coordinates of the pole. The physical nature of these changes is the subject of discussion and controversy.

Variations in the coordinates of the Earth poles are usually modeled as a superposition of a polynomial component and two periodic oscillations: the Chandler wobble and seasonal variation. The parameters of this model require constant refinement based on observations.

There also exist more complicated models. However, since no convincing physical origins for the excitation of the Chandler wobble have been identified, these models do not explain the observed variations in the Chandler amplitude: if the Chandler oscillation were a free motion, it would necessarily be damped, but astronomical observations over the past 150 yr do not indicate any such damping. Discrepancies between theory and observation necessitate either improvement of the theory or a new method for modeling the observed behavior. If improvements in the theory do not bring it closer to the observations, the need for a new modeling method becomes obvious. A new method for modeling the polar motion was first proposed by us in 1995 [1] and studied further in subsequent works. We showed that the increase in the period of the Earth's free nutation (the Chandler period) finds a simple explanation if we consider the motion of the interconnected Earth–Moon–Sun system: the fundamental frequency of the free Earth is transformed into the fundamental frequency of the Earth–Moon system due to the mutual action of the system's natural oscillations. The present work continues our previous investigations of this problem.

2. NATURAL OSCILLATIONS

The gravitational attraction between two material points or two spherically symmetric bodies with the masses of the Earth (m_E) and Moon (m_M) is governed by the law of universal gravitation. In the two-body problem, we neglect all forces except the mutual attraction of the two spherically symmetric bodies. This model enables exact integration of the equations of motion and treats additional forces as perturbations.

We can simplify studies of oscillations in the Earth–Moon system by using a model with a linear system with two degrees of freedom. In this case, the properties of the oscillations are determined by the degree of physical interaction between the two bodies.

The system of homogeneous equations for the problem at hand takes the form

$$\left.\begin{aligned} \ddot{\psi} + \nu_1^2\psi - 2\lambda(\nu_2^2 - \nu_1^2)\eta = 0 \\ \ddot{\eta} + \nu_2^2\eta - 2\lambda(\nu_2^2 - \nu_1^1)\psi = 0 \end{aligned}\right\}, \qquad (1)$$

1063-7729/02/4606-0515$22.00

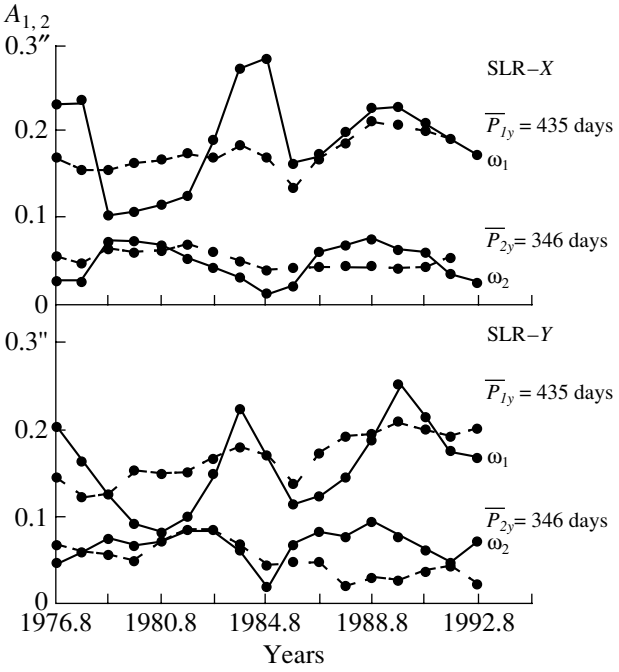

Fig. 1. Estimates of amplitudes for the natural frequencies $\bar{\omega}_1(\bar{P} = 435$ days) and $\bar{\omega}_2(\bar{P} = 346$ days).

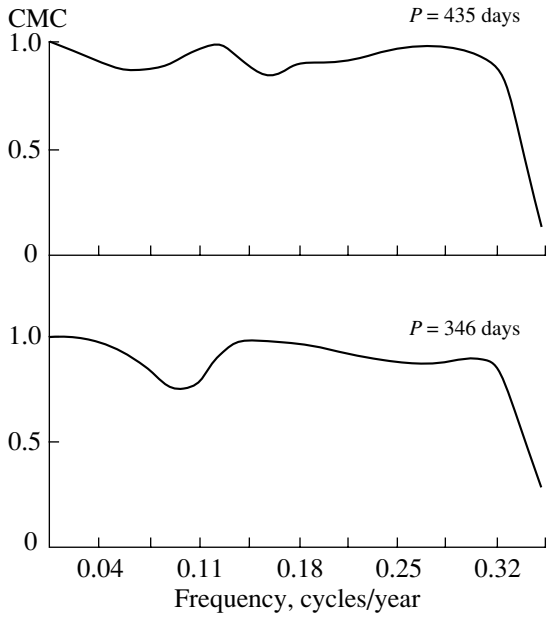

Fig. 2. Coefficients of the modulus of the coherence (CMC) for the amplitudes of the frequencies $\bar{\omega}_1(\bar{P} = 435$ days) and $\bar{\omega}_2(\bar{P} = 346$ days).

where ν_1 and ν_2 are the (partial) natural frequencies of the Earth and Moon, respectively, λ is the interaction coefficient, and ψ and η are small deviations from the equilibrium motion. Eqs. (1) and the interaction coefficient λ were derived previously in [2].

Solving these equations yields the frequencies ω_1 and ω_2 for the natural oscillations of the Earth–Moon system for various combinations of the partial frequencies ν_1 and ν_2

$$\left.\begin{aligned} &\nu_2 > \nu_1 \\ &\omega_1^2 = k_1\nu_1^2 - k_2\nu_2^2 \\ &\omega_2^2 = k_1\nu_2^2 - k_1\nu_1^2 \end{aligned}\right\}, \tag{2}$$

$$\nu_2 = \nu_1 = \omega_1 = \omega_2, \tag{3}$$

$$\left.\begin{aligned} &\nu_2 < \nu_1 \\ &\omega_1^2 = k_1\nu_2^2 - k_2\nu_1^2 \\ &\omega_2^2 = k_1\nu_1^2 - k_2\nu_2^2 \end{aligned}\right\}. \tag{4}$$

The coefficients k_1 and $k_2(k_1 > k_2)$ are roots of the equation

$$k^2 - k - 1.05043 = 0 \tag{5}$$

and depend on the interaction coefficient $2\lambda = (1+\mu)/(1-\mu)$, where $\mu = m_{\rm M}/m_{\rm E}$ is the ratio of the masses of the Moon and the Earth, $\lambda = 0.512453$. For $\lambda = 0.5$, Eq. (5) takes the form

$$k^2 - k - 1 = 0; \tag{6}$$

that is, the roots of the equation become Fibonacci numbers ($k_1 = \Phi, k_2 = \Phi^{-1}$), which describe many parameters of and proportions in the solar system. For example, the orbital and beat periods of the planets form a geometric progression with the denominator Φ.

Let us assume that $\nu_1 = 0.90588$ cycle/year; i.e., $T\nu_1 = 403.2$ days (this corresponds to the Chandler period in the model of Wahr) and $\nu_2 = 1$ cycle/year ($T\nu_2 = 365.25$ days). Substituting these into (2), we obtain two natural frequencies for the Earth–Moon system: $\omega_1 = 0.84004$ ($T\omega_1 = 434.8$ days) and $\omega_2 = 1.05594$ ($T\omega_2 = 345.9$ days). The general solution of (1) takes the form

$$\left.\begin{aligned} &\psi = A_1\cos(\omega_1 t + \beta_1) + A_2\cos(\omega_2 t + \beta_2) \\ &\eta = \kappa_1 A_1\cos(\omega_1 t + \beta_1) + \kappa_2 A_2\cos(\omega_2 t + \beta_2) \end{aligned}\right\}, \tag{7}$$

where A_1, A_2, β_1, and β_2 are the amplitudes and phases of the oscillations, and κ_1 and κ_2 are the amplitude ratios for the frequencies ω_1 and ω_2. For the case under study, $\kappa_1 = 0.6252$ and $\kappa_2 = -1.6013$.

We can estimate the interaction between the Earth and Moon by estimating the corresponding energy

transfer. For this purpose, we assume the initial conditions (at $t = 0$) $\psi = \psi_0, \dot{\psi} = 0, \eta = 0$ and $\dot{\eta} = 0$. Substituting these into (7), we obtain

$$A_1 + A_2 = \psi_0, \quad A_1\kappa_1 + A_2\kappa_2 = 0, \qquad \beta_1 = \beta_2 = 0. \tag{8}$$

The oscillations will be described by the expressions

$$\left.\begin{aligned} \psi &= \tfrac{\psi_0}{|\kappa_2|+\kappa_1}[|\kappa_2|\cos(\omega_1 t) + \kappa_1\cos(\omega_2 t)] \\ \eta &= \tfrac{\psi_0\kappa 1|\kappa_2|}{|\kappa_2|+\kappa_1}[\cos(\omega_1 t) - \cos(\omega_2 t)] \end{aligned}\right\}. \tag{9}$$

We obtain for the natural oscillations of the Earth in the Earth–Moon system

$$\psi(t) = A(t)\cos[\omega_1 t - \beta(t)], \tag{10}$$

where

$$A_2(t) = \frac{\psi_0^2}{(|\kappa_2| + \kappa_1|)^2}\left\{\kappa_2^2 + k_1^2 + 2\kappa_1|\kappa_2|\cos[(\omega_2 - \omega_1)t]\right\}, \tag{11}$$

$$\tan(\beta(t)) = -\frac{|\kappa_2|\sin[(\omega_2 - \omega_1)t]}{\kappa_1 + |\kappa_2|\cos[(\omega_2 - \omega_1)t]}. \tag{12}$$

Since the frequencies ω_1 and ω_2 are close, we can treat $A(t)$ as an amplitude that changes with time. The period of these changes is $T_A = 2\pi/(\omega_2 - \omega_1)$; that is, $T_A = 4.63$ yrs. The maximum amplitude is ψ_0, and the minimum is $\psi_0(\kappa_1 - |\kappa_2|)/(|\kappa_2| + \kappa_1)$. This means that, if $A^{\max} = 0''.2$, $A^{\min} = -0''.08$.

Equations (1) describe oscillations in a conservative system. In a real system, there is energy dissipation. The solutions for a dissipative system take the form

$$\left.\begin{aligned} &\psi = A_1 e^{-\theta_1 t}\cos(\omega_1 t + \beta_1) \\ &+A_2 e^{-\theta_2 t}\cos(\omega_2 t + \beta_2) \\ &\eta = \kappa_1 A_1 e^{-\theta_1 t}\cos(\omega_1 t + \beta_1 + \chi_1) \\ &+\chi_2 A_2 e^{-\theta_2 t}\cos(\omega_2 t + \beta_2 + \chi_2) \end{aligned}\right\}, \tag{13}$$

where θ_1 and θ_2 are the damping coefficients for the frequencies ω_1 and ω_2, and χ_1 and χ_2 are the phase shifts for the same oscillation frequency for both bodies. These phase shifts depend on the system parameters and are proportional to the damping coefficients.

We can show that the natural frequencies ω_1 and ω_2 and coefficients κ_1 and κ_2 coincide with those for the conservative system (with an accuracy of δ_i^2/ω_i^2, where δ_i are the partial damping coefficients). Figure 1 presents the variations in the amplitudes A_1 and A_2 (solid curves) indicated by observations. These estimates were obtained using a quasi-polynomial approximation for the coordinates of the Earth's pole $\{X\}$ and $\{Y\}$ derived from CSR (SLR) laser measurements. The model for oscillations with the mean frequencies ω_1 and ω_2 is

$$A(t) = A_{0_n}\exp(\gamma_n t)\sin(2\pi\omega_n + \beta_n), \quad \text{where} \quad n = 1, 2. \tag{14}$$

Here, we take A_{0_1} and A_{0_2} on time intervals of 5–6 yrs, with a shift of 1 yr.

The coherence functions calculated using 6–9th order, two-channel, autoregression procedures exhibit peaks corresponding to periods of the data sequences A_{01}(8.8, 6.1, 3.6 yrs) and A_{02}(8.8, 4.6, 3.6 yrs). These estimates indicate a complex deformation of the amplitudes A_{01} and A_{02}. When the amplitude increases at the frequency ω_1, it decreases at ω_2. The coefficients of the modulus of the coherence (CMC) presented in Fig. 2 indicate that the oscillations A_{01}^x and A_{02}^x agree well with A_{01}^y and A_{02}^y.

3. FORCED OSCILLATIONS

Let us examine the effects of external forces on the amplitudes of the oscillations at the natural frequencies ω_1 and ω_2. Since the principle of superposition is applicable to linear systems, we should study the effect of a harmonic external force $P(t) = P_0\cos(pt)$, where p is the frequency of the external force. The solution of the homogeneous equation (1) describes the natural oscillations. Under the action of external forces, the motion becomes a superposition of free and forced oscillations. The Sun exerts the most important action on the Earth–Moon motion, and the frequency of the external force ($p = 1$ cycle/year) is close to the natural frequencies. In this case, the superposition of the free and forced oscillations (without damping) yields an oscillation with the frequency $(\eta + 1)/2$ and an amplitude that slowly changes in accordance with the harmonic law [3]

$$A(t) = -\frac{2x_0}{1 - \eta^2}\sin\frac{\eta - 1}{2}\tau. \tag{15}$$

where x_0 describes the strength of the perturbation, $\tau = \omega_0 t$ is the dimensionless time, ω_0 is the natural frequency, and $\eta = p/\omega_0$ is the ratio of the frequency of the forced oscillations to the natural frequency. If we assume that $\omega_0 = \omega_1$ and $p = 1$ cycle/year, we obtain an oscillation with the period $T_{\omega_1} = 397.2$ days whose amplitude varies with the period $P_{\omega_1} = 12.44$ yrs. For the "free" Earth, $\omega_0 = 0.903637(\omega_0 = 1/403.2$ cycle/day), and these periods are $T_{\omega_0} = 383.3$ days and $P_{\omega_0} = 21.2$ yrs, respectively. The oscillations exhibit beating, with the intervals between minima being $\tau_{\omega_1} = 6.2$ yrs and $\tau_{\omega_0} = 21.2$ yrs.

The oscillations with periods 6.1 and 3.6 yrs in the $\{A_{01}\}$ and $\{A_{02}\}$ data (Fig. 1) indicate a deformation of the amplitude of free oscillations at the frequencies ω_1 and ω_2 due to the effect of the forced oscillations.

Certain characteristic behavior can arise when the frequency of the external force is close to the partial frequencies. The first occurs if one of the partial frequencies is equal to the external frequency; i.e., $\nu_2 = p$. In this case, the forced oscillations at the frequency ν_2 (the Moon) do not occur in the system with the partial frequency ν_1 (the Earth): there is a damping of the oscillations. This will not be observed in a real system, since the resonance amplitudes become finite when damping of the forced oscillations is taken into account. Therefore, there is no complete damping in a system with losses. However, the decrease in the amplitude of ω_2 in the presence of a small amount of damping is rather significant.

Figure 1 shows $A_{0n}exp(\gamma_n t)$ for $n = 1, 2$ (dashed curves). The exponential factor smoothens the variations in the amplitudes A_{0n}. The spectrum of the data contains the periods 8.8, 6.2 and 3.6 yrs for the frequency ω_1 and 8.5 and 3.6 yrs for ω_2.

The second type of characteristic behavior for the forced oscillations in a system with two degrees of freedom is that the resonance can be absent even when $p = \omega_1$ or ω_2 in the case of certain relationships between the external forces applied to the Earth (P_{0_E}) and the Moon (P_{0_M}). For instance, if $\omega_1 = p$, the amplitudes A_1 and A_2 at the frequency ω_1 obey the relation $A_1 P_{0_E} + A_2 P_{0_M} = 0$. This is known as the orthogonality of the external force to the natural oscillation with the frequency ω_1. This orthogonality means that the work of the external forces in the first partial system (the Earth) is equal in magnitude and opposite in sign to that in the second system (the Moon). Since the total work of the external forces is zero, there is no increase in the amplitudes. The orthogonality between the external forces and natural oscillations excludes the possibility of resonance at either ω_1 or ω_2.

4. PARAMETRIC OSCILLATIONS

The homogeneous equations (1) were derived for a constant distance ρ_0 between the Earth's and Moon's centers of mass (a circular lunar orbit). The interaction coefficient in these equations is $2\lambda = (1 + \mu)/(1 - \mu)$, where $\mu = m_M/m_E$ and is a constant parameter of the system.

In the real system, the distance ρ between the centers of mass changes periodically. Of the two parameters characterizing the energy input (mass and distance), ρ is the varying quantity. The periodic changes in this parameter under the action of an external force give rise to a parametric excitation of oscillations in the system. The parametric resonance takes place for certain relationships between the frequency of the variations in ρ and the frequency at which the oscillations are excited ω, which is close or equal to the natural frequency $\omega_1 (\rho = 2\omega/n)$, and also for certain conditions on the modulation parameter m for the given frequency relation. We can determine the modulation parameter m using the limiting values of the distance ρ

$$\rho_a = a(1 + e), \quad \rho_n = a(1 - e), \tag{16}$$

where a and e are the semiaxis and eccentricity of the Moon's orbit. Then,

$$m = \frac{\rho_a - \rho_n}{\rho_a + \rho_n} = e. \tag{17}$$

The periodic change in $\rho(t)$ with the modulation depth $m = e$ takes the form

$$\rho_t = \rho_0/[1 + e\cos(2\omega t)], \tag{18}$$

where $\rho_0 = a(1 - e^2)$.

The mathematical description of parametric resonances in linear systems involves a linear differential equation with variable coefficients. A complete analysis is rather complicated for linear cases, and even more so for nonlinear cases. Let us derive the most important properties of the phenomenon using some assumptions that enable us to estimate the behavior of the parametric resonance taking into account the nonlinearity of the system.

The nonlinearity, which gives rise to nonisochronism, will lead to variations in the natural frequencies with an increase in the amplitudes, disturbing the resonance condition and limiting the amplitudes of the parametric oscillations. Taking into account the energy input parameter (18), we can describe the oscillations at the natural frequency ω_1 with $\rho = 2\omega$ using the equation

$$\ddot{x} + \omega_1^2[1 + e\cos(2\omega t)]f(x) = 0, \tag{19}$$

where ω is the frequency of the oscillations excited and $f(x)$ describes the nonlinear characteristic of the system.

We will look for a solution of (19) in the form $x = a\cos(\omega t) + b\sin(\omega t)$; that is, in the form of a steady-state oscillation ($a = \text{const}$ and $b = \text{const}$) at a frequency that is half the frequency of the parametric excitation, which corresponds to the first region of the parametric resonance.

Expanding $f(x)$ into a Fourier series, we obtain two equations for the coefficients of $\cos(\omega t)$ and $\sin(\omega t)$. We then substitute this solution into (19). Expanding $f(x)$ into a Fourier series and retaining

only $\cos(\omega t)$ and $\sin(\omega t)$ terms, we obtain the two equations

$$\omega_1^2\alpha_1(1+e/2) - a\omega^2 = 0, \qquad (20)$$
$$\omega_1^2\beta_1(1-e/2) - b\omega^2 = 0.$$

Introducing the dimensionless time $\tau = \omega t$, we obtain

$$\alpha_1 = \frac{1}{\pi}\int_{-\pi}^{\pi} f(a\cos\tau + b\sin\tau)\cos\tau d\tau, \qquad (21)$$

$$\beta_1 = \frac{1}{\pi}\int_{-\pi}^{\pi} f(a\cos\tau + b\sin\tau)\sin\tau d\tau.$$

Hence, we can find the amplitude of the steady-state solution $A = \sqrt{a^2+b^2}$ and its phase $\phi = \arctan(a/b)$.

Let us consider the case when $f(x)$ takes the form

$$f = x + \gamma x^3, \qquad (22)$$

where $\gamma = \sqrt{1+(4\lambda)^2}$ is a dimensionless coefficient describing the system nonlinearity. In this case,

$$\alpha_1 = a + \frac{3}{4}\gamma a^3 + \frac{3}{4}\gamma ab^2, \qquad (23)$$
$$\beta_1 = b + \frac{3}{4}\gamma b^3 + \frac{3}{4}\gamma a^2 b,$$

and we arrive at the equations

$$\omega_1^2(a + \frac{3}{4}\gamma a^3 + \frac{3}{4}\lambda ab^2)(1+\frac{1}{2}e) - a\omega^2 = 0, \qquad (24)$$
$$\omega_1^2(b + \frac{3}{4}\gamma b^3 + \frac{3}{4}\gamma a^2 b)(1-\frac{1}{2}e) - b\omega^2 = 0$$

or

$$\omega_1^2 a(1+\frac{3}{4}\gamma A^2)(1+\frac{1}{2}e) - a\omega^2 = 0, \qquad (25)$$
$$\omega_1^2 b(1+\frac{3}{4}\gamma A^2)(1-\frac{1}{2}e) - b\omega^2 = 0,$$

where $A^2 = a^2 + b^2$.

These equations admit the following solutions.

(1) The case $a = b = A = 0$ corresponds to the absence of steady-state periodic motion. It may be an equilibrium state of the system. Analysis of the stability of the system to small deviations from equilibrium leads to a linear equation with periodic coefficients (similar to the Mathieu equation). For a given modulation depth m, there are certain regions of ω close to $\omega_1/\omega = 1, 2, 3, ...n$, where the equilibrium becomes unstable, giving rise to growing oscillations at the frequencies ω, 2ω, 3ω etc. In an approximate treatment, we can restrict our study to the first region of instability near $\omega_1 = \omega$. The existence of this solution is associated with the possible realization of an equilibrium state for the specified system parameters and external actions on the system.

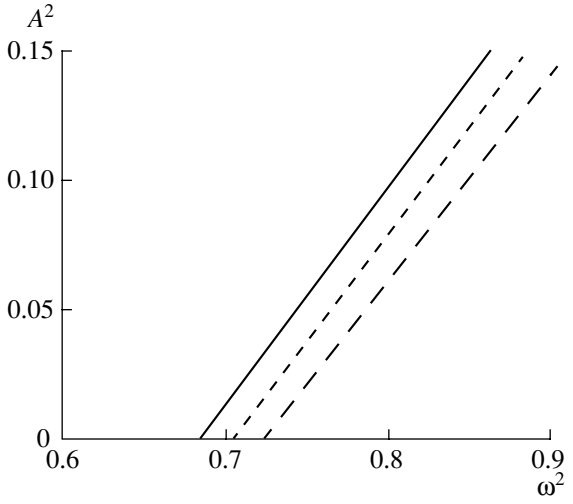

Fig. 3. Parametric resonance $A^2(\omega^2)$ of the conservative nonlinear system.

(2) Assuming $a \neq 0$ and $b = 0$, we obtain $\omega_1^2(1 + \frac{3\gamma}{4}A^2)(1+e/2) = \omega^2$, whence

$$A^2 = \frac{3}{4\gamma}\left[\frac{\omega^2}{\omega_1^2(1+e/2)} - 1\right]. \qquad (26)$$

The value of A is larger the smaller the value of γ (a coefficient describing the system nonlinearity). For $\gamma > 0$, the amplitude A is real if

$$\frac{\omega^2}{\omega_1^2(1+e/2)} - 1 > 0, \quad \text{i.e.} \qquad (27)$$
$$\omega > \omega_{11} = \omega_1\sqrt{1+e/2}.$$

(3) When $a = 0$ and $b \neq 0$, we find from the second equation of (25)

$$A^2 = \frac{4}{3\gamma}\left[\frac{\omega^2}{\omega_1^2(1-e/2)} - 1\right], \qquad (28)$$

which yields the condition for real solutions

$$\omega > \omega_{12} = \omega_1\sqrt{1-e/2}. \qquad (29)$$

Consequently, when ω is in the frequency interval ω_{11}–ω_{12}, there is an oscillation with a finite amplitude A that depends appreciably on γ.

Relations (27) and (29) indicate that the limits of the frequency interval ω_{11}–ω_{12} depend on the average natural frequency ω_1 ($T_{\omega_1} = 435.3$ days) and the modulation parameter e.

The table presents the limiting frequencies $(\omega_{11}, \omega_{12})$ and corresponding periods P_{11}, P_{12} calculated via (27) and (29) for the extremal and average modulation depths e.

Limits of intervals of the first region of parametric resonance for the average natural frequency of the Earth–Moon system $\bar{\omega}_1(\bar{P} = 435$ days)

e	ω_{11}, cycles/year	P_{11}, days	ω_{12}, cycles/year	P_{12}, days
0.0448	0.848422	430.50	0.829626	440.26
0.0549	0.850515	429.44	0.82748	441.40
0.0650	0.852602	428.39	0.82533	442.55

The parametric resonance $A^2(\omega^2)$ for the conservative nonlinear system is shown in Fig. 3; we used (26) and (28) with an average value for e for the calculations. When $\gamma < 0$, the amplitude A decreases as the frequency ω increases.

We can describe the physical process resulting from a parametric action with a given modulation depth e as follows. If we take the frequency of the external action to be $p = 2\omega$ and assume that the natural frequency ω_1 of the system is variable (for small amplitudes), we find that there is an oscillation with finite amplitude A that depends on the system nonlinearity (γ) for all frequencies ω in the frequency interval ω_{11}–ω_{12}. The nonisochronism of the system is responsible for the variation of the natural frequency with increasing amplitudes of the parametric oscillations, and the system goes to the boundary of the corresponding region of parametric excitation. This diminishes the energy input of the external force, changing ρ_t, and thus limits the growth of the amplitudes.

5. CONCLUSIONS

(1) We have used a linear model with two degrees of freedom to analyze oscillations in the Earth–Moon system. For various combinations of the partial frequencies ν_1 and ν_2 of the Earth's and Moon's oscillations, we have obtained possible natural oscillations of the Earth–Moon system with periods $T_{\omega_1} = 434.8$ and $T_{\omega_2} = 345.9$ days. We have estimated the maximum and minimum amplitudes and the periods for their variations.

(2) We have studied the influence of external forces on the amplitudes of natural oscillations in the Earth–Moon system. The most important effect is that of the Sun, for which the frequency of the external force ($P = 1$ cycle/year) is close to the natural frequencies of the system. We have studied variations in the amplitudes for a superposition of free and forced oscillations in a linear system without damping. We have also indicated the characteristic behavior that occurs when the frequency of the external force is close to the partial frequencies.

(3) Of the two parameters characterizing the Earth–Moon system (the mass and distance ρ), the distance is the variable quantity exciting parametric oscillations. We have studied the occurrence of the parametric resonance for certain relations between the frequency for variations in ρ and the frequency of the excited oscillations. We have identified the characteristic behavior of the Earth–Moon system applying assumptions that enable an accurate estimation of the behavior of the parametric resonance taking into account the system's nonlinearity.

(4) The forced oscillations can occur for any relationship between the frequency of the external action on ρ and the natural frequency ω_1, and can be excited for any amplitude of the applied force. In the case of a parametric external force, there are discrete regions of excitation. The nonlinear case differs from the linear case only in the deformation of the limits of these regions for finite oscillation amplitudes.

(5) Superposition is not applicable to nonlinear systems (in contrast to the linear case), and we cannot extract the components of individual external forces. This circumstance extremely complicates the analysis, even in a conservative approximation, and models for the effects of forces without taking into account variations in the system parameters become not completely correct. Therefore, we can only classify the external effects according to the various ways in which they add energy to the system, which is the determining factor in resonance phenomena. In a direct action, the energy of the forced oscillations develops due to the work of the external forces during the motion of the system. In a parametric action, the oscillation energy increases due to a transformation of energy from one type to another.

ACKNOWLEDGMENT

This work was supported by the Russian Foundation for Basic Research, project no. 01-02-16231.

REFERENCES

1. G. C. Kurbasova and L. V. Rykhlova, Astron. Zh. **72**, 945 (1995) [Astron. Rep. **39**, 845 (1995)].
2. G. C. Kurbasova and L. V. Rykhlova, Astron. Zh. **78**, 1049 (2001) [Astron. Rep. **45**, 922 (2001)].
3. K. Magnus, *Schwingungen: Eine Einführung in die theoretische Behandlung von Schwingungsproblemen* (Teubner, Stuttgart, 1976; Mir, Moscow, 1982).

Translated by V. Badin